Norwegian University of Life Sciences

Master's Thesis 2021   30 ECTS
Faculty of Science and Technology

Marine gravity modelling in the Norwegian coastal zone

Bjørnar Aaberge Dale

Geomatics

Abstract

This thesis investigates the possibility of using observations from satellite altimetry in marine gravity modelling. Observations of sea surface height obtained by satellite altimetry can be decomposed into different components, where the Earth's gravity field contribution is among one of those components. By reduction of all other components, a residual geoid height signal can be formed. This residual signal can be used for predicting gravity anomalies by least-squares collocation. The computations are following the *remove-compute-restore* (RCR)-method where the gravity field's long wavelength components is removed and restored using a global geopotential model. In total, three global models are used within this thesis: EGM2008, XGM2019e2159 and GOCO06s. The two first models are high-resolution GGMs, while the latter is a satellite-only model with a lower resolution. These different models are selected in order to investigate the assumption about model independence in the RCR-method.

The implementation of lest-squares collocation is validated in an area located approximately 150 km from the Norwegian coast. This area is considered to be so far from shore that any coastal effects can be neglected. The validation of least-squares collocation is carried out by comparison with gravity anomalies from a global gravity field model DTU13GRA. The global model is based, to a large extent, on the same data, while the computation method differs, and accordingly the validation procedure is termed as a near *closed-loop* simulation. Within the validation area, two different mean sea surface models, DTU13MSS and DTU18MSS, are used in the computation of residual geoid height in order to see if any systematic effects can be seen between the different components.

The prerequisite for applying least-squares collocation is that the residual signal can be treated as a stochastic signal. Empirical covariance functions are used to evaluate the stochastic properties of the residual signal. All residual signals derived by using different GGMs and MSS models result in covariance functions with shapes closely resembling the shape of a stochastic signal. The empirical errors are in mutual agreement between all three models, and hence confirming the assumption about model independence. When using DTU13MSS the empirical and formal errors are reported as $1.68 - 1.92$ mGal and $3.39 - 3.86$ mGal, while using DTU18MSS results in $2.23 - 2.35$ mGal and $3.44 - 3.78$ mGal. GOCO06s is the global geopotential model resulting best result for both DTU13MSS and DTU18MSS.

Further numerical investigations were performed at a gravimetric testbed formed by the Norwegian Mapping Authority located in the coastal areas outside of Sunnmøre. The empirical errors must be analysed with caution due to degrading quality of DTU13GRA in the coastal areas. Within this testbed the residual geoid height was formed by heterogeneous observations from Saral/ALTIKA, Saral/ALTIKA-GM, Sentinel-3A and Cryosat-2. These satellite missons employ the SAR technique resulting in significantly higher spatial resolution compared to conventional altimetry satellites. Empirical and formal errors by comparison with DTU13GRA is achieved by 4.08 mGal and 5.55 mGal, respectively.

The empirical and formal errors for both study areas are in accordance with results from similar studies. The formal errors represents an upper-bound estimate compared with the empirical errors. Due to time limitations, comparison by an independent set og ship-measured gravity anomalies provided by the Norwegian Mapping Authority is left to be performed. A comparison with ship-measured gravity anomalies is necessary in order to give a final conclusion on error-estimates of satellite altimetry derived gravity anomalies in coastal areas predicted by least-squares collocation.

Samandrag

Denne oppgåva undersøkjer høve til å nytta observasjonar frå satellittaltimetri innan marin tyngdemodellering. Observasjonar av havoverflatehøgde oppnådd frå satellittaltimetri kan bli delt opp i ulike komponentar, kor ein av desse er bidraget frå jordas tyngdefelt. Ved reduksjon av alle andre komponentar kan ein isolere eit residualgeoidesignal. Dette signalet kan nyttast til prediksjon av tyngdeanomali ved bruk av minste-kvadraters kollokasjon. Berekninga følgjer remove-compute-restore (RCR)-metoden der jordas langbølgja signal blir fjerna og attendeført ved bruk av ein global geopotensialmodell. Totalt blir tre ulike globale modellar nytta i oppgåva: EGM2008, XGM2019e2159 og GOCO06s. Dei to første modellane er høgoppløyselege modellar, medan den siste nyttar berre observasjonar frå satellittar og har ein lågare oppløysing. Desse ulike modellane blir valt for å undersøkja TEORIEN om modelluavhengigheit i RCR-metoden.

Implementeringa av minste-kvadrater kollokasjon blir validert i eit område kring 150 km frå norskekysten. Dette området blir anteke å vera tilstrekkeleg langt vekke frå kysten, slik at kysteffektar kan bli neglisjert. Valideringa av minste-kvadraters kollokasjon blir utført ved samanlikning med tyngdeanomali frå ein global tyngdemodell DTU13GRA. Denne modellen er i stor grad basert på same type data, men med ulik berekningsmetode, so valideringsprosessen blir omtalt som ein nær lukka krets simulering. I valideringsområdet blir to modellar av middelvassflater, DTU13MSS og DTU18MSS, nytta i berekninga av residualgeoidehøgde for å undersøkja om potensielle systematiske effektar kjem til syne mellom dei ulike komponentane.

Føresetnaden for bruken av minste-kvadraters kollokasjon er at residualsignalet kan bli behandla som eit stokastisk signal. Empiriske kovariansfunksjonar blir nytta til å undersøkja residualsignalets stokastiske eigenskapar. Alle residualsignala ved bruk av dei ulike global geopotensial modellane og middelvassflatene resulterer i kovariansfunksjonar som liknar nær på forma til stokastiske signal. Alle dei empiriske feila ved bruk av EGM2008, XGM2019e2159 og GOCO06s samsvarar med kvarandre, og dermed stadfestar antake om modelluavhengigheit i RCR-metoden. Ved bruk av DTU13MSS blir det oppnådd empiriske og formelle feil ved bruk av dei ulike geopotensialmodellane i intervalla $1.68 - 1.92$ mGal og $3.39 - 3.86$ mGal, medan bruk av DTU13MSS resulterer i $2.23 - 2.35$ mGal og $3.44 - 3.78$ mGal. GOCO06s er den globale geopotensialmodellen som oppnår best resultat både ved bruk av DTU13MSS og DTU18MSS.

Vidare numeriske forsøk blir utført i eit gravimetrisk testfelt danna av Kartverket i kystsona utanfor Sunnmøre. Dei empiriske feila i testfeltet må bli vurdert med aktsemd på grunn av den redusert kvaliteten til DTU13GRA i kystområde. I dette området blei berekninga berre utført med GOCO06s. I testfeltet blir residualgeoidehøgde danna ved bruk av heterogene observasjonar av havoverflatehøgde utført med Saral/ALTIKA, Saral/ALTIKA-GM, Sentinel-3A og CryoSat-2. Desse satellittferdane nyttar SAR-teknikken som gir ein betydeleg høgare romleg oppløysing samanlikna med konvensjonelle altimetrisatellittar. Empiriske og formelle feil ved samanlikning med DTU13GRA blir oppnådd på henhaldsvis 4.08 mGal og 5.55 mGal.

Dei empiriske og formelle feila oppnådd for begge studieområda er i samsvar med resultat frå liknande type studiar. Dei formelle feila dannar eit øvre feilestimat samanlikna med den empiriske feilen. På grunn av begrensa tid står det att å gjera ein uavhengig samanlikning med skipsmålt tyngdeanomali. Ein uavhengig samanlikning med skipsmålt tyngdeanomali er naudsynt for å gi ein endeleg konklusjon på feilestimatet for avleia tyngdeanomali i kystsona frå havoverflatehøgde målt med satellittaltimetri.

Føreord

Denne oppgåva markerer slutten på mine 5 år med studiar ved Noregs miljø- og biovitenskapelege universitet (NMBU). Oppgåva utgjer 30 studiepoeng og er utført i løpet av våren 2021.

Eg vil med dette retta ein stor takk til dei to vegleiarane mine Christian Gerlach og Vegard Ophaug for kyndig vegleiing i arbeidet med denne oppgåva. I gjennom hovudkurset og spesialpensum på førehand var ein godt budd til å byrja med oppgåva. Sjølv om den fysiske avstanden har vore stor mellom Kaupanger, Ås og München, så har det alltid vore hjelp å få via digitale møte eller grundige svar på eit tallaust antall e-postar.

Christian bidrog også sterkt med at tilhøva blei best mogleg fagleg for eit vellukka år på utveksling til Techische Universität München. Hjelpelinja frå utlandet til seksjonssjef Ivar og Arne Auen Grimenes i samband med utvekslinga og faglege råd blei satt høgt pris på.

Vidare skal resten av gjengen på geomatikk ha skryt for at dei fekk meg interessert i fagfeltet, og då spesielt gjennom geodesiemna til Jon-Glenn og Ola.

Andre som fortener ein takk er familie, vener og andre som alltid støttar opp når ein skal ut å utforska den store verda. Familien spesielt for det siste året med losji heime og fjernundervising.

Eg helsar også til mastergjengen på Ås for morosame stundar og godt humør i løpet av dei 5 åra.

Til min første mattelærar og gode ven, bestemor.

Bjørnar Dale

Contents

List of Figures

List of Tables

Chapter 1

Introduction

Monitoring of the Earth is of great importance, and today spending on space operations are at an all-time high. The operations have varying focus, some performs research on other celestial objects, such as the Moon and Mars, others focuses on space science, but the majority of missions monitors our planet Earth. Climate change is one of the most important questions within politics and decision making, both at regional and global level (ESA, 2020c). Satellites can provide daily updates with global coverage, and as a result *Copernicus* was formed by the European Union as their Earth Observation Programme. The programme will look at our planet and its environment to benefit all European citizens. The Sentinel satellites are built to fulfill the needs of the Copernicus programme, and they are developed by the European Space Agency (ESA). Copernicus is an cooperation between the member states of the European Union and its data policy assure full, open and free-of-charge access to Copernicus data and information. The programme is built up around six main categories: land management, the marine environment, atmosphere, emergency response, security and climate change (ESA, 2020c). An important part of the Copernicus program is to provide scientific data to the research communities, but also provide information to normal citizens through a variety of products. One application of special interest for Norwegian inhabitants is the monitoring of potential dangerous regions for rock slides as a result from the Sentinel-1 mission (ESA, 2020b).

Several different missions are involved in the program, where each mission aims to provide insight in some of the above categories. The first satellite, Sentinel-1, was launched back in April 2014 (ESA, 2020c), and the last satellite, now re-named as Sentinel-6 Michael Freilich[1], was launched into orbit on 21. November 2020. One of the main treats of climate change is sea level rise. Over 10 % of the world's population living less than 10 meters above sea level (ESA, 2020a) and continuous measurements of sea surface height (SSH) are by these means of crucial importance. Sea level rise has had a rate of 3.6 cm per decade, and its trend is accelerating even faster in recent years (ESA, 2020a). Since 1993 satellite altimetry missions have observed the Earth's water bodies, mainly the open ocean waters. Improvements in observation techniques and analysis strategies for satellite altimetry has in the more recent times made it possible to also observe the Earth's inland water bodies. ERS-1, as the first altimetry mission, was launched back in 1991 starting the continuous observation and monitoring of sea level. An overview of historical and planned satellite altimetry missions is shown in figure 1.2. Each altimetry mission has contributed to the observation of sea level resulting in a continuous observation period of over 25 years. With an increasing focus and developments in observations techniques, sea level rise can now be measured with mm-level accuracy (Abdalla et al., 2021). Since 1993 vast developments in many fields has occurred, but hardly any as explosive development as in the field of global navigation satellite systems (GNSS). As will be shown in section 5.1, improvement in the satellite's position directly affects the solution of any altimetry derived product. Figure 1.3 shows the historical improvement of accuracy in orbital and altimetry errors, where the accuracy of both components hs improved by a factor of almost 100 and 10, respectively. The Sentinel-6 satellite shows even further improvement in accuracy, which is explained by the development in observation techniques and positioning of the satellite (ESA,

---

[1]Named in honour after the director of NASA's Earth Sciences Division Michael Freilich.

Figure 1.1: Different categories and services included in the Copernicus programme. Satellite altimetry mainly contributes to the investigation of climate change.

2020e). Sentinel-6 is the first altimetry satellite able to receive both Galileo and GPS signals. In addition to surveillance of sea level change, satellite altimetry can provide measurements of mean sea surface (MSS), mapping of dynamic ocean topography (DOT) and also provide measurements used in gravity field modelling.

Satellite altimetry observes SSH and its temporal variations. As will be described in following sections, the sea surface is mainly affected by the Earth's gravity field and time varying ocean topography. If the SSH measurement can be reduced for the time-varying oceanic effects, then the altimetry observations can provide information about the Earth's gravity field. The geoid is determined as an equipotential surface coinciding with an undisturbed sea surface (Barthelmes, 2009). This equipotential surface makes the foundation for height systems, and thus is of high importance in geodesy. By using global models for reducing known long-wavelength components the SSH measurement a residual geoid height signal can be isolated. This signal can in turn be used to derive gravity anomalies and provide information about the Earth's gravity field. Different techniques can be applied for predicting gravity anomalies from residual geoid, e.g., Molodensky[2]'s equation, inverse Vening Meinesz equation or *least-squares collocation* (LSC). This thesis will focus on the transition from altimetry observations to gravity anomalies using the LSC approach.

After a theoretical study of possible estimation techniques has been done, a numerical investigation will be carried out based on datasets of mean sea surface (MSS) (Andersen et al., 2018), mean dynamic topography (MDT) (Andersen et al., 2016) and a gravity field solution (Andersen et al., 2014), where all datasets are originating from the Technical University of Denmark (DTU). As this thesis focuses on the use of altimetry observation for marine gravity field modelling, all topics relating to processing, error sources and realization of a MSS, will not be treated here. Those topics are for sure of great importance, and at NMBU a fellow M.Sc. student in geomatics is currently writing a master thesis on how artificial intelligence and machine learning can be exploited on classification of Sentinel-3 radar pulses in the Norwegian coastal zone. It is very complex to distinguish between observations affected by land contamination and undisturbed measurements in the coastal zone. Correctly classifying altimetry observations will become even more important with the satellite's reduced footprint on ground. A smaller footprint allows for observations even closer to the coast, and then in order to fully exploit the potential of satellite altimetry, improvement in classification and handling of error sources are necessary. Estimation of gravity anomalies from altimetry observations is an established geodetic technique where detailed information can be

---

[2]Named after the Soviet geodesist Mikahil Sergeevich Molodenskii (1909-1991)

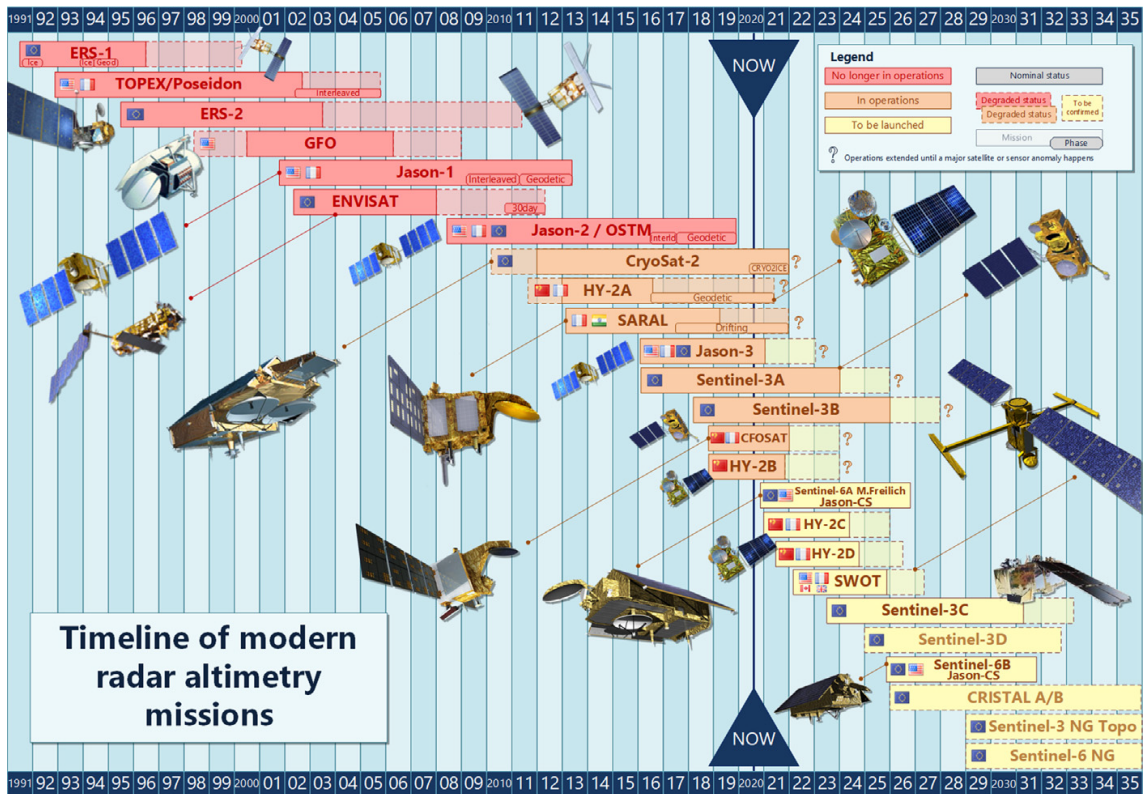Figure 1.2: Historical overview of satellite altimetry missions launched since 1991. Overlap between the missions is necessary to not introduce biases in the observation series. The figure originates from Abdalla et al. (2021).
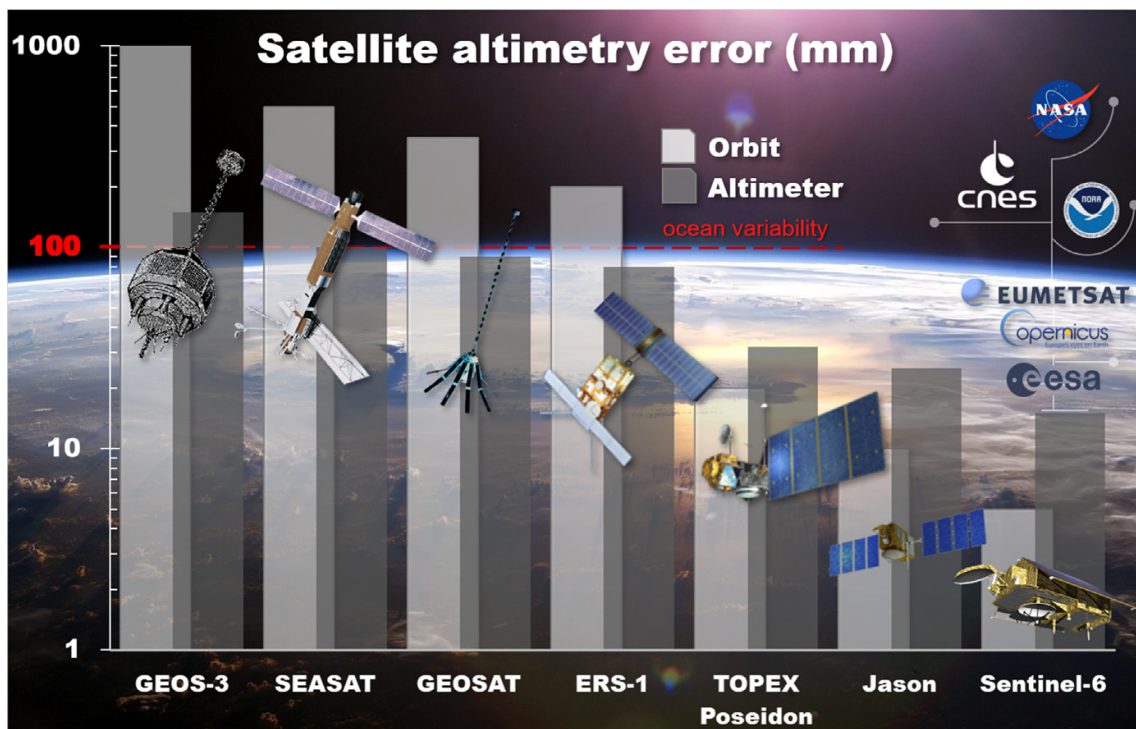

Figure 1.3: Representation of the development in orbital and altimetry errors for a number of selected satellite altimetry missions. The figure originates from Abdalla et al. (2021).

found in Stammer and Cazenave (2017). A regional application, which in many ways serves as a theoretical guideline for the implementation of LSC in this thesis, was recently done by Nguyen et al. (2020). However, adaptations in covariance modelling to fit Norwegian conditions for selecting the different components in LSC have been necessary.

LSC is a numerical method developed by T. Krarup in 1969 (Krarup, 1969), and further exploration and application to geodesy was later done by H. Moritz (Moritz, 1980) and published in 1980. LSC has in the recent years become a well used method in the field of physical geodesy, and especially when it comes to regional gravity field modelling. Through a special syllabus before the start on this master thesis a study of LSC was done (Dale, 2021). A detailed explanation on LSC can be found in a variety of books on physical geodesy (Moritz, 1980; Hofmann-Wellenhof and Moritz, 2006; Andersen, 2013). In addition several articles, on global and regional gravity field modelling, e.g., Willberg et al. (2019); Zingerle et al. (2020), provide an useful insight in LSC. All these resources together with articles on covariance modelling, e.g., Knudsen (1987); Heydarizadeh Shali et al. (2020), form the theoretical background of this master thesis.

Application of LSC is especially useful when it comes to combining different observation types. In addition to measurements of the Earth's global gravity field from space, also terrestrial measurements are performed on or near the Earth's surface. Commonly the Earth's gravity field is represented using spherical harmonics as basis functions, and when it comes to how the spherical harmonic coefficients are estimated, the terrestrial measurements, i.e., measurements by ship, airborne or ground data, and satellite observations have different strengths. The satellite data is well suited for observing the long to medium wavelengths of the gravity field, while ground data is suitable for detecting short wavelength part of the gravity field signal. With the increasing number of satellites, and also dedicated gravity missions such as CHAMP, GRACE, GOCE and most recently GRACE-FO, a high resolution and accurate global geopotential model (GGM) is now possible to obtain. By both having a set of global and regional gravity measurements, then a natural question would be how these measurements could be combined in an optimal way. The motivation for combining the two datasets could either be to improve a global gravity field model by terrestrial gravity field data, or to support a regional geoid solution with the global model. With a new global gravity model coming up, EGM2020 originally planned for 2020, a lot of research is ongoing with a goal to answer how this combination can be done optimally, and also on other questions regarding the estimation procedure, e.g. Willberg et al. (2020).

Observations of the Earth's gravity field over the entire earth are seeked when working with global gravity field modelling. With the recent satellite gravity missions a large increase of gravity observations has taken place during the last 20 years. Water covers over two-thirds of earth's surface, and by this fact satellite altimetry is a technique with great potential in gravity field modelling. The observations used in global gravity field modelling origins from satellite gravity missions, satellite altimetry, in combination with terrestrial or airborne gravity campaigns. The most recent GGMs are calculated using relative weighting accounting for the difference in accuracy between the above mentioned observation techniques. Satellite altimetry through its multi-mission processing contributes to a consistent data set of high accuracy (Fecher et al., 2017).

1.1 Primary goal for this thesis

The main goal for this master thesis is to derive gravity anomalies altimetric in the coastal zone and see if they can improve the marine geoid. On a global scale the Earth's gravity field is most commonly described using a spherical harmonic series expansion up to a maximum degree N_{max}, and today these models have a maximum degree of $N_{max} = 5540$ which corresponds to a spatial resolution of around 4 km. In regional areas, a gravity field model with higher spatial resolution can be obtained by combing local measurements with the global gravity field model. Collecting measurements of the Earth's gravity field in regional areas can be done from terrestrial, airborne or ship campaigns, and the Norwegian geoid is computed from a set of terrestrial measurements with higher accuracy on land than in oceanic areas. Due to observational gaps in the datasets a degradation of the geoid's accuracy occurs in the coastal regions. Norway, similar to other countries, has the majority of its population located in coastal regions, and thereby a precise geoid

in this area is of high interest. A precise geoid is also important in the transition between different vertical datums (height references), as the geoid forms a natural reference surface for physical heights, used on ocean and land. The development of new altimetry satellites and observation techniques allows today for altimetric observations closer to the shore than previously. In this thesis, gravity anomalies are determined using LSC on residual geoid heights deduced from satellite altimetry observations. First the implementation and simulation is performed in an area outside of the Norwegian coast, not affected by coastal effects. Here the collocation result is compared and verified with gravity anomalies from an external gravity field solution, DTU13GRA (Andersen et al., 2014), released by the Technical University of Denmark (DTU). Next the prediction of gravity anomalies is carried out in a testbed at Sunnmøre along the Norwegian coast. In this testbed the Norwegian Mapping Authority (MNA) has made available shipborne gravimetric observations .

Chapter 2

Earth's gravity field

Extensive literature about the Earth's gravity field can be found, and especially the book by Hofmann-Wellenhof and Moritz (2006) has been used for the theoretical background for this thesis. A more compact and less mathematical source, still giving a fairly good understanding of the different components of the Earth's gravity field can be obtained from ICGEM (2019).

The Earth's gravity field can be described using Sir Isaac Newton's law of universal gravitational

$$\vec{F}_g = -\frac{GMm_0}{r^2}\frac{\vec{r}}{r},$$

(2.1)

where G is the Newton's gravitational constant, $G = 6.6742 \times 10^{-11}\,\mathrm{m^3\,kg\,s^{-1}}$, and the two point masses M and m_0 are separated by a distance of $r = |\vec{r}|$. Conservative forces, such as the gravitational force $\vec{F}_g$, can be described through the gradient of a scalar field $\nabla V = \vec{F}$, where V is the gravitational potential. Working with a scalar quantity is easier than through a vector field representation. As is pointed out in ICGEM (2019), the total gravity field consist of components from a gravitational and centrifugal part. The gravitational field is a conservative vector field, which means that no energy is changed if a body moves back and forth between points P and Q. In conservative vector fields the potential energy can be defined to be path independent, and mathematically this is stated as the vector field to be rotationally invariant, i.e., rot $\vec{F} = \mathrm{curl}\vec{F} = \nabla \times \vec{F} = 0$.

The work for moving a unit mass m_0 in the gravitational field generated by a point mass M is given by

$$W = \int \vec{F} \cdot d\vec{r} = \int m_0 \cdot \vec{a} \cdot d\vec{r} = \int \vec{a} \cdot d\vec{r} \Rightarrow W = \int -G\frac{M}{r^2}dr.$$

(2.2)

The gravitational potential V of the mass M is the amount of work necessary to move the particle from infinity to a given distance r

$$V = \int_{\infty}^{r} -\frac{GM}{r^2}dr = -GM \int_{\infty}^{r} \frac{1}{r^2}dr = -GM\left[\frac{1}{\infty} - \frac{1}{r}\right] \rightarrow V = \frac{GM}{r}.$$

(2.3)

From equation (2.3) it can be seen that $\nabla V = \vec{F}$

$$\nabla V = \frac{dV}{dr} = \frac{d}{dr}\left(\frac{GM}{r}\right) = -\frac{GM}{r^2}\frac{\vec{r}}{r} = \vec{F}.$$

(2.4)

In a system with many attracting masses continuously distributed over a volume v, the gravitational potential, given by equation (2.3), will result in an integral

$$V = \iiint_v \frac{dm}{r} = G \iint_v \frac{\rho}{r} dv, \tag{2.5}$$

which also is known as Newton's integral. If the Earth's density ρ distribution would have been precisely known, then the potential at an arbitrary location $P = (\varphi, \lambda, h)$ could have been calculated using equation (2.5). However, the Earth's density distribution is not known with required accuracy, and thus a different approach needs to be taken in order to obtain potential values. The gravitational potential V can be shown to satisfy *Poisson's* differential equation

$$\Delta V = -4\pi G \rho, \tag{2.6}$$

and outside of the attracting bodies the density is $\rho = 0$, and a special case of Poisson's equation, known as *Laplace's* partial differential equation, results

$$\Delta V = 0. \tag{2.7}$$

All solutions of equation (2.7) are called *harmonic functions*. Since the gravity field of the Earth is sought, the solution on arbitrary locations on a sphere, or an ellipsoid, would be preferable. In order to obtain such a solution, the Cartesian coordinates are transformed to spherical coordinates and Laplace's equation is solved by a separation of variables. A detailed description of the derivations and solutions of equation (2.7) will not be given here, for further details I will refer to Hofmann-Wellenhof and Moritz (2006).

By using separation of variables, three one-dimensional functions depending on r, θ and λ are obtained. The result of the derivation is a set of equations, one representing the solution inside the sphere, and one solution outside the sphere. Only the solution outside of the sphere is of interest, for a solution inside the sphere the appropriate solution should fulfill Poisson's equation. The gravitational potential of the Earth can be expanded into a series of spherical harmonics, which is solely a mathematically solution of Laplace's differential equation. In spherical coordinates the series expansion is given by

$$V(r, \theta, \lambda) = \sum_{n=0}^{\infty} \frac{1}{r^{n+1}} \sum_{m=0}^{n} \left[a_{nm} \cos m\lambda + b_{nm} \sin m\lambda \right] P_{nm}(\cos \theta), \tag{2.8}$$

where $\{a_{nm}, b_{nm}\}$ is the spherical harmonic coefficients of degree n and order m, and P_{nm} is the associated Legendre functions.

To determine the potential at arbitrary location in space at a point $P = (r, \theta, \lambda)$ from known spherical harmonic coefficients $\{a_{nm}, b_{nm}\}$ is called *spherical harmonic synthesis* (SHS), and will be the only application used in this thesis. To determine spherical harmonic coefficients based on observations of gravity functionals, i.e., quantities that can be derived from the gravity field, is known as *spherical harmonic analysis*. This thesis only focuses on SHS, where global geopotential models (GGM) are selected from the International Centre for Global Earth Models (ICGEM). Further details about GGMs will be given in section 2.2.

The gravity field is the sum of the Earth's gravitational attraction and the centrifugal force (ICGEM, 2019). Hence, the gravity potential W is the sum of the gravitational potential V and the centrifugal potential Φ:

$$W = V + \Phi, \tag{2.9}$$

where the centrifugal potential is accurately given by

$$\Phi = \frac{1}{2}\omega^2 d^2, \tag{2.10}$$

with d representing the distance between the point and the Earth's rotational axis. The gravity acceleration, which again is a sum of the gravitational and centrifugal acceleration, can be determined by taking the gradient of the gravity potential W.

$$\vec{g} = \operatorname{grad} W. \tag{2.11}$$

The geoid is defined as the equipotential surface that coincides with the undisturbed sea surface (Barthelmes, 2009). An equipotential surface is a surface where the potential is constant, and accordingly the geoid can be defined by assigning this equipotential surface with a value by

$$W = W_0 = \text{constant.} \tag{2.12}$$

The geoid, defined by its value W_0, will be used in the following for forming a normal gravity field fulfilling some specific criteria.

2.1 The normal gravity field or normal potential

The entire Earth's true gravity potential W could have been modelled, but large parts can instead be calculated using a geometrical and physical model of the Earth. By approximating the Earth with a rotating ellipsoid, large parts of the true gravity potential W can be reduced by the gravity potential U generated from this mathematical Earth model. An ellipsoid is convenient to use, because of its fairly simple mathematical description, but it also approximates the true gravity field very well (Hofmann-Wellenhof and Moritz, 2006). Approximately 99.9996% of the Earth's total gravity field can be accounted for by the normal gravity potential according to Jekeli (2015). By introducing this normal potential, the Earth's true gravity potential W can be written as

$$W = U + T, \tag{2.13}$$

where T is called the disturbing potential and describes the remaining signal parts not represented by the normal potential generated from the mathematical representation of the Earth's gravity field. The rotational ellipsoid is formed such that it fits with the definition of the geoid. In order to do so, the ellipsoid must be constructed as an equipotential surface in the normal gravity field. This equipotential surface with a value of $U = U_0$ should approximate the geoid as good as possible. From this statement the value of U_0 is defined as

$$U = U_0 = W_0. \tag{2.14}$$

A rotating ellipsoid, and accordingly a normal gravity field, is defined by the following 4 parameters (Hofmann-Wellenhof and Moritz, 2006):

- The angular velocity of the Earth ω

- The shape of the reference ellipsoid given by a and b, or one of them in combination with the ellipsoids flattening $f = \frac{a-b}{a}$

- The value $U_0 = W_0$.

As was described in section 2, the gravity field consists both of gravitational and centrifugal components. The normal gravity field's centrifugal component, in the same way as for the true gravity field, can be calculated from the analytical formula given in equation (2.10). The disturbing potential can then be written as

$$T = W - U = (V + \Phi) - (V^N + \Phi) = V - V^N, \tag{2.15}$$

where V^N is introduced as the gravitational component of the normal gravity field. If the rotational ellipsoid is selected such that it rotates with the same angular velocity ω, then it can clearly be seen from equation (2.15) that the centrifugal potential cancels out when forming the disturbing potential. ICGEM (2019) points out that there exists a mixture of terms in the literature to denote W: global gravity field models, global geopotential models and global gravitational models. The reason for this mixture is probably relating to that the centrifugal component can be calculated precisely with an analytical formula, here again referring to equation (2.10). Still, since the gravity field consists of both a gravitational and centrifugal component, throughout this thesis the global models will be denoted as global geopotential models (GGM).

The normal gravity field can also, in the same way as for the gravitational potential of the Earth, be represented with a spherical harmonic series expansion

$$V^N(r, \theta, \lambda) = \frac{GM}{R} \sum_{n=0}^{\infty} \left(\frac{R}{r}\right)^{n+1} \sum_{m=0}^{n} \left(\bar{C}_{nm} \cos m\lambda + \bar{S}_{nm} \sin m\lambda\right) \bar{P}_{nm}(\cos \theta). \tag{2.16}$$

Due to symmetrical properties of the rotating ellipsoid, the normal gravitational field does only depend on latitude. This also implies that the series expansion can only consist of terms invariant of longitude, and only zonal harmonics which have an order of $m = 0$ fulfill this property. Since the field also is symmetric with respect to the equator, it can only consist of zonal harmonics of even degree $n = \{0, 2, 4, ..\}$ (Gerlach, 2019). Taking all these properties into account, the normal gravitational potential can be represented by

$$V^N(r, \theta, \lambda) = \frac{GM^N}{R^N} \sum_{n=0(2)}^{\infty} \left(\frac{R^N}{r}\right)^{n+1} \bar{C}_{n0}^N \bar{P}_{n0}(\cos \theta), \tag{2.17}$$

where normalised spherical harmonic coefficients $\{\bar{a}_{nm}, \bar{b}_{nm}\}$ and normalised associated Legendre functions $\bar{P}_{nm}$ are used.

The disturbing potential T can be calculated according to equation (2.15), and using the spherical harmonic series expansion representation of the respective gravitational potentials leads to

$$T(r, \theta, \lambda) = \frac{GM}{R} \sum_{n=2}^{\infty} \left(\frac{R}{r}\right)^{n+1} \sum_{m=0}^{n} \left(\Delta\bar{C}_{nm} \cos m\lambda + \Delta\bar{S}_{nm} \sin m\lambda\right) \bar{P}_{nm}(\cos \theta). \tag{2.18}$$

The Δ-coefficients $\{\Delta\bar{C}_{nm}, \Delta\bar{S}_{nm}\}$ are the difference in spherical harmonic coefficients between the true gravitational field V and the normal gravity field V^N

Table 2.1: The dimensioning factor D^f and spectral eigenvalue λ_n^f for different gravity functionals. In addition, the cosine and sine part of the general expression, given by equation (2.22), using spherical-harmonic series expansion of the anomalous potential T is represented.

$f(T)$	D^f	λ_l^f	K_{nm}^C	K_{nm}^S
T	GM/r	1	$\Delta\bar{C}_{nm}$	$\Delta\bar{S}_{nm}$
$-\delta g$ or T_r	$-GM/r^2$	$(l+1)$	$(n+1)\Delta\bar{C}_{nm}$	$(n+1)\Delta\bar{S}_{nm}$
T_{rr}	GM/r^3	$(l+1)(l+2)$	$(n+1)(l+2)\Delta\bar{C}_{nm}$	$(n+1)(l+2)\Delta\bar{S}_{nm}$
ζ or N	R	1	$\Delta\bar{S}_{nm}$	$\Delta\bar{S}_{nm}$
Δg	GM/r^3	$(l-1)$	$(n-1)\Delta\bar{C}_{nm}$	$(n-1)\Delta\bar{S}_{nm}$

$$\Delta\bar{S}_{nm} = \bar{S}_{nm} \tag{2.19}$$

$$\Delta\bar{C}_{nm} = \begin{cases} \bar{C}_{n0} - \bar{C}_{n0}^N \text{ ; for } m = 0, n = \{2,4,6,8\} \\ \bar{C}_{nm} \text{ ; else} \end{cases} \tag{2.20}$$

From the disturbing potential it is possible to derive several different gravity field functionals. All quantities that can be derived from the gravity field are called *gravity field functionals*. These quantities are related to the distrubing potential T through linear functionals. An alternative, or more general expression, to express a functional $F(T)$ of the disturbing potential T can be written as

$$F(T) = D^f \sum_n \lambda_n \sum_m \bar{P}_{nm}(\cos\theta) \left[\Delta\bar{C}_{nm}\cos m\lambda + \Delta\bar{S}_{nm}\sin m\lambda\right], \tag{2.21}$$

where D^f and λ_n^f are the gravity functional's dimensioning factor and spectral eigenvalue, respectively. Another representation that can be obtained by including the spectral eigenvalues inside the summation sign, and accordingly obtained an expression for the functional $F(T)$ as

$$F(T) = D^f \sum_n \sum_m \bar{P}_{nm}(\cos\theta)[(\underbrace{\lambda_n\Delta\bar{C}_{nm}}_{=K_{nm}^C})\cos m\lambda + (\underbrace{\lambda_n\Delta\bar{S}_n m}_{=K_{nm}^S})\sin m\lambda]. \tag{2.22}$$

In table 2.1, a summary of gravity functionals and their corresponding dimensioning factor D^f and spectral eigenvalues λ_l^f is given. With dimensionless potential coefficients originating from a GGM, *degree variances* of different gravity functionals can be calculated using equation (2.22) by selecting the correct spectral eigenvalues λ_l^f and dimensioning factor D^f from table 2.1

Figure 2.1, known as a Meissl[1] schema, shows the spectral relationship between the disturbing potential and its first and second order derivatives T_r and T_{rr} at the Earth's surface $h = 0$ and at satellite altitude h. A closer investigation of figure 2.1 reveals that through its dependency on the spherical harmonic degree n, the higher order derivatives are more sensible for short wavelength components of the disturbing potential.

Another important part is that the prediction using LSC will follow the well known *remove-compute-restore* (RCR)-method, see further section 2.2.1. As LSC will be applied after the *remove*-step, then the covariance function should express the remaining signal's characteristics. Reduction of the signal by use of a GGM leads to a bandlimited $n = [N_{max}, \infty]$ residual signal. In case a high-resolution GGM is used, for example EGM2008 with a maximum degree of $N_{max} = 2159$, then the residual field will be bandlimited to $n = [2159, \infty]$. For $n > 2159$ there exist no potential coefficients, and the covariance function must be calculated by other means.

---

[1]named after the Austrian geodesist Peter Meissl
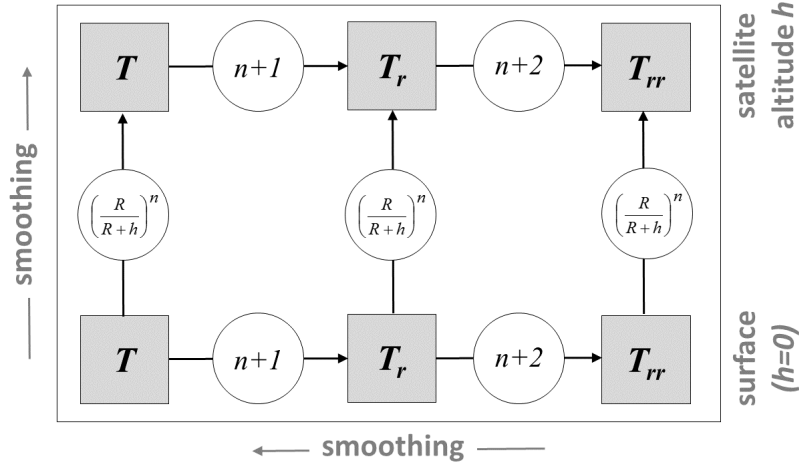
Figure 2.1: A Meissl schema representing the spectral relationship between the disturbing potential and its first and second order derivatives T_r and T_{rr} at the Earth's surface $h = 0$ and at satellite altitude h. The figure originates from Gerlach (2019).

2.2 Global Geopotential Models(GGM)

ICGEM provides the scientific community with GGMs and solutions from dedicated time periods. An approximation to the real gravity field can be developed through different mathematical representations, e.g., ellipsoidal harmonics, spherical harmonics, spherical radial basis function, or spherical harmonic wavelets (Ince et al., 2019). As was described in section 2, all the basis functions are harmonic and satisfy Laplace differential equation. The most common approach is to describe the Earth's gravity field by a spherical harmonic series.

A GGM is published through a set of spherical harmonic potential coefficients $\{\bar{C}_{nm}, \bar{S}_{nm}\}$, and in more recent times it contains also the standard deviations $\{\sigma_{\bar{C}_{nm}}, \sigma_{\bar{S}_{nm}}\}$ of the corresponding potential coefficients. In addition, the constants R and GM are published such that gravity functionals defined by the anomalous potential can be computed. Today, there exists both combined and satellite-only GGMs, where the latter only uses satellite data.

An increasing number of GGMs exists in the geodetic community. One of the most frequently used GGMs in the scientific community is EGM2008 (Pavlis et al., 2012). Since its publication in 2008, EGM2008 has served as a mathematical model of the Earth's gravity field supporting research fields like oceanography, unification of global height systems and orbit determination (Fecher et al., 2015). With the more recent specialised satellite gravity missions, CHAMP, GRACE, GOCE and latest GRACE-FO, an increasing number of observations has been collected since the publication of EGM2008 back in 2008. With an increase in observations and better processing strategies, comparison with GNSS-levelling shows that a 1 cm geoid from the combined GGM can be obtained in areas with a high quality terrestrial gravity dataset available (Gruber and Willberg, 2019).

At ICGEM's website, GGMs can be evaluated against each other, both in the spectral domain and by comparison with GNSS levelling. From the model coefficients of a GGM, geoid heights N at arbitrary locations can be derived by

$$N(\phi, \lambda)_{GGM} = \frac{GM}{\gamma r} \left[\sum_{n=2}^{N_{max}} \left(\frac{R}{r} \right)^n \sum_{m=0}^{n} (\bar{C}_{nm} \cos(m\lambda) + \bar{S}_{nm} \sin(m\lambda)) \bar{P}_{nm}(\sin \phi) \right], \qquad (2.23)$$
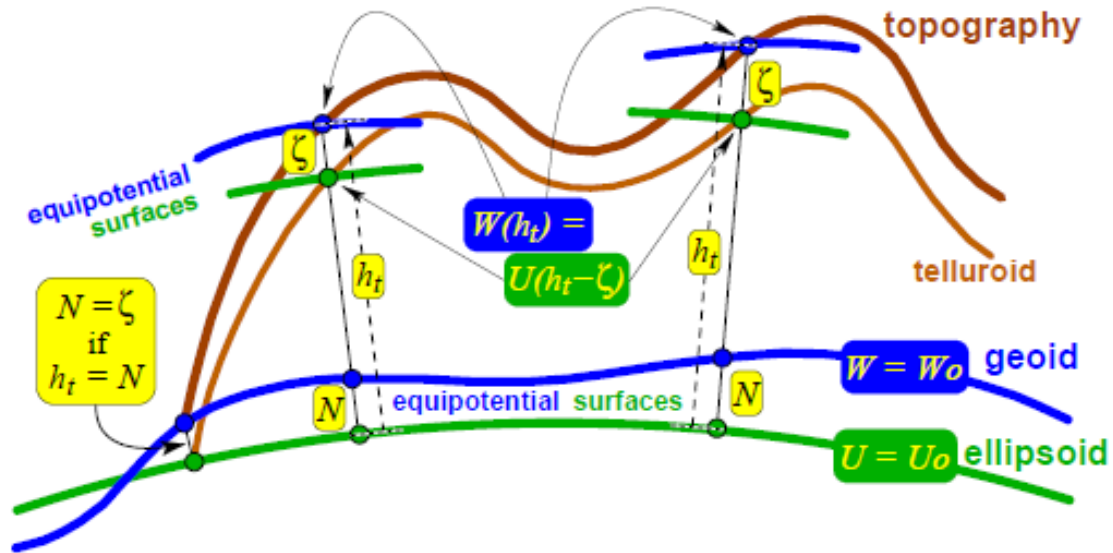
Figure 2.2: A geometrical representation of the difference between height anomaly ξ and geoid height N. The height of the topography h_t refers to the ellipsoid. For areas where $h_t = N$ (or $H = 0$) the quasigeoid and geoid coincide. The figure originates from Barthelmes (2009).

where the transition from disturbing potential T to geoid height N is described by the famous Bruns[2]' formula

$$N = \frac{T}{\gamma}, \tag{2.24}$$

where γ is the normal gravity generated by the normal potential field V^N. Equation (2.23) expresses the geoid height N using an assumption that at the sea surface the quasigeoid coincides with the geoid as shown by figure 2.2. This assumption is certainly of great importance as the Norwegian height system NN2000 is based on normal heights, which in turns refers to the quasigeoid. Without going into details about the Stokes's and Molodensky's theory, the assumption holds because of absent in topographic masses above the point P when it is located in open-waters on the sea surface. Using the same assumption for NN2000 means that these heights will coincide with the geoide at sea.

An independent set of geoid height can be obtained at benchmark points which has been observed both by geodetic levelling and GNSS according to

$$N_{geom} = h - H, \tag{2.25}$$

where the ellipsoidal height h is observed with GNSS and the orthometric height H is observed from geodetic levelling. To finish off the discussion about difference between the quasigeoid and geoid, it is noted that in case the heights H would have referred to NN2000, then equation (2.25) would result in quasigeoid heights ξ_{geom}. By forming the difference in geoid height from the two different approaches, an external evaluation of the different GGMs can be performed by comparison of

$$\epsilon_{\Delta N} = N_{GGM} - N_{geom}. \tag{2.26}$$

[2]Named after the German mathematician Ernst Heinrich Bruns (1848-1919).

As this comparison method depends on the access to benchmark points, it is well suited for local or regional evaluation of a GGM from comparison with national GNSS-levelling datasets. The validation results from ICGEM do not take into account the different error sources in equation (2.25), so the comparison result will only be as good as the quality of the resources, global gravity field model, and GNSS-levelling derived geoid undulation (Ince et al., 2019). Still, the comparison will give a good estimate of the GGM quality. Gruber and Willberg (2019) provide a more detailed description and analysis on comparison of recent GOCE-based gravity field models and pre-GOCE models. In addition, they investigate how GNSS-levelling can be used to investigate possible systematic errors in the global models, in the spirit levelling and in the GNSS height observations. Their approach is also used by Zingerle et al. (2020) for comparison of recent high-resolution GGMs.

In this thesis, GOCO06s (Kvas et al., 2021), EGM2008 (Pavlis et al., 2012) and XGM2019e2159 (Zingerle et al., 2020) will be used as GGMs in the *remove-compute-restore*(RCR) approach. GOCO06s is the most recent satellite-only model, and is modelled up to a maximum degree of $N_{max} = 300$. EGM2008 and XGM2019e2159 are high-resolution GGMs with a maximum degree of $N_{max} = 2190$. The three models' RMS-value compared to a global GNSS-levelling dataset at ICGEM are reported to be 0.3341 m, 0.1877 m and 0.1732 m for GOCO06s, EGM2008 and XGM2019e2159, respectively. Zingerle et al. (2020) show that XGM2019e2159 is the most consistent model, and it also posses the lowest RMS-value among the models evaluated by ICGEM. EGM2008 is included because it still serves as a reference GGM. Recent studies, such as Zingerle et al. (2020); Gruber and Willberg (2019), has showed that recent GGMs perform better than EGM2008 in most regions, where the improvement is largely explained by inclusion of new GOCE-data and updated terrestrial datasets.

Even though no detailed description or derivation has yet been given on how LSC will be used for predicting gravity anomalies, I still consider a short description on the application of GGM in the *remove-compute-restore* (RCR)-method to be appropriate.

2.2.1 Remove-compute-restore (RCR)-method

The RCR-method is a well used estimation technique in physical geodesy. These steps account for the removal and restoring of known signal components of the Earth's gravity field. A GGM represented through a spherical harmonic expansion with maximum degree of N_{max} can resolve signal components with a spatial resolution given by

$$\lambda_{max} = \frac{20\,000\,\text{km}}{N_{max}}. \tag{2.27}$$

Vice versa, the spatial resolution of the observations defines the maximal degree N_{max} which can be determined from an observed dataset (Fecher et al., 2015). The removal of the signal's long wavelength components allows for a close investigation on the short wavelength characteristics of the signal to take place. According to the RCR-method the residual signal will be bandlimited to $N = [N_{max}, \infty]$. This is not 100% true, but for now this holds as a fact. A more detailed description and treatment of the residual signal's spectral characteristics will be treated in section 5.1. In principle, the same signal parts will be added back after the LSC prediction to recreate the full signal using equation (2.28), so the selection of a GGM was initially expected to not be of great importance. However, as part of a preprocessing step, Nguyen et al. (2020) uses GNSS-levelling comparison, similar to the approach found in Ince et al. (2019), to assure that the best GGM in the area under consideration is used. The analysis done by Gruber and Willberg (2019) is to be considered as best guidelines. Instead of direct comparison between GNSS levelling and geoid heights derived from a GGM, Gruber and Willberg (2019) applies a planar correction for reducing systematic effects such as biases and tilt in the regional GNSS levelling datasets. Comparison of geoid heights derived from the GGMs and GNSS-levelling at benchmarks goes beyond this thesis, but by using three different GGMs, EGM2008, XGM2019e2159 and GOCO06s, then potential effects relating to the model selection should become visible.

Today EGM2008 (Pavlis et al., 2012) is the most used GGM, while in near future a new release, EGM2020, will be available. Reduction by a GGM gives a more homogeneous and smooth signal than the original geoid signal, and several studies, such as Andersen (2013); Willberg et al. (2019), have shown that using LSC on the residual signal gives favourable results.

A modified approach named residual least-squares collocation (RLSC) has been developed by Willberg et al. (2019), where RLSC uses error-covariance matrices instead of signal covariance matrices. Willberg et al. (2019) shows by a numerical closed-loop simulation of regional geoid modelling that RLSC achieves better results than standard LSC. They points out that the favourable results comes of how the residual signal fulfills the stochastic properties compared with the full signal.

After the prediction of gravity anomaly by LSC is carried out, then the gravity field signal's long wavelength is added back again in form of gravity anomalies derived from SHS as

$$\Delta g(\theta, \lambda) = \frac{GM}{R^2} \sum_{n=2}^{N_{max}} (n-1) \sum_{m=0}^{n} (\Delta \bar{C}_{nm} \cos m\lambda + \Delta \bar{S}_{nm} \sin m\lambda) P_{nm}(\cos \theta), \tag{2.28}$$

with $\{\Delta \bar{C}_{nm}, \Delta \bar{S}_{nm}\}$ the dimensionless normalised potential coefficients of the anomalous gravity field and $\bar{P}_{nm}$ the associated Legandre functions of degree n and order m. This equation states that the gravity anomaly at a point $P(\theta, \lambda)$ is based on a sum of productse between spherical harmonic coefficients and the corresponding associated Legendre functions. A more compact form of the gravity anomalies Δg can be obtained by introducing two new variables

$$\bar{R}_{nm} = \bar{P}_{nm} \cos m\lambda \tag{2.29}$$
$$\bar{S}_{nm} = \bar{P}_{nm} \sin m\lambda, \tag{2.30}$$

and then the spherical harmonic representation of gravity anomalies Δg, given by equation (2.28), can be written as

$$\Delta g = \frac{GM}{R^2} \sum_{n=2}^{\infty} (n-1) \sum_{m=0}^{n} \left(\Delta \bar{C}_{nm} \bar{R}_{nm} + \Delta \bar{S}_{nm} \bar{S}_{nm} \right). \tag{2.31}$$

The above expression for gravity anomalies will be very convenient when the covariance function $C^{\Delta g}(\psi)$ is derived by using a spherical harmonic expansion.

2.2.2 Degree variances

From equation (2.27) it is evident that potential coefficients of different degree n resolves different signal components with different spectral characteristics. How much a spherical harmonic coefficient of a certain order contributes to the gravity field's total signal variance can be expressed by

$$c_n = \sum_{m=0}^{n} \left[\Delta \bar{C}_{nm}^2 + \Delta \bar{S}_{nm}^2 \right], \tag{2.32}$$

where c_n are the dimensionless degree variances. The degree variances give information on the spectral distribution of signal power (squared amplitude), i.e., they tell us which degrees (which spectral band) contribute most to the signal (Gerlach and Ophaug, 2021). In section 5.1.7, see for example figure 5.12 for GOCO06s, it can clearly be seen that potential coefficients of higher degree

contribute less to the total signal variance. By using a satellite-only model, such as GOCO06s, with lower spatial resolution it is possible to obtain a higher signal-to-noise ratio for the reduced signal. In order to increase the signal-to-noise ratio, also the high-resolution GGM has been truncated to a maximum degree of $N_{cut} = 1000$. In the service provided by ICGEM (`http://icgem.gfz-potsdam.de/calcpoints` -last accessed: 27.03.2021) no gentle truncation of the model is applied. The different ICGEM-services, especially the one which allows for calculation of gravity functionals from a specific GGM at user-defined points, have provided essential support in the work with this thesis.

2.2.3 Commission error

The GGM is a mathematical representation, i.e., an approximation, of the Earth's gravity field and it will accordingly also contain modelling errors. In addition to the set of potential coefficients, the GGM contains a corresponding set of standard deviation for the potential coefficients. The error standard deviation of a certain GGM up to a given degree N is calculated in a similar way as degree variances

$$\sigma_{com} = \sqrt{\sum_{m=0}^{N} \left[\sigma_{\bar{C}_{nm}}^2 + \sigma_{\bar{S}_{nm}}^2 \right]}, \qquad (2.33)$$

where standard deviations of the potential coefficients $\{\bar{C}_{nm}, \bar{S}_{nm}\}$ are used, instead of the potential coefficients themselves as in the case of degree variances. The value calculated using equation (2.33) is commonly called the *commission error* of the model (Gerlach, 2019). The maximum resolution of a GGM is defined where the commission error surpasses the signal strength.

2.2.4 Omission error

Another quantity which is of relevance when working with GGMs is the *omission error*. The signal content above the maximum degree N_{max} of a GGM, addresses the omission error (Gerlach, 2019). It represents the signal strength in the spectral band above the maximum degree of the GGM. Normally, a GGM is used up to its maximum degree N_{max}, but in this thesis, a truncation of the GGM to a lower spherical harmonic degree N_{cut} is done in an attempt to increase the signal-to-noise ratio. This also allows the signal content above N_{cut} to be modelled using the potential coefficients of a high-resolution GGM in the spectral band $N_{cut} < N \leq N_{max}$. Above the GGM's maximum degree N_{max} there exist no potential coefficient usable for calculating the degree variance, then the omission error needs to be calculated by other means. Several models exists for modelling the degree variance c_n above the GGM's maximum degree. Two examples of degree variance models are the model derived by Kaula (1966):

$$c_n \approx \frac{1 \cdot 10^{-10}}{n^3}, \qquad (2.34)$$

which provides dimensionless degree variances, and another possibility is to derive degree variances of the anomalous potential T using the model by Tscherning and Rapp (1974):

$$c_n(T,T) = \frac{A(n-1)}{(n-2)(n+B)} \qquad (2.35)$$

valid for $n > 2$. Degree variances for other gravity functionals are obtained by combining the appropriate dimensioning factor and spectral eigenvalue. In Nguyen et al. (2020) and Knudsen

(1987) the Tscherning/Rapp covariance model, as given by equation (2.35) is used to calculate degree variance for $N > N_{max}$, and it is also selected as the preferable choice within this thesis. As the model parameters A and B are highly correlated, B is fixed to a value of 24, which is also the value selected by Knudsen (1987), while Nguyen et al. (2020) uses a value of 4. Initial tests, not shown here, confirms that fixing the value of B to a specific value has no significant effect since A will then be scaled accordingly. A more detailed explanation about the covariance modelling will be given in section 5.1.7.

Chapter 3

Least-squares collocation (LSC)

LSC was already implemented on computers in the early 1960s (Tscherning, 1972). With entering into the era of supercomputers some previous estimation techniques can now be used for gravity field modelling. LSC, due to its high computational demand, is one of those techniques who has gained on the improvements in computational powers. Even today, global gravity field modelling challenges the computational bounds of supercomputers (Pail et al., 2017). As described in section 2.2.1, the RCR-method is popularly used for regional gravity field modelling. The method uses a GGM for removing and restoring the long wavelength components of the Earth's gravity field. When working with LSC the underlying assumption is that we assume the signal to be stochastic. This assumption means that (Gerlach and Ophaug, 2021):

- the signal does not contain any deterministic components (like trends or biases) and as such

- the signal fluctuates around zero (the function's mean value is zero) and is

- isotropic (no dependence on azimuth or direction) and

- homogeneous (signal characteristics do not vary from place to place)

Moritz (1980) showed that the anomalous gravity field of the Earth, T, may be described as a stochastic process, expressing its spatial variability. The signal strength of the Earth's gravity field reduces with altitude. This causes spaceborne observation techniques only to measure the medium and long wavelength components of the Earth's gravity field. Terrestrial observations, on the other hand, can observe the full gravity signal, and thereby also observe the gravity field's short wavelength components. In addition to observing different signal components of the gravity field, the observation techniques observe different types of gravity functionals. Tscherning (2001) states that LSC is well suited to handle different types of observed gravity functionals, where combination of the different gravity functionals is carried out according to their statistical relationship described through the auto-covariance and cross-covariance functions. A natural question would be how spaceborne and high-resolution terrestrial gravity data can be combined in an optimal way. An optimal combination of local (terrestrial) gravity data and global gravity models derived from satellite data is achieved by assigning relative weights based on their respective covariance matrices.

This thesis will focus on using a GGM for regional applications. The common way is to remove the gravity field's long-wavelength parts using a global model. After this removal is done, a local Tscherning-Rapp covariance model is fitted to the residual signal. When working with LSC, which is a statistical estimation technique, the signal must fulfill the given stochastic properties in order to give reliable results. In regional or local applications, the average of Δg is not necessarily zero. Large scale structures with wavelengths larger than the extent of the study area will show up as regional trends. Subtraction of a high-resolution GGM is applied to make sure the stochastic assumptions are met (Gerlach and Ophaug, 2021). To further reduce and ensure that no systematic effects are present relating to the global models, the residual signal should also be reduced by its mean value in the area of interest.

Large parts of this section is based on Dale (2021). First a brief introduction to the concept of covariance functions will be given, and afterwards least-squares prediction is derived. Further details about covariance functions, which is the key component in LSC, is given in section 4. At last, the expression for least-squares collocation is derived from Stokes's formula.

3.1 Deriving least-squares prediction

The geoid height can be calculated using Stokes[1]'s formula

$$N_P = \frac{R}{4\pi\gamma} \iint\limits_{\sigma} S(\psi_{PQ})\Delta g_Q d\sigma, \tag{3.1}$$

where geoid height N at the computation point P is derived by globally integrating gravity anomalies Δg weighted by the Stokes function $S(\psi)$. Gravity anomalies are only obtained at discrete points, but in order to apply Stokes equation a continuous representation of gravity anomalies is needed. Due to the fact that gravity anomalies are only obtained at discrete points, a way to predict gravity anomalies as a continuous function must be obtained. A suitable prediction method should both take signal variance and signal correlation into account, and a covariance function does exactly this.

In this section a derivation will be given on how least-squares-collocation(LSC) can be used for predicting gravity anomalies Δg from residual geoid heights ΔN. First an introduction to what a covariance function is given, and next how the covariance function builds the foundation for creating an optimal prediction method with respect to average prediction error.

3.1.1 The idea of a covariance function

In general, when selecting an interpolation method good knowledge of the target quantity's behaviour is important. All the following derivations will be shown using gravity anomaly Δg as an example, but it is of course valid for any other quantity. As has already been stated, gravity anomalies Δg are only measured at discrete points on the earth's surface. To predict gravity anomalies in an optimal way would be preferable. When searching for such a method then its performance on the entire earth's surface should be investigated. If the normal gravity field is created from an ellipsoid with the same mass as the earth, and the same potential as the geoid, then the global average of the gravity anomaly Δg will be 0. Mathematically this is stated as

$$M\{\Delta g\} = \frac{1}{4\pi} \iint\limits_{\sigma} \Delta g \, d\sigma = 0, \tag{3.2}$$

where the integration is done over a unit sphere with area σ and M denotes the average operator. A better impression on how a function behaves can be obtained by calculating the product of two distinct points' function values. The covariance function characterizes the statistical correlation between a quantity's value at two points separated by a distance ψ. Creating products for all point pairs separated by a certain distance ψ, and then taking the average for all observation pairs separated by the same distance over the entire earth's surface leads to a one dimensional function only depending on the distance ψ called the covariance function

$$\text{cov}(\Delta g, \psi_{ij}) = \mathcal{M}\{\Delta g_i \Delta g_j\} = \frac{1}{4\pi} \iint\limits_{\sigma} \Delta g_i \Delta g_j d\sigma. \tag{3.3}$$

---

[1]Named after the Irish mathematician Sir George Gabriel Stokes (1819-1903

The variance is a special value of the covariance function at $C(s = 0)$, which of course implies that $\Delta g_i = \Delta g_j$. From statistics, variance describes the range of function values, while the function's smoothness can be described through the covariance or its normalized version, the correlation. The correlation length ϵ is commonly used to describe the smoothness of a function, and it is defined as the distance where the covariance function has dropped to half of its maximum value, mathematically stated as

$$C(\epsilon) = \frac{1}{2}C_0. \tag{3.4}$$

3.1.2 Interpolation

Now a short look will be taken on the application of a covariance function $C(\psi)$ in LSC. As briefly explained earlier, good knowledge of a function's behaviour is necessary to come up with a good approximation. In section 3.1.1 a statistical approach was used to describe a signal through its covariance function. Interpolation is describing the process of how to assign individual weights to the observations at hand, when calculating the value at a new location P based on the original observations.

Prediction of gravity anomaly $\Delta \tilde{g}$ at P is a linear combination of the function values given at the data points Q_i, i.e.,

$$\Delta \tilde{g}_P = \sum_{i=1}^{I} \alpha_{Pi} \Delta g_i = \vec{\alpha}_{Pi} \cdot \Delta \vec{g}_i, \tag{3.5}$$

where α_i is the weight assigned to the different data points Q_i. When talking about selecting an interpolation method this means in particular to assign values to the α-coefficients following some criteria. In the following, a closer look will be taken on how these weights can be calculated in such a way that it leads to minimizing the average square error $\mathcal{M}\{\epsilon^2\}$.

3.1.3 The error-covariance function

As in any other field of study, estimate of a quantity should always be provided together with its correspond uncertainty. The whole purpose with interpolation is to estimate the target quantity's value at a locations that does not have any observation. To decide upon the best method, then a certain criteria needs to be defined, so the different methods can be compared.

The accuracy of any prediction method is described by the prediction error

$$\epsilon_P = \Delta g_P - \Delta \tilde{g}_P = \Delta g_P - \sum_i \alpha_{Pi} \Delta g_i \tag{3.6}$$

which is the deviation between the true Δg_P and the predicted value $\Delta \tilde{g}_P$. The best prediction method is the one which on average (average over the entire prediction area) yields the smallest prediction error m_P, i.e., the one which fulfills the condition

$$m_P^2 = M\{\epsilon^2\} = \min. \tag{3.7}$$

The value m_P is called the standard error of the prediction, so equation (3.7) is representing the square of this value. Inserting equation (3.6) into equation (3.7) and after some calculation the square of the standard error can finally be written as

$$m_P^2 = \mathcal{M}\{\epsilon^2\} = C_0 - 2\alpha_{Pi}C_{iP} + \alpha_{Pi}C_{ij}\alpha_{jP}.$$

For further explanation and derivation, I will refer to either Hofmann-Wellenhof and Moritz (2006); Gerlach and Ophaug (2021).

3.1.4 Least-squares prediction

So far, no numerical values have been assigned to the α-coefficients. In the previous section it was stated that the prediction should fulfill the condition given by equation (3.7). An optimization problem like this is solved by finding for which α-coefficients the derivative of m_P^2 is zero. Mathematically this is calculated by

$$\frac{\partial m_P^2}{\partial \alpha_{Pi}} = -2C_{Pi} + 2\alpha_{Pk}C_{ik} = 0,$$

and solving for α gives

$$\alpha_{Pk} = C_{ik}^{(-1)}C_{Pi}. \tag{3.8}$$

Now, as an expression for the α-coefficients which minimizes the square error have been found, then equation (3.8) can be inserted again in equation (3.5) giving

$$\Delta \tilde{g}_P = \alpha_{Pk}\Delta g_k = C_{ik}^{(-1)}C_{Pi}\Delta g_k. \tag{3.9}$$

Equation (3.9) expresses the predicted gravity anomaly $\Delta \hat{g}_P$ at a point P in terms of the covariance function C. The prediction based on equation (3.9) is known as *Least-Squares Prediction*(LSP), since the average prediction error is minimized. This prediction uses α-coefficients containing information on the signal characteristics through the covariance function.

3.1.5 Standard error of least-squares prediction

An expression for the gravity anomaly $\Delta \hat{g}_P$ in terms of the covariance function which guarantees to minimize the square error has been established through equation (3.9). The next step is to also express the square standard error m_P^2 by the covariance function C.

Inserting the α-coefficient which leads to minimum square error, i.e, the coefficients given by equation (3.8), into equation (3.7) gives an expression for the squared standard error in the prediction as

$$m_P^2 = C_0 - 2C_{ik}^{(-1)}C_{Pi}C_{Pk} + C_{ik}^{(-1)}C_{Pi}C_{jl}^{(-1)}C_{Pj}C_{kl}.$$

After some manipulation m_P^2 can be further simplified to its final form as

$$m_P^2 = C_0 - C_{ik}^{(-1)}C_{Pi}C_{Pk}. \tag{3.10}$$

3.2 Derivation of least-squares collocation

To keep track of the findings so far a short summary is necessary: With the help from statistical treatment a continuous representation of gravity anomalies Δg has been obtained using least-squares prediction given by equation (3.9), and the corresponding standard error can be calculated

from equation (3.10). Both equations depends on the knowledge of a covariance function $C(\psi)$, where a detailed description of both empirical and global covariance functions can be found in section 4. In this section, least-squares collocation will be derived from Stokes' equation based on the findings so far.

As was described in the introduction of section 3.1, the requirement for applying Stokes' equation is a continuous representation of gravity anomalies Δg. The findings from section 3.1 showed that gravity anomalies at arbitrary locations can be predicted using the least-squares prediction formula

$$\Delta \tilde{g}_P = \alpha_{Pk} \Delta g_k = C_{ik}^{-1} C_{Pi} \Delta g_k.$$

Through the least-squares prediction formula, a continuous representation of gravity anomalies is realized. From the above formula it is clear that in order to realize a least-squares prediction of gravity anomalies, the covariance between observation points and cross-covariance between observation points and computation points are needed. Inserting the continuous representation of gravity anomalies, given by the least squares prediction, into Stokes' formula gives

$$
\begin{aligned}
N_P &= \frac{R}{4\pi\gamma} \iint\limits_{\sigma} S(\psi_{PQ}) \Delta g_Q d\sigma_Q \\
&= \frac{R}{4\pi\gamma} \iint\limits_{\sigma} S(\psi_{PQ}) C_{Qi} C_{ij}^{-1} \Delta g_i d\sigma_Q.
\end{aligned}
\tag{3.11}
$$

The covariance matrix C_{ij} does not depend on the integration point Q, so it can be taken out of the integral resulting in

$$
N_P = \left[\frac{R}{4\pi\gamma} \iint\limits_{\sigma} S(\psi_{PQ}) C_{Qi} d\sigma_Q \right] \cdot C_{ij}^{-1} \Delta g_i.
\tag{3.12}
$$

Now a closer look on the terms within the brackets of equation (3.12) will be taken. An important component in Stokes' equation is the Stokes function $S(\psi_{PQ})$, which works as a weight for the different gravity anomalies Δg_Q. The Stokes function $S(\psi)$ is a one-dimensional function only depending on the spherical distance ψ between the calculation point P and the integration point Q, and it can be expressed through a harmonic expansion as

$$
S(\psi_{PQ}) = \sum_{n=2}^{\infty} \frac{2n+1}{n-1} P_n(\cos\psi_{PQ}),
\tag{3.13}
$$

where n denotes the spherical harmonic degree. The elements in C_{ij} can be described using the spherical harmonic expansion of the covariance function, i.e. from equation (4.1)

$$
C^{\Delta g}(\psi_{Pi}) = \sum_{n=2}^{\infty} c_n^{\Delta g} P_n(\cos\psi_{PQ}).
$$

Representing both the Stokes function and the covariance matrix by their spherical harmonic expansion, then the brackets of Stokes' equation can be written as

$$
\frac{R}{4\pi\gamma} \iint\limits_{\sigma} S(\psi_{PQ}) C_{Qi} d\sigma_Q = \frac{R}{4\pi\gamma} \iint\limits_{\sigma} \left[\sum_{n=2}^{\infty} \frac{2n+1}{n-1} P_n(\cos\psi_{PQ}) \right] \cdot \left[\sum_{p=2}^{\infty} c_p^{\Delta g} P_p(\cos\psi_{Qi}) \right] d\sigma_Q.
\tag{3.14}
$$

Through the *decomposition formula* a mathematical relationship between the Legendre polynomial and fully normalized spherical harmonics is established according to

$$P_n(\cos \psi_{PQ}) = \frac{1}{2n+1} \sum_{m=0}^{n} (\bar{R}_{nm}(P)\bar{R}_{nm}(Q) + \bar{S}_{nm}(P)\bar{S}_{nm}(Q)), \qquad (3.15)$$

where the fully normalized spherical harmonics $\bar{R}_{nm}$ and $\bar{S}_{nm}$ are evaluated at the calculation point P and the integration point Q. Inserting the newly formed expression for the Legendre polynomial, $P_n(\cos \psi_{PQ})$, gives an expression for the brackets as

$$\frac{R}{4\pi\gamma} \iint_{\sigma} S(\psi_{PQ}) C_{Qi} d\sigma_Q$$

$$= \frac{R}{4\pi\gamma} \iint_{\sigma} \left[\sum_{l=2}^{\infty} \frac{2l+1}{l-1} \cdot \frac{1}{2n+1} \sum_{m=0}^{l} (\bar{R}_{lm}(P)\bar{R}_{lm}(Q) + \bar{S}_{lm}(P)\bar{S}_{lm}(Q)) \right] \qquad (3.16)$$

$$\cdot \left[\sum_{p=2}^{\infty} c_p^{\Delta g} \cdot \sum_{m=0}^{n} (\bar{R}_{lm}(P)\bar{R}_{lm}(Q) + \bar{S}_{lm}(P)\bar{S}_{lm}(Q)) \right] d\sigma_Q.$$

By using the *orthogonality property* of fully normalized spherical harmonics, which states that only the integral of products between fully normalized spherical harmonics of same degree and order $n = p$ and $m = q$ will yield a value of n, and all other combinations will result in 0, then the following expression can be obtained

$$\frac{R}{4\pi\gamma} \iint_{\sigma} S(\psi_{PQ}) C_{Qi} d\sigma_Q = \frac{R}{\gamma} \sum_{n=2}^{\infty} \frac{1}{n-1} \cdot \frac{c_n^{\Delta g}}{2n+1} \cdot \sum_{m=0}^{n} \left[\bar{R}_{nm}(P)\bar{R}_{nm}(Q) + \bar{S}_{nm}(P)\bar{S}_{nm}(Q) \right].$$

$$(3.17)$$

Recognizing that the last part of equation (3.17) can be replaced with the Legendre polynomial, according to the *decomposition formula*, then equation (3.17) can be further simplified to

$$\frac{R}{4\pi\gamma} \iint_{\sigma} S(\psi_{PQ}) C_{Qi} d\sigma_Q = \frac{R}{\gamma} \sum_{n=2}^{\infty} \frac{1}{n-1} \cdot c_n^{\Delta g} P_n(\cos \psi_{Pi}). \qquad (3.18)$$

Explicitly writing the expression for gravity anomaly degree variances $c_n^{\Delta g}$, where the expression is given by the generalized formula for degree variances c_n^f in section 4, equation (4.6), alongside with the spectral eigenvalues λ_n^f and dimensioning factor D^f for gravity anomaly Δg found in table 2.1, then equation (3.18) can be further described by

$$\frac{R}{4\pi\gamma} \iint_{\sigma} S(\psi_{PQ}) C_{Qi} d\sigma_Q = \sum_{n=2}^{\infty} \frac{R}{\gamma} \frac{1}{n-1} \cdot \gamma^2 (n-1)^2 c_n P_n(\cos \psi_{Pi})$$

$$(3.19)$$

$$= \sum_{n=2}^{\infty} R \cdot \gamma (n-1) c_n P_n(\cos \psi_{Pi}).$$

Comparing the general formula for degree variances c_n^f and equation (3.19) a pattern can be found, showing that it contains the spectral eigenvalue and dimensioning factor of gravity anomaly and geoid height. Accordingly, equation (3.19) describes the cross-covariance between gravity anomaly and geoid height, and equation (3.19) can then be further reduced to

$$\frac{R}{4\pi\gamma} \iint_{\sigma} S(\psi_{PQ}) C_{Qi} d\sigma_Q = \sum_{n=2}^{\infty} R\gamma(n-1)c_n P_n(\cos\psi_{Pi}) = C^{N\Delta g}(\psi_{Pi}). \qquad (3.20)$$

A final equation for the brackets of Stokes' equation, as it was written in equation (3.12), can now be expressed in terms of the cross-covariance between gravity anomaly and geoid height. Inserting equation (3.20) into equation (3.12) gives

$$N_P = C_{Pi}^{N\Delta g}(C_{ij}^{\Delta g})^{-1}\Delta g_i. \qquad (3.21)$$

Equation (3.21) is known as *Least-Squares Collocation (LSC)*. Since all the derivations from equation (3.1) to equation (3.21) is only mathematical derivations, then both equations need to represent the same quantity. So, *Least-Squares Collocation* gives exactly the same solution as Stokes integration, but the major difference is that LSC does not require a continuous representation of gravity anomalies, only discrete point observations. Here I wish to emphasize on one important aspect and understanding of LSC. If it is possible to describe the covariance of the observed signal and its cross-covariance with the target quantity, then a prediction can be made according to equation (3.21).

3.3 Validation of estimates

The accuracy of a prediction result can be represented either using empirical or formal errors, and often a quantity in real life will be presented alongside with an estimate of its standard deviation $s = \hat{\sigma}$ or variance $s^2 = \hat{\sigma}^2$. For completeness, a description of both empirical and formal errors will be given in this section since both of them will be used in assessing the numerical results later in this thesis. The two error representations differ, one resulting solely from error propagation and mathematical relationship, while the other uses deviations between the predicted value at points which also contain independent measurement of the quantity.

3.3.1 Empirical errors

When new measurement systems and techniques are being developed, then a verification following a *closed-loop* simulation is often carried out. In a closed-loop simulation, both the input and output is known, i.e., values of the target quantity in the prediction area are known from independent measurements. In this way it is possible to compare different methods and processing strategies against each other with real observations. In this thesis, the implementation of LSC in MATLAB is validated in a near closed-loop simulation against an external dataset. The external dataset is a result of an estimation procedure using mainly the same datasets, and thereby the simulations is strictly a near closed-loop simulation, and not, exactly a closed-loop simulation. A closed-loop simulation can be created by leaving out a number of measurements when calculating the covariance functions. In this way an existing independent set of observations at P is available and can be used for validation. These observations are to be considered as ground truth.

The empirical error is defined as the difference between measured and predicted values at the points P. For the gravity anomaly the empirical error is given by

$$s_{emp} = \hat{\sigma}_{emp} = \Delta g_P - \Delta\tilde{g}_P. \qquad (3.22)$$

If several approaches exists for estimating $\tilde{\Delta g}_P$, then the approach resulting in smallest empirical error should be considered as the superior. As has been mentioned several times, calculating empirical errors requires independent observations at the prediction locations.

3.3.2 Formal errors

If a set of independent values at the prediction points is not available, then empirical errors can not be estimated as it requires available observations at the prediction points. Formal errors, in contrast to empirical errors, can always be calculated. These errors are calculated by the mathematical relationship between the measurements and the target quantities. Formal errors can be estimated using error-propagation, and in the case when predicting geoid heights N from gravity anomalies Δg the formal errors can be obtained from

$$\Sigma_P^N = C_P^N - C_{Pi}^{N\Delta g}(C_{ij}^{\Delta g})^{-1}C_{jP}^{N\Delta g}, \tag{3.23}$$

where Σ_P^N represents the error covariance matrix of all computation points P, C_{ij} the covariance matrix between all data points, and the cross-covariance matrix $C_{jP}^{N\Delta g}$ between data points and computation points. As can be seen from equation (3.23) the observations at Q are not necessary, and the corresponding covariance matrices can be calculated using methods which will be described in section 4.

Chapter 4

Covariance functions

Working on a global scale the covariance function for gravity anomaly $C^{\Delta g}(\psi)$ would conveniently be represented using a spherical harmonic representation. Global covariance functions play an important role as they describe the field's spatial variability. In section 3, covariance functions played a fundamental role in the derivation of LSC. They describe the stochastic relationship between the observations through the auto-covariance matrix, e.g, $C^{\Delta g}$, and also the statistical relationship between the observation and target quantity through the cross-covariance matrix, e.g., $C^{N\Delta g}$. One advantage with LSC is that it allows to use a mixture of different data types, such as geoid and gravity anomalies, when estimating the anomalous potential T. In addition, by LSC it is possible to estimate arbitrary gravity field functionals from inhomogeneous point observations (Moritz, 1980).

In this section the derivation of two different types of covariance functions will be given. From the potential coefficients of a GGM it is possible to derive global covariance functions, while local empirical covariance functions are estimated from observations within the study area. To adapt the global covariance functions to local conditions they are scaled with a factor based on the variance-ratio between the global and local covariance functions. A detailed explanation of the covariance modelling used in this thesis will first be given in section 5.1 after the theoretical foundation on the transition from residual geoid height ΔN to gravity anomalies Δg has been given.

4.1 Global covariance functions

Recalling the statistical properties of the anomalous gravity field itself, then already some conditions are imposed on the spherical harmonic expansion of $C^{\Delta g}(\psi)$. Knowing that the covariance function is defined to be an isotropic function, i.e. angular independency, then the spherical harmonic expansion cannot contain terms depending on azimuth. When expressing a global covariance function in terms of a spherical harmonic expansion, then zonal harmonics, i.e. those harmonics with an order of $m = 0$, are the only terms fulfilling this criteria. With an order of $m = 0$ all S_{nm} terms will vanish because $\sin(0 \cdot \lambda) = 0$, and a spherical harmonic representation for the global covariance function of gravity anomalies $C^{\Delta g}(\psi)$ will look like

$$C^{\Delta g}(\psi_{Pi}) = \sum_{n=2}^{\infty} c_n^{\Delta g} P_n(\cos \psi_{PQ}). \tag{4.1}$$

From equation (4.1) it can be seen that Legendre polynomials P_n are used instead of associated Legendre functions P_{nm}. The calculations of Legendre polynomials are implemented on computers by recursive algorithms due to better numerical stability than using Rodrigues' formula. On a computer, recursive algorithms are implemented for calculating the associated Numerically, recursive Covariance functions based on equation (4.1) uses potential coefficients from a GGM, and

they will therefore be called *global covariance functions*. An illustration of a covariance function is shown in figure 4.1, which shows that the covariance function decreases quite rapidly for larger distances. The correlation length ξ is defined as the distance where the covariance function has dropped to half of its maximum value, and it is often used for describing the signal's characteristic. A smooth signal will have a larger correlation length compared to a rough signal.
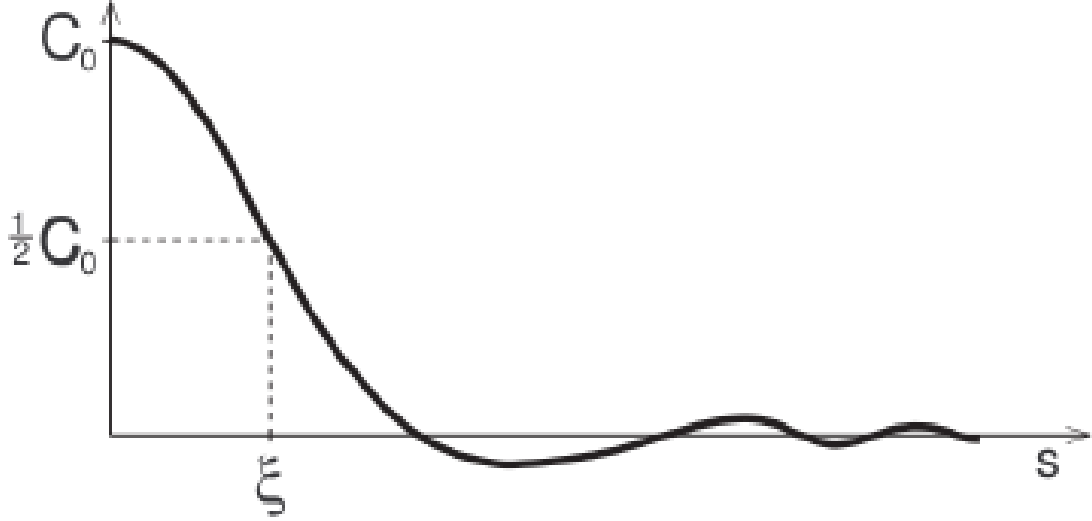
Figure 4.1: An illustration of a covariance function together with its descriptive parameters. C_0 - Signal variance and ξ - correlation length. The figure originates from Gerlach and Ophaug (2021).

To get a deeper understanding of global covariance functions a short derivation of the *degree variances* $c_l^{\Delta g}$ will be given in the following. The signal variance is defined as the global mean of the function under consideration, in the above case this was gravity anomaly Δg. Expressing the gravity anomaly Δg by its spherical harmonic expansion, equation (2.31), the signal variance can be written as

$$
\sigma^2(\Delta g) = \frac{1}{4\pi} \iint_\sigma \left[\frac{GM}{R^2} \sum_{n=2}^{\infty} (n-1) \sum_{m=0}^{n} (\Delta \bar{C}_{nm} \bar{R}_{nm} + \Delta \bar{S}_{nm} \bar{S}_{nm}) \right] \cdot \ldots
$$
$$
\ldots \left[\frac{GM}{R^2} \sum_{p=2}^{\infty} (p-1) \sum_{q=0}^{p} (\Delta \bar{C}_{pq} \bar{R}_{pq} + \Delta \bar{S}_{pq} \bar{S}_{pq}) \right],
$$
(4.2)

where spherical degree and order numbers are labelled $\{n, m\}$ in the first term of the product and $\{p, q\}$ in the second term. A detailed derivation will not be given in this thesis, for further details it is referred to Gerlach and Ophaug (2021); Hofmann-Wellenhof and Moritz (2006). By applying the *orthogonality relations of the spherical harmonics*, then equation (4.2) can be simplified to

$$
\sigma^2(\Delta g) = \left(\frac{GM}{R^2} \right)^2 \sum_{n=2}^{\infty} (n-1)^2 \sum_{m=0}^{n} (\Delta \bar{C}_{nm}^2 + \bar{S}_{nm}^2),
$$
(4.3)

where the spectral eigenvalue and dimensioning factor of gravity anomaly, see section 2.1, can be

recognized. Multiplying those two factors inside the summation signs and collecting terms gives

$$\sigma^2(\Delta g) = \sum_{n=2}^{\infty} \sum_{m=0}^{n} \left[\left(\frac{GM}{R^2}(n-1)\Delta\bar{C}_{nm} \right)^2 + \left(\frac{GM}{R^2}(n-1)\Delta\bar{S}_{nm} \right)^2 \right]$$

$$= \sum_{n=2}^{\infty} \underbrace{\sum_{m=0}^{n} \left[\left(\Delta\bar{C}_{nm}^{\Delta g} \right)^2 + (\Delta\bar{S}_{nm}^{\Delta g})^2 \right]}_{c_n^{\Delta g}}$$

$$= \sum_{n=2}^{\infty} c_n^{\Delta g}. \qquad (4.4)$$

Multiplying the spectral eigenvalue, dimensioning factor and the dimensionless potential coefficients gives the *degree variance* $c_l^{\Delta g}$. Equation (4.4) shows that the signal variance of gravity anomaly $\sigma^2(\Delta g)$ is calculated as the sum over all degree numbers l. Following this argumentation the individual terms represent the contribution of each degree l to the total variance. An alternative form of writing equation (4.4) would be to keep the spectral eigenvalue and the dimensioning factor outside of the summation over m, since they only depend on n. The degree variance can then be written as

$$c_n^{\Delta g} = \left(\frac{GM}{R^2}(n-1) \right)^2 \underbrace{\sum_{m=0}^{l} \left[\Delta\bar{C}_{nm}^2 + \Delta\bar{S}_{nm}^2 \right]}_{=c_n}, \qquad (4.5)$$

where the second term describes the dimensionless degree variances c_l.

From equation (4.5) a pattern can be seen, allowing for generalising the computation of degree variances for arbitrary functionals. Calculation of degree variance of an arbitrary gravity functional f can be written as

$$c_n^f = (\lambda_n^f)^2 \cdot c_n, \qquad (4.6)$$

and the total signal variance of an arbitrary gravity functional is then given by

$$\sigma^2(f) = \sum_{n=2}^{\infty} (\lambda_n^f)^2 \cdot c_n. \qquad (4.7)$$

When working with LSC the statistical relationship between different gravity functionals are needed, see for example equation (3.21) where the cross-covariance between geoid height N and gravity anomaly Δg is required. Already in 1974 closed expressions for covariance and cross-covariance for ΔN and Δg were derived by Tscherning and Rapp (Tscherning and Rapp, 1974):

$$C_{\Delta N_i \Delta g_P} = \frac{a}{\gamma_i} \sum_{n=2}^{N} c_n \frac{n-1}{r_P} \left(\frac{R_E^2}{r_i r_p} \right)^{n+1} P_n \cos\psi + \frac{1}{\gamma_i} \sum_{n=N+1}^{\infty} \frac{A}{(n-2)(n+b)} \frac{1}{r_P} \left(\frac{R_B^2}{r_i r_P} \right)^{n+1} P_n \cos\psi$$

$$(4.8)$$

and

$$C_{\Delta N_i \Delta N_i} = a \sum_{n=2}^{N} c_n \frac{1}{\gamma_i \gamma_j} \left(\frac{R_E^2}{r_i r_j} \right)^{n+1} P_n \cos \psi + \sum_{n=N+1}^{\infty} \frac{A}{(n-2)(n+b)} \frac{1}{\gamma_i \gamma_j} \left(\frac{R_B^2}{r_i r_j} \right)^{n+1} P_n \cos \psi,$$

(4.9)

where a: additional parameter r: geocentric radius of the point; γ: normal gravity on the ellipsoidal surface; R_E: the readius of the Earth; A: is a constant; b: is a constant and R_B is the radius of the Bjerhammer-sphere. All other quantities are defined as in the previous sections. The analytical closed expression derived by Tscherning and Rapp are used by Nguyen et al. (2020), where the parameters α, A and R_B are determined in a least-squares adjustment. Their study works in many ways as a guideline for the processing flow in this thesis. The procedure for selecting the best possible GGM within the study area was also treated in Nguyen et al. (2020). Gruber and Willberg (2019) give a full explanation on the assessment of a GGM in local areas based on comparison with GNSS-levelling and computation of geoid slopes. A more detailed explanation on selection of GGM can be found in section 2.2.

4.2   Scaling of the global covariance function

From the observation made so far it has become clear that a covariance function is only valid for the same gravity functional it was built for, and also for the area under consideration. This last fact becomes important when using a global covariance model. To verify that the global covariance function, derived using potential coefficients from a GGM, represents the signal characteristics for the area under consideration it should be compared with an empirical covariance function. If comparison of the global and empirical covariance function reveals differences, then the global covariance function can be scaled such that both functions gets the same variance. The scaling coefficient α can then be computed according to

$$\alpha = \frac{C_{0_{empirical}}}{C_{0_{global}}},$$

(4.10)

where $C_{0_{empirical}}$ and $C_{0_{global}}$ are the variance of the empirical and global functions, respectively. In case the empirical covariance function does not approach 0 with increasing distance, or it oscillates around a value different from 0, then some deterministic part is still present in the signal, and thereby it also violates with the signal properties stated in section 3. The handling of systematic and deterministic effects are more thoroughly discussed in section 5.1.5 and 6.

4.3   Empirical covariance function

In addition, to derive covariance functions using closed analytical expression, it is possible to derive empirical covariance functions *if* observations of the gravity functional are available in the area under consideration. A covariance function describes the statistical correlation of a function's value at two points Q_i and Q_j separated by a certain distance ψ_{ij}. The covariance is a statistical measure derived from the average of all point pairs within the same distance class. In order to do so, several distance classes needs to be defined, ideally following a specific rule. Defining different classes and average over all observations falling into each distance class will give a more robust result in a statistical sense, because the average value is based on a higher number of observations. From an intuitive understanding it is expected that the correlation of the two function values should approach 0 with increasing distance.

After an empirical covariance function has been calculated, then it would be preferable to fit an analytical function that resembles this empirical function well in order to determine covariance

values for arbitrary distances. There exists several different analytical functions for this purpose, and among them are exponential functions, Hirvonen's model or Tscherning/Rapp as given by equation (4.9) and equation (4.8). In this thesis, the empirical covariance function will only be used as a comparison and scaling for the global covariance function.

4.3.1   How to define distance classes

A question when deriving an empirical covariance function is how to select distance classes. Several attempts have been made in order to find a clever way, but none of these approaches has proven to be superior to any of the other methods. One obvious thing is that all distance classes should contain a similar amount of observations, otherwise the mean value for each class will not be determined with the same accuracy, as this is dependent of the number of observations. If the last class, containing those point pairs separated furthest from each other, cannot be filled up, then these points will be disregarded when forming the empirical covariance function. This is done in order to keep a simple and efficient implementation in MATLAB allowing for working with matrices. The relative distribution, not shown here, of point pairs has a maximum for smaller distance, so the potential effect of leaving out those point pairs separated furthest from each other can be neglected. On the other hand the distance distribution between point pairs is not evenly distributed, and then by fixing a number of observations in each class will cause that some classes may cover a large distance span. No matter how the distance classes are defined it will have this side-effect. Quantifying the possible effect on the procedure of selecting distances classes has not been possible within this thesis. In order to do so, a closer inspection of the distance distribution for all point-pairs has to be made, but this goes beyond the scope of this thesis.

4.3.2   Calculation of spherical distances

It is by now well established that a one dimensional covariance function depending only on the spherical distance $C(\psi)$ shall be used for describing the function's behaviour. In all the derivations the distance variable has been denoted with ψ, instead of its planar relative s. From the fact that LSC will be implemented on a fairly large area, with a dimension of $2° \times 2°$, it is necessary to use spherical distance, instead of planar distance. The spherical distance between two points $P(\phi_P, \lambda_P)$ and $Q(\phi_Q, \lambda_Q)$ can be calculated using

$$\cos \psi_{PQ} = \sin \phi_P \phi_Q + \cos \phi_P \cos_Q \cos(\lambda_P - \lambda_Q). \tag{4.11}$$

When implemented on computers with low float precision a spherical distance calculated by equation (4.11) can cause large rounding errors for short distances. Haversine's equation given by

$$\sin^2\left(\frac{\phi_{PQ}}{2}\right) = \sin^2\left(\frac{\phi_P - \phi_Q}{2}\right) + \sin^2\left(\frac{\lambda_P - \lambda_Q}{2}\right) \cos \phi_P \cos \phi_Q \tag{4.12}$$

is better conditioned for small distances and has been implemented in MATLAB.

Chapter 5

Satellite altimetry

Altimetry satellites are active sensors providing measurements of the Earth's surface height using radar techniques. Satellite altimetry are used in observing the Earth's water bodies, and among the parameters they can determine are time-varying sea-surface height (ocean topography), coverage of ice sheets, significant wave heights and determine wind speeds (ESA, 2020c). With increased focus on climate change the by far most used application of satellite altimetry is the monitoring of sea surface changes. As described in section 1, satellite altimetry is an essential part of the 6 main services of the Copernicus programme coordinated by ESA. At 21. November 2020, Sentinel-6 Michael Freilich was launched as the next satellite altimetry mission following its predecessor Sentinel-3, and a second satellite Sentinel-6B is planned for launch in 2025. Sentinel-6 is the first satellite within the Sentinel family that carries a dual-system satellite navigation receiver capable of receiving both GPS and Galileo signals to perform Precise Orbit Determination (POD). Initial test shows that position accuracy is improved by a factor of two compared with GPS-only measurements (ESA, 2020d). Sentinel-6, alongside with CryoSat-2 and Sentinel-3A, is part of the new-generation altimetry satellites which uses the synthetic aperture radar (SAR) technique. Compared to conventional altimetry satellites, the SAR technique achieves greater precision and a spatial resolution of 300 m in high-resolution mode compared to previous mission with a spatial resolution of several kilometres. The better spatial resolution will allow retrieval of sea-surface measurements closer to the coastline, which is an important aspect in sea surface analysis (ESA, 2020a). An in-orbit validation with Jason-3, successfully completed at 27. January 2021, assures that no biases are introduced into the time series of data. For the next 12 months, Sentinel-6 will orbit closely following Jason-3 before starting operating as the operational reference mission (ESA, 2021). Sentinel-6 will continue the legacy of sea-surface height measurements that began with Topex-Poseidon in 1992 until at least 2030 (ESA, 2021). An overview of recent and current satellite altimetry missions can be found in figure 1.2.

Satellite altimetry missions can be divided into two main categories based on their scientific goals: Exact repeat mission (ERP) and Geodetic mission (GM). These two mission types differ from each other with respect to spatial and temporal resolution. GMs provides data with a high spatial resolution, and hence also a long repetition period. Earth's gravity field is of special interest in geodesy, and the gravity field can be split into a static and temporal part. Due to a long repetition period, then GM altimetry missions can only observe long wavelength components of the Earth's gravity field. ERPs have a coarser spatial resolution, but on the other hand a short repetition period. To observe location dependent small scale changes, often characterised with high temporal variations, frequent observations at the same location on ground is a requirement. In observing temporal changes of climate related quantities, such as sea surface height, ERP satellite missions are of great importance. It is not possible to create an orbit with both high spatial resolution and temporal resolution at once, so there is a constant trade-off between orbital height and revolution period. The mathematical connection between the two will be given in the following. Here it will also be shown that orbital errors propagate directly into an estimate of sea surface height. Satellites flying in a higher orbit will be less affected by orbit perturbations, but the signal strength will reduce. Satellite altimetry measures the Earth's gravity field at ground level, but it is still a
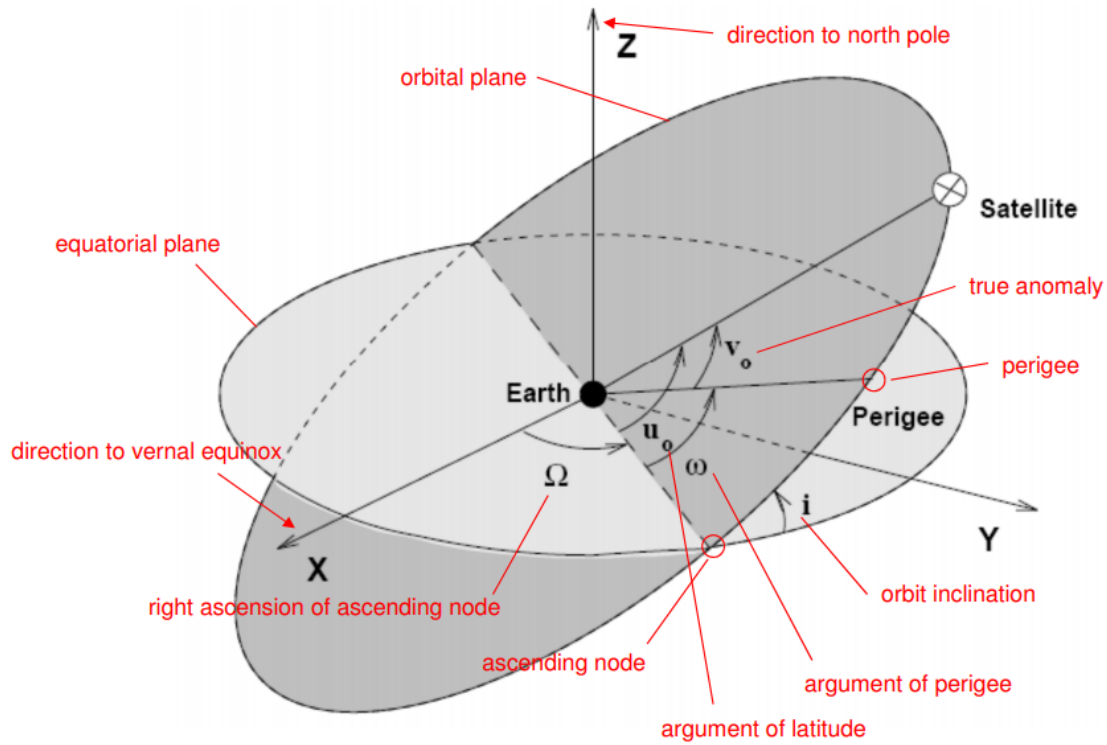
Figure 5.1: A representation of the different Keplerian elements needed for describing a satellite orbit in space. The figure originates from lecture notes on satellite geodesy given at the Technische Universität München.

reduction in signal strength due to backscattering and atmospheric effects.

Before a detailed description of satellite altimetry and its observation equation will be given, a short introduction to satellite orbits is appropriate. Orbital parameters are selected based on the mission's scientific goal, and a satellite orbit can be fully described by six orbital elements, also known as as Keplerian[1] elements. Figure 5.1 shows the six Keplerian elements needed to describe a satellites position in space. Semi-major axis a and the numerical eccentricity e describes the orbit's shape, while the inclination i and right ascension Ω of the ascending node describes the orbital plane's orientation. The satellite's position along this plane can be described using argument of perigee ω and the perigee passing time T_0, or alternatively the argument of latitude u_0 at an epoch t_0, i.e., the angle between the ascending node and the satellite position at the epoch t_0, measured in the direction of the motion of the satellite.

As already mentioned, satellite altimetry missions can be divided into two categories, where the different types are characterised by its spatial and temporal resolutions. The revolution period T_{rev} of a satellite orbit describes the time a satellite uses on one full revolution around the Earth. From Kepler's 3rd law the revolution period can be derived from

$$n^2 a^3 = GM,$$

where n is the mean motion and a is the satellite orbit's semi-major axis. Mean motion describes the satellite's angular velocity by

$$n = \frac{2\pi}{T},$$

[1]Named after the German mathematician and astronomer Johannes Kepler(1571-1630).

and writing n explicitly in Kepler's 3rd law gives a revolution period T_{rev} of

$$T_{rev} \approx 2\pi \sqrt{\frac{a^3}{GM}}.$$

A mission's temporal resolution is represented by the repetition period T_{rep}, and it describes how long time it takes before the satellite repeats its ground track. To repeat the exact same ground track, then the total number of Earth revolutions α, relative to the satellite orbit must be equal to the Earth's relative angular velocity relative to the satellite orbit $(\omega_e - \dot{\Omega})$ multiplied with the repetition period P_{orb}. During this time the Earth has rotated an angle of $2\pi\alpha$. The repetition period P_{orb} can then be described by

$$2\pi\alpha = P_{orb}(\omega_e - \dot{\Omega}) \Rightarrow P_{orb} = \frac{2\pi\alpha}{\omega_e - \dot{\Omega}}, \tag{5.1}$$

where ω_e is the Earth's angular velocity and $\dot{\Omega}$ is the drift in right ascension of the ascending node. The spacing between satellite ground tracks on the Earth's surface defines a mission's spatial resolution. To calculate the spatial resolution it is necessary to know the total number of revolutions β performed by the satellite within one repetition period P_{orb}. From Kepler's 3rd law the satellite's revolution period T_{rev} is known, and then the total number of revolutions β can be calculated from

$$\beta = \frac{T_{rev}}{P_{orb}}. \tag{5.2}$$

The angular spacing between satellite ground tracks can then be calculated by

$$\Delta\lambda = \frac{2\pi}{\beta}, \tag{5.3}$$

or alternatively expressed in km by

$$\Delta x = \frac{222.4\pi}{\beta} \cos\phi. \tag{5.4}$$

From equation (5.4) it is seen that the spatial resolution is dependent of latitude with largest spread in ground tracks for small latitude values. An orbit's inclination i, defines the accessible areas for the satellite $\mid \phi_{max} \mid = i$, or for a retrograde orbit, i.e. a orbit with an inclination angle larger than 90°, $\mid \phi_{max} \mid = 180° - i$. Typical spatial and temporal resolution are shown in table 5.1 for recent and current satellite altimetry missions.

5.0.1   From observations by satellite altimetry to gravity anomalies

As previous described in section 3, the geoid height N at a computation point P can be calculated from gravity anomalies Δg_Q using Stokes's formula given by 3.1. From the derivation in section 3, Stokes's formula was used to derive an expression for estimating geoid height N with LSC and also showing that the two methods are mathematical equivalent. Stokes's formula represents the functional relationship $\Delta g \rightarrow N$. When estimating gravity anomalies from reidual geoid height the relationship $\Delta N \rightarrow \Delta g$ is needed. A final expression for representing this relationship was

derived for LSC in equation (3.21). However, LSC is not the only possible technique that can be used for predicting gravity anomalies Δg from residual geoid heights ΔN. Even though none of these approaches are used in this thesis, they should be mentioned as they are commonly used in gravity field modelling.

The integral equation representing the relationship $\Delta N \rightarrow \Delta g$ is given by the inverse Stokes equation, also known as Molodensky's equation (Andersen, 2013)

$$\Delta g_p = \gamma \frac{N_p}{r} - \frac{\gamma}{16\pi r} \iint\limits_{\sigma} \frac{N - N_p}{\sin^3(\psi/2)} d\sigma, \tag{5.5}$$

where ψ describes the spherical distance between the integration point $P(\lambda_P, \phi_P)$ and the integration point $P(\lambda, \phi)$. All other quantities are defined in the other equation shown within this thesis.

Another option is to calculate gravity anomalies by observing north/south and east/west deflections of the vertical (ξ, η), and then calculate gravity anomaly Δg and geoid height H from the inverse Vening Meinesz[2] equation and the deflection geoid formula (Andersen, 2013)

$$\begin{Bmatrix} N \\ \Delta g \end{Bmatrix} = \frac{1}{4\pi} \begin{Bmatrix} R \\ \gamma \end{Bmatrix} \iint\limits_{\sigma} (\xi \cos \alpha + \eta \sin \alpha) \begin{Bmatrix} C \\ H \end{Bmatrix}, \tag{5.6}$$

where the kernel functions H and C represent the connection between the observables and the corresponding target quantities, for gravity anomaly

$$H(\psi) = \frac{\cos(\psi/2)}{2\sin(\psi/2)} \left(-\frac{1}{\sin(\psi/2)} + \frac{3 + 2\sin(\psi/2)}{1 + \sin/\psi/2)} \right), \tag{5.7}$$

while for geoid height the kernel function is given by

$$C(\psi) = -\cot \frac{\psi}{2} + \frac{3}{2} \sin \psi. \tag{5.8}$$

---

[2]Named after the Dutch geodesist Felix Andries Vening Meinesz (1887-1966)

Table 5.1: An overview of historical and present satellite altimetry missions and some of their respective orbital parameters. Mission details have been collected from Breili (2018) and at the missions respective operation websites.

Mission	Mission era	Orbital height	Inclination	Revolution period	Repetition period	Distance equator
SKYLAB	1973	435 km	50°	93.4 min		
GEOS-3	1975-1978	845 km	115°	102 min		
SeaSat	1978-1978	800 km	115°	100 min		
GeoSat	1980-1980	800 km	108°	100 min	3, 17 d	163 km
GFO-1	1998-2008	800 km	108°	100 min	17 d	
ERS-1	1991-1996	785 km	98.5°	112 min	3,35,168 d	77 km
ERS-2	1995-2000	785 km	98.5°	112 min	35 d	77 km
ENVISAT	2002-2012	785 km	98.5°	112 min	35 d	77 km
TOPEX/POSEIDON	1992-2005	1336 km	66°	112 min	35 d	315 km
Jason-1	2001-2013	1336 km	66°	112 min	10 d	315 km
Jason-2	2008-2019	1336 km	66°	112 min	10 d	315 km
IceSat	2003-2010	600 km	94°	97 min	91 d	
CryoSat-2	2010 →	717 km	92°	100 min	309/30 d	
Saral/Altika	2013 →	815 km	98.55°	100 min	35 d	
Jason-3	2016 →	1336 km	66°	112 min	10 d	315 km
Sentinel-3a	2016 →	815 km	98.65°	100 min	27 d	104 km
Sentinel-3b	2018 →	815 km	98.65°	100 min	27 d	52 km
Sentinel-3c	2023?	810 km	98.65°	100 min	27 d	52 km
Sentinel-3d	2025?	815 km	98.65°	100 min	27 d	
IceSat-2	2018 →	496 km	94°	100 min	91 d	315 km
Sentinel-6	2020 →	1336 km	66°	112 min	10 d	315 km
SWOT	2022?	891 km	77.6°	100 min	21 d	

In this thesis, only least-squares collocation will be used to predict gravity anomalies from residual geoid heights. The satellite altimetry observation equation and its different components will be described in the following sections. In addition, an adaptation of the LSC expression, derived in section 3, to represent the stochastic relationship between residual geoid height ΔN and gravity anomalies Δg will be presented. As the procedure of deriving a residual geoid height signal involves several different components and models, a summary of the reference systems and tide systems used in the this thesis will be presented. By not assuring consistency in reference systems between all datasets will introduce unwanted systematic errors into the signal. The final part in this section focuses on the application and modelling of covariance functions. Extended literature on satellite altimetry and its application on marine gravity field modelling can be found in Andersen (2013); Stammer and Cazenave (2017).

5.1   Satellite altimetry observations

Altimetry observations are well suited in open waters, where the observation area is uniform and without distortions. When approaching shore the observations becomes noisy, or they get a totally different form than expected for open-water areas. How land affects the signal is called *land contamination*. One of the main sources for this effect is that the footprint contains backscattered signal from land areas. The correction terms for the altimetry observation have a lower spatial resolution, and therefore they will be contaminated earlier by land than the altimetry observations itself. In addition, geophysical corrections becomes more challenging in coastal areas. An overview of the error budget for Jason-2 is shown in table 5.2, where the table originally was published in Stammer and Cazenave (2017). The new satellite altimetry mission Sentinel-6 reports an even better orbital determination than what is reported for Jason-2. Anyhow, table 5.2 provides an overview in error budget for a modern satellite altimetry mission. Benveniste et al. (2020) reports that wet tropospheric corrections becomes inaccurate at distances shorter than 20-50 km from land caused by land reflection entering into the radiometer footprint, while the models for sea state bias (SSB), which accounts for the interference between radar pulse and sea surface, becomes inaccurate within 10-15 km from the coast. Another component that affects the return pulse is how it is reflected by the sea surface. In wind-still conditions without waves the pulse will appear as a spike, because the sea surface acts like a mirror(Breili, 2018). Coastal regions on the other hand are often characterised with surface currents and short wavelength characteristics which disturbs
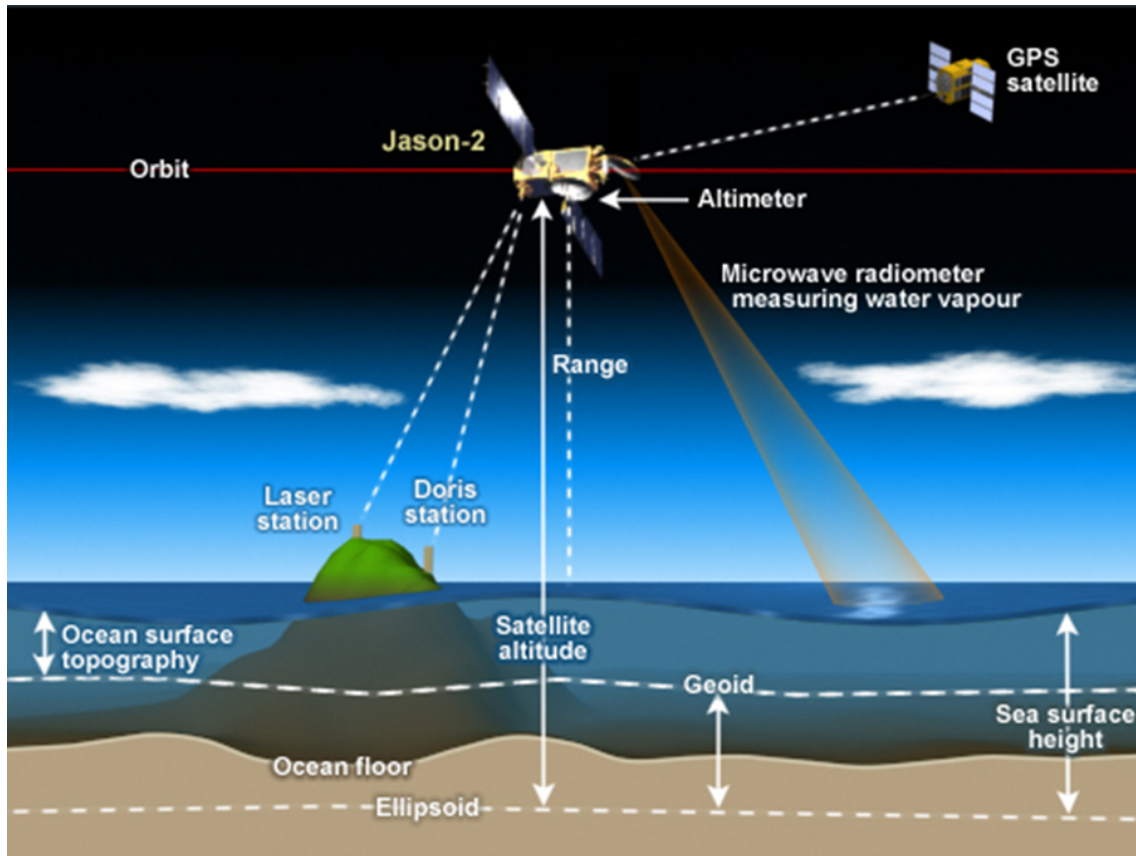
Figure 5.2: Representation of the key components in satellite altimetry. An altimetry satellite's position is determined using DORIS, SLR and GNSS, and then the altimetry observe the relative distance between itself and the sea surface. Notice that the sea surface can be decomposed into different quantities. The figure originates from NOOA (2021).

the backscattering effect.

In contrast to other specially designed gravity missions, such as CHAMP, GRACE, GOCE and GRACE-FO, altimetry provides observations at the the Earth's surface by its measurement of *sea surface height* (SSH). Altimetry observations alongside with terrestrial measurements gives the full signal of the Earth's gravity field, but altimetry also provides global coverage, and hence is a measurement technique with great potential in marine gravity field modelling. Satellite altimetry observes SSH with respect to its own position. This is an important property of satellite altimetry and caution needs to be made in processing to assure consistency in reference systems between the different model components. A new satellite altimetry mission always goes through an in-orbit validation phase to assure that no biases relating to the observation equipments are introduced with respect to previous missions.

The measurement principle for satellite altimetry is that the satellite transmits and records its own pulse, then the distance R between the satellite and the reflecting object in presence of no error-sources is given by

$$R = \frac{c\Delta t}{2},$$
(5.9)

where $c = 299\,792\,458\,\mathrm{m\,s^{-1}}$ is speed of light in vacuum and Δt is the time between transmittance and recording. Equation (5.9) expresses a relative distance measurement with respect to the transmitting satellite.

Figure 5.2 shows the different components involved in satellite altimetry with both the measurement

principle in satellite altimetry, but also the POD using space geodetic techniques such as SLR, DORIS and GNSS. The position of an altimetry satellite is then referring to the same reference ellipsoid as is used for the control stations and GNSS satellites in the POD. Satellite altimetry is by these means a geometrical measurement technique, however, the target quantity SSH is governed by physical laws. By knowing the satellite height H, then SSH can be represented in the same reference frame by

$$h_{SSH} = H - R. \tag{5.10}$$

From equation (5.10) it is clear that an error in satellite position, which will effect the H component, will propagate directly into the estimation of SSH. Because of this fact, POD of altimetry satellites is very important. Today altimetry satellites are determined with an accuracy of 1-2 cm (Breili, 2018). Additional corrections needs to be made as well, due to signal propagation in the atmosphere and signal interaction with the sea surface. These corrections are summarised in table 5.2.

Equation (5.10) is dependent of time through the distance measurement in equation (5.9). The pulse generated by an altimetry satellite creates a *footprint* covering a certain area on the Earth's surface. Sentinel-6, the newest altimetry satellite, has a footprint of 300m resulting from its improved SAR-technique, and a list of different altimetry satellite mission and their specifications are given in table 5.1.

Table 5.2: An overview of the error budget for Jason-2 sea surface height measurement. Notice that the table shows uncertainty in the correction term of the error source, and not the magnitude of the correction itself. The table is adapted from Stammer and Cazenave (2017).

Parameters		Altimetry Uncertainties [cm]
Parameters and correction for sea surface height	Altimeter range	1.7
	Filtered-out altimeter ionosphere correction	0.2
	Sea state bias	0.2
	Dry troposphere and dynamical atmospheric corrections	0.7
	Radiometer wet troposphere	0.2
	Ocean tide	1.0
	Orbit (radial component)	1.5
Sea surface height	Corrected with all corrections	<3.5

If the signal would have been reflected by a planar surface, then time of flight Δt could easily been determined. The reflecting signal would only consist of one sharp return pulse(echo). Irregularities in the sea surface will cause multiple echoes and decision of Δt becomes more complex. From the received echo's shape, information about sea surface height, significant wave height and wind speed can be derived (Ophaug et al., 2019). As can be seen from figure 5.2, the physical measurement quantity SSH is composed of several different components. Different applications and quantities are possible depending on the field of interest. In this thesis, the *geoid* is of particular interest. Table [ref], found in (Breili, 2018), shows the different applications area for satellite altimetry. As this thesis focuses on determination of gravity anomalies Δg from residual geoid heights ΔN, no further focus will be paid to topics involving preprocessing of altimetry observations. Now a closer look at the observation equation will be made, and in particular to decompose the sea surface height measurement into different components. An excellent illustration of the different processing steps can be found in Nguyen et al. (2020). The processing flow, implementation and processing used in this thesis can be found in figure 6.1 which is greatly inspired from the scheme found in (Nguyen et al., 2020).

5.1.1 Altimetric observation equation

The observation equation is a bit more complicated than equation (5.10) implies and is described through

$$h_{SSH} = N + \zeta + \epsilon, \tag{5.11}$$

where N is geoid height above the reference ellipsoid, ζ contains time-variable sea surface topography, and ϵ is the error including: instrumental corrections; sea state bias corrections; ionospheric correction; tropospheric correction(wet, dry); tides (ocean, earth, pole); inverse barometer (Nguyen et al., 2020). Application of satellite altimetry observations depends on which component in equation (5.11) that is of interest. In geodesy, which is the focus of this thesis, N is of particular interest, while in ocean studies ζ is the important component.

Both geoid height and sea surface topography can be split up into two parts containing long and short wavelength components. Geoid height can be written as $N = N_{GPM} + \Delta N$, where a GGM is used for describing the long wavelength part N_{GPM} and ΔN is the residual signal. Sea surface topography can be written as $\zeta = \zeta_{MDT} + \zeta(t)$, where ζ_{MDT} is *mean dynamic topography* (MDT) and $\zeta(t)$ is *time varying sea surface topography* also known as *dynamic ocean topography* (DOT). Explicitly writing out N and ζ in equation (5.11) gives

$$h_{SSH} = N_{GGM} + \Delta N + \zeta_{MDT} + \zeta(t) + \epsilon. \tag{5.12}$$

Equation (5.12) is the fundamental observation equation in satellite altimetry. This thesis focuses on how satellite altimetry can be used in marine gravity modelling, and hence the target quantity is the residual geoid height signal ΔN. In order to estimate ΔN with a given accuracy, then all other terms in equation (5.12) needs to be estimated within the same accuracy. Equation (5.12) still contains time-variable components not relating to the geoid component, and a way to reduce these effects is needed. There are two methods that can be used, either model the time-varying or create differences to reduce its value. Forming difference between two neighbouring points i and j, while assuming that N_{GPM}, ζ_{MDT} and $\epsilon(t)$ have long wavelength characteristics, gives

$$h_i - h_j \approx \Delta N_i - \Delta N_j + \epsilon \approx \partial N + \epsilon \tag{5.13}$$

and all terms with long wavelength behaviour will cancel out, since they are assumed to have the same value in both points. Equation (5.13) describes the geoid slope which is closely related to the deflection of the vertical in the north and east direction (ξ, η) which can be used to derive gravity anomalies Δg (Andersen, 2013), recall the inverse Vening Meinesz equation given in equation (5.6) as part of the introduction in section 5. The assumptions made when deriving equation (5.13) will not necessarily be true in shallow areas where effect of wind and currents have a higher spatial variation. An alternative approach would be to model those terms instead. This will be a very complex task, in particular for the time varying sea surface topography which contains high frequency components caused by wind and other effects. The geometrical shape of a satellite orbit causes different spacing of ground tracks depending on latitude, as it was described in the introduction of 5. Ground tracks are separated by a larger distance for low latitudes, while having more dense tracks for regions in high latitude. This leads to a more accurate estimation of geoid undulation in north-south direction for low latitudes, and better accuracy in east-west direction for high latitudes (Andersen, 2013). In this thesis, datasets containing *mean sea surface* (MSS), DTU18MSS (Andersen et al., 2018) and DTU13MSS (Andersen et al., 2016), are given. As the name describes, it is a mean of SSH extended over a long period of time. Effects due to tides and atmosphere have been corrected prior to the mean calculation

$$h_{MSS} = N + \zeta_{MDT} + e = N_{GPM} + \Delta N + \zeta_{MDT} + e. \tag{5.14}$$

Equation (5.14) does not contain the time varying sea surface topography $\zeta(t)$ because it is expected to be a stochastic signal, which implies an expected value of $E(\zeta(t)) = 0$, and with time-averaging all stochastic and time dependent quantities will cancel each other out. $\zeta(t)$ will vary most in regions with largest differences, such as within the large ocean systems, and has a wavelength of 100-200 km mainly caused by wind, waves and air pressure (Andersen, 2013). Equation (5.14) forms the final observations equation used in this thesis, and in the following a description of its different terms will be given.

5.1.2   Mean dynamic topography(MDT)

In Nguyen et al. (2020) mean dynamic topography (h_{MDT}) is defined as the average value of the difference between mean sea surface (h_{MSS}) and geoid height (N_{GGM}) over many years:

$$h_{MDT} = h_{MSS} - N_{GGM}. \tag{5.15}$$

In this thesis, DTU13MDT is used as the mean dynamic topography model, and a detailed description on the development of DTU13MDT can be found in Andersen et al. (2016). As a short summary, the calculation of DTU13MDT is performed in a purely geodetic way, where the difference between DTU13MSS and quasi-geoid heights, derived according to equation (2.23), from EIGEN-6C3 (Foerste et al., 2011) was used to estimate the MDT according to equation (5.15). In turn the calculation of EGIEN-6C3 uses surface data based on EGM2008. So, even if another GGM is used as part of the RCR-method, a dependency on EGM2008 exist due to the calculation procedure in DTU13MDT. Still, as was described in section 2.2, the RCR-method should in principle be model independent given that the GGM fits reasonably well with local conditions. Andersen et al. (2016) shows that the largest difficulty in creating a MDT is that the MSS and GGM resolves different signal scales. The spherical harmonic expansion describing the Earth's gravity field is only expanded to a maximum degree and order N_{max}, where the spatial resolution possible to resolve with a given maximum degree can be calculated from equation (2.27). Normally the spatial resolution of a GGM and MSS differ which induces small scale signals in the MDT originating from the Earth's gravity field signal above the GGM's maximum degree. In order to obtain an useful estimate of the MDT without these small scale signals, a proper filtering of the MDT is necessary. The application of a MDT is in the field of oceanographic studies where horizontal derivative of the MDT, and assuming geostrophic conditions, can be used to derive surface geostrophic currents (Breili, 2018). A recent study by Wu et al. (2020) indicates that selection of GGM is of great importance in oceanographic research when forming geostrophic currents from MDT surfaces. Their results for the South China Sea by comparison of geostrophic currents from different GGMs with currents derived from oceanographic models shows an increased accuracy of the more recent developed GGMs with a higher number of observations and improvements in processing strategies.

5.1.3   Time varying sea surface topography(DOT)

Alongside with the treatment of $\zeta(t)$, Andersen (2013) points out an important processing issue with MSS. A MSS will only be possible to realize in points with several measurements. In section 5, it was described that altimetry satellites can be divided into two categories: GM and ERM. Several observations in a point is only true if the point lies along the ground track of ERM satellites. If no interpolation is applied, then the MSS will for points between the ground track of an ERM be realised based only on the observations from a GM. Altimetric observations are available as discrete observations both geographical and in time. If continuous observations in a point would have been available, then mean of the *time varying sea surface topography* $\zeta(t)$ would have become 0. Due to discrete sampling of altimetry observations, a MSS will contain a time-varying component $\zeta(t)$. Crossover adjustment between different altimetry missions is used to minimize $\zeta(t)$. Assuming that a point's residual geoid height signal should be time invariant, then intersecting satellite ground tracks can be used for cross adjustment to eliminate, or at least reduce, the time varying sea surface

topography. A short summary of the procedure is that it minimizes the height difference between measurements from different satellite revolutions or missions. This step represents a removement of offset between different observation epochs, making all observations referring to the same reference point. Crossover adjustement is a topic of preprocessing so no further discussion on this matter will be done, further details can be found in (Andersen, 2013; Stammer and Cazenave, 2017).

5.1.4   RCR-method revisited

In section 2.2.1, the concept of the RCR-method was introduced. As now finally all components involved in satellite altimetry have been introduced, the observation equation used for predicting gravity anomalies by LSC can be presented.

In the same way as for the long wavelength part of the Earth's gravity field, global models of MSS and MDT can be used to reduce their respective quantities' long wavelength components. After all reductions have been done a residual geoid height ΔN is given by

$$\Delta N = h_{MSS} - N_{GGM} - h_{MDT}. \tag{5.16}$$

Equation (5.16) is the observable to be used for predicting gravity anomalies by LSC.

5.1.5   Reference systems and tide systems

All geodetic products that are provided relates to a specific reference system and tide system. As has been described in section 5, satellite altimetry products are referring to the same reference system as the satellite's position is referring to. In addition to reference system, the products are also defined in a given tide system. The three tide systems differ from each other depending on which effects caused by the Sun and Moon that are corrected for. The tidal effects consist both of a time dependent and time independent components, where the time dependent component has a periodic behaviour and with observation over time its mean value will be zero (Ophaug, 2018). The time independent component is the tidal effects permanent deformation of the Earth's surface. These effects have a mean value different from zero, and they will therefore not cancel over time, and then they have to be corrected for. From (Ophaug, 2018) and the ICGEM faq website (ICGEM, 2019) the different tide systems are defined as:

- In a *tide-free* system all (direct and indirect) effects of the Sun and Moon are removed.

- In a *mean-tide* system no permanent tidal effects are removed, so it includes the presence of the Sun and Moon.

- In a zero-tide system all permanent effects of the Sun and Moon are removed, but the indirect effects component related to the elastic deformation of the Earth is retained.

The orbital planes of the Sun and the Moon are close to the equatorial plane, so the tidal effect is mainly latitude dependent. The requirement for applying LSC is that the signal behaves stochastically, which means that no deterministic signal or inconsistency in the parameters and definitions of the GGM, MSS or MDT can exist. As a preprocessing step, the potential inconsistency in reference systems and tide systems must be corrected for. DTU13MSS and DTU13MDT had previously been transformed from TOPEX to WGS84 reference ellipsoid, while The DTU18MSS dataset is accordingly referring to a TOPEX reference ellipsoid, while DTU13MSS refer to WGS84. Along the Norwegian coastal zone the difference between WGS84 and TOPEX has a mean value of $\epsilon_{corr} = 0.71$ m. The residual geoid height ΔN in RLSC will then be calculated according to

$$\Delta N = h_{MSS} - N_{GGM} - h_{DTU18MDT} + \epsilon_{corr}, \tag{5.17}$$

where the ellipsoidal correction is $\epsilon_{corr} = 0.71\,\mathrm{m}$ and $\epsilon_{corr} = 0\,\mathrm{m}$ for DTU18MSS and DTU13MSS, respectively.

The corrected field follows the stochastic requirements in chapter 3. Even though a GGM is applied for removing the field's long wavelength components, the residual geoid height ΔN is further reduced by its own mean value. This is done in order to remove any possible systematic effects relating to the GGM, and it will also assure consistency and allow for comparison of gravity anomalies predicted by RLSC using different GGMs for the remove-restore step. If an inconsistency in reference systems, tide systems or other definitions would have been present, then a reduction with the residual signal's mean value would reduce its effect significantly. On the other hand, reducing the residual signal by its mean value can then also cover systematic effects, so thorough investigation of the datasets is always required.

5.1.6 Prediction of gravity anomalies using least-squares collocation

Equation (5.16) is the observation equation entering into the least-squares collocation approach for predicting gravity anomalies. The calculation procedure is shown as a flowchart in figure 6.1.

In section 3, an expression for the geoid height in a computation point P was derived from Stokes' formula. It was shown that least-squares collocation and integral representation of geoid height N by Stokes' formula would mathematically give the same results. Section 3 used collocation to estimate geoid height N from gravity anomalies Δg, but as was shortly explained in the introduction of section 5, and also can be seen in equation (5.16), satellite altimetry provides observation of residual geoid height ΔN.

It was described in section 3 that LSC is a result of statistical treatment of the observable, In equation (3.21), gravity anomalies Δg_i were observed at discrete points i, and then the observations were used to predict geoid heights at the computation point P by exploiting the statistical dependency, i.e., covariance function between the observable Δg and the target quantity N. The LSC prediction of gravity anomalies Δg from residual geoid height ΔN can be found by manipulating equation (3.21) into

$$\Delta g = C^{\Delta N \Delta g^T} \left[C^{\Delta N \Delta N} + D_\Delta \right]^{-1} \Delta N, \tag{5.18}$$

where the expression has also been extended to include the error covariance matrix D_Δ of the residual geoid height. The theoretical background for the covariance matrices was derived in section 3.1.1, and a more detailed description of the covariance model used in this thesis will be given in the following section. For the datasets used in this thesis, see table 6.1, only the MSS alongside with the GGMs have a corresponding error field. The error covariance in equation (5.18) will therefore be $D_\Delta = \Sigma_{h_{MSS}}$, since the GGM's error field is already included in the computation of the covariance matrices. The formal errors, similar to equation (3.23), can be calculated as

$$\sigma^2_{\Delta g} = C^{\Delta g \Delta g} - C_{\Delta N \Delta g^T} \left[C^{\Delta N \Delta N} + D_\Delta \right]^{-1} C^{\Delta N \Delta g}. \tag{5.19}$$

As has earlier been described, and which is also very clear from equation (5.18) and (5.19), LSC depends solely on the statistical relationship between the observable and the target quantity described by the auto-covariance and cross-covariance matrices, respectively. To accurately model the residual signal's behaviour, a more detailed look at its component should be taken. Parts of the residual signal, even if it has a stochastic behaviour, can be explained from the different terms for the final observation equation of ΔN, as given by equation (5.17).

The formal errors, as given by equatin (5.19), are independent of measurements and can always be calculated based on the statistical relationship between the observation and target quantity. In cases where an independent set of observations are available then the calculation of empirical

errors is also possible. The empirical error is defined as the difference in estimated and measured value of the target quantity according to

$$\epsilon_{emp} = \Delta \hat{g} - \Delta g_{obs}, \tag{5.20}$$

where the notation $\hat{g}$ and g_{obs} is introduced to denote estimated and measured values, respectively. Ideally the empirical and formal errors should be of the same order, such that the measurements verifies the formal errors which are solidly a result of mathematical error propagation. In section 6 empirical and formal errors will be used as parameters to evaluate the contribution of RLSC prediction of gravity anomalies from residual geoid height using EGM2008, XGM2019e2159 and GOCO06s in the *remove-restore* step.

5.1.7 Modelling of the covariance function

Except for the GGMs, not much time has been spent on the error fields relating to the different components of the final observation equation. All terms on the right hand side are based on some models. In other words, all the terms are an approximation of the real world. GGM, for example, is a mathematical description of the Earth's geopotential represented by a spherical harmonic series expansion up to a maximum degree of $n = N_{max}$. To perfectly reproduce the true geopotential, then the model must contain an infinite number of terms. Even today with GGMs expanded up to a maximum degree of $N_{max} = 2190$, the model is still an approximation and will accordingly contain errors with respect to the true field. A more detailed handling of these problems might have been dealt with at an earlier stage, but first now as all the observation components, i.e., GGM, MSS and MDT, have been introduced I argue that a complete handling of the problem can take place.

A more complex notation could have been introduced in the beginning, where both MSS and GGM can be split into two components; a common component of the geoid signal N_{true} and a component that differs between the two models δ_{MSS} and δ_{GGM}. Introducing this extended notation gives

$$\begin{aligned} \Delta N &= h_{MSS} - N_{GGM} - h_{MDT} \\ &= (N_{true} + \delta_{MSS}) - (N_{true} + \delta_{GGM}) - h_{MDT} \\ &= \delta_{MSS} - \delta_{GGM} - h_{MDT}. \end{aligned} \tag{5.21}$$

The common (true) geoid signal N_{true} covered by both models will cancel each other out. The resulting residual geoid height ΔN will then accordingly consist of the difference between the MSS and the GGM, in addition to the MDT. With a perfect mathematical representation of the MSS and GGM up to the maximum degree used for the remove-restore step $N = N_{cut}$, then the residual geoid signal would truly be bandlimited between $N = [N_{cut}, \infty]$. Since both the MSS and GGM contains errors, their respective error contribution up to $N = N_{cut}$ will still be present in the signal. In section 2.2.3 the error contribution of a GGM was covered under the term *commission error*. The error-degree variances can be used to model the residual geoid height's signal for $N \leq N_{cut}$. Since error-degree variances are derived using the GGM's potential coefficients, then they represents the signal on a gloval scale for the spectral band $N \leq N_{cut}$. Following, the error-degree variances may not describe local conditions representative for the residual geoid height ΔN in the area under consideration. As was described in section 4, the solution is to introduce a scaling factor calculated from variance comparison between the local and global functions. The scaling will change the error signal strength such that it fits best possible with the residual geoid height signal in the respective spectral frequency domain. In contrary to the GGM, the error field relating to the MSS is represented as grid values alongside with the corresponding MSS values. To calculate error-degree variances from an error field is possible, but these calculations goes beyond this thesis. By only modelling the error signal strength of the GGM and then scale it to fit local effects, then it is assumed that degree variances for the GGM and MSS posses the same spectral characteristics. In that case, no significant error is introduced by using a simple scaling for the error-degree variances.

In this thesis, the *remove-restore* step is applied with the GGM's maximum degree truncated to a lower spherical harmonic degree of $N_{cut} = 1000$. Above $N = N_{cut}$ the residual signal consist mainly of the true geoid signal. Since the remove-restore step was calculated using a lower spherical harmonic degree than the GGM's maximum degree, then the signal components for $N_{cut} < N \leq N_{max}$ can be calculated using degree variances based on the model's potential coefficients. Even when using GGMs with a maximum degree of $N_{max} = 2190$, the marine gravity field signal still contains significant above the maximum degree (Zingerle et al., 2020). The Tscherning-Rapp model, equation (4.9) can be used for describing the signal strength above the GGM's maximum degree $N > N_{max}$.

In summary, the covariance functions consists of three parts:

1. Using the GGM's error-degree variances for modelling the residual geoid height's signal strength for the spherical harmonic degrees $N \leq N_{cut}$.

2. Using the GGM's degree variances for modelling the residual geoid height's signal strength for the spherical harmonic degrees $N_{cut} < N \leq N_{max}$.

3. Applying Tscherning-Rapp closed analytical covariance function for modelling the residual geoid height's signal strength above the GGM's maximum degree $N > N_{max}$.

From the findings in this section, a more detailed description of the residual signal's different components is now possible. Nguyen et al. (2020) uses equation (4.8) and (4.9) for modelling the stochastic relationship and spatial variation of the signal. Knudsen (1987) uses the same equations, but with other values assigned to the model parameters. In Nguyen et al. (2020), these parameters are determined using the GRAVSOFT software, while Knudsen (1987) provides a detailed description on how these parameters can be estimated in a least-squares adjustment. Since the remove-restore technique in this thesis is only performed up to N_{cut}, which is a lower spherical harmonic degree than the GGM's maximum degree, there is still potential coefficients available for $N_{cut} < N \leq N_{max}$. This leads to a slight adaptation to equation (4.8) and (4.9). The extended formulation of cross-covariance and auto-covariance functions will then be written as

$$C_{\Delta N_i \Delta g_P} = \frac{\alpha}{\gamma_i} \sum_{n=2}^{N_{cut}} \sigma_{c_n} \frac{n-1}{r_P} \left(\frac{R_E^2}{r_i r_p} \right)^{n+1} P_n \cos\psi + \frac{\alpha}{\gamma_i} \sum_{n=N_{cut}+1}^{N_{max}} c_n \frac{n-1}{r_P} \left(\frac{R_E^2}{r_i r_p} \right)^{n+1} P_n \cos\psi$$
$$+ \frac{1}{\gamma_i} \sum_{n=N_{max}+1}^{\infty} \frac{A}{(n-2)(n+b)} \frac{1}{r_P} \left(\frac{R_B^2}{r_i r_P} \right)^{n+1} P_n \cos\psi$$
(5.22)

and

$$C_{\Delta N_i \Delta N_i} = \alpha \sum_{n=2}^{N_{cut}} \sigma_{c_n} \frac{1}{\gamma_i \gamma_j} \left(\frac{R_E^2}{r_i r_j} \right)^{n+1} P_n \cos\psi + \alpha \sum_{n=N_{cut}+1}^{N_{max}} c_n \frac{1}{\gamma_i \gamma_j} \left(\frac{R_E^2}{r_i r_j} \right)^{n+1} P_n \cos\psi$$
$$+ \sum_{n=N_{max}+1}^{\infty} \frac{A}{(n-2)(n+b)} \frac{1}{\gamma_i \gamma_j} \left(\frac{R_B^2}{r_i r_j} \right)^{n+1} P_n \cos\psi,$$
(5.23)

where c_n and σ_{c_n} are degree variances and error-degree variances calculated using equation (2.32) and (2.33), respectively. Equation (4.8) and (4.9) are special cases of this extended formulation with $N_{cut} = N_{max}$. The error-degree variances, as for degree variances, expresses the error contribution of each spherical harmonic degree by the GGM up to N_{cut} on a global scale. The same scaling factor, as found for the degree variances, will be used to fit the commission error to local conditions. The extended formulation by equation (5.22) and (5.23) accounts for the commission error caused by the GGM. The MSS dataset is given as a grid of MSS and corresponding error estimates. Equation

(5.22) and (5.23) are derived using degree variances, so the inclusion of the MSS's error field is not straightforward from its original gridded representation. By assuming equal spectral properties of the error contribution of MSS and GGM, then the extended formulation with rescaling of the global covariance function will also account for the MSS's uncertainty. The scaling parameter for the global covariance function degree variances α is commonly estimated based on variance comparison from equation (4.10).

5.1.8 Final implementation of covariance function

Originally it was intended that the covariance modelling would be implemented following the approach found in Knudsen (1987); Heydarizadeh Shali et al. (2020), where both determines the model parameters by a least-squares adjustment. Due to time limitations in the work with this thesis, estimation of the model parameters α, R_B and A in equation (5.22) and (5.23) by least-squares adjustment could not be achieved. In addition, numerical investigations at a very late stage revealed problems with modelling the covariance functions by the extended formulation as shown in equation (5.22) and (5.23). These problems are related to the switch from error-degree variances to degree variances represented by the second and last term of equation (5.22) and (5.23). This switch in the computation of degree variances causes an unavoidable jump in value for the degree variances and result in odd-shaped covariance functions. In the following, a final treatment of how the covariance functions are implemented for GOCO06s, EGM2008 and XGM2019e2159 will be given.

In equation (5.23), the covariance function consist of three terms representing the commission and omission error of the RCR-method. The commission error is modelled by the first term containing the GGM's error-degree variance up to its truncation degree N_{cut}, while the omission error is modelled by the two last terms of equation (5.23) which consists of the potential coefficients from a high-resolution GGM for the spectral band $N \in [1001, 2190]$ and a Tscherning-Rapp covariance model for $N \in [2191, 10000]$. As was described in section 5.1.7, the covariance modelling used by Knudsen (1987) and Nguyen et al. (2020) is a special case of the extended covariance modelling represented by equation (5.23) with $N_{cut} = N_{max}$. Accordingly, only the relative weighting of two terms by least-squares adjustment is estimated.

Instead of assigning relative weights for each term, one common vector of dimensionless degree variances $c_{n_{tot}}$ is formed in the alternative approach. This degree variance vector consists of error-degree variances σc_n from a GGM, degree variances c_{GGM} between the truncation degree N_{cut} and the maximum degree of the GGM N_{max}, and at last analytical degree variances c_{TR} from a Tscherning-Rapp model for $N \in [1001, 2190]$. To summarise, the degree variances vector $\vec{c}_n$ is given by

$$\vec{c}_n = \begin{bmatrix} \sigma c_n \\ c_{GGM} \\ c_{TR} \end{bmatrix}, \tag{5.24}$$

and it is taken as input to an already implemented MATLAB routine for computing covariance functions based on degree variances. The resulting global covariance function from this combined degree variances vector is scaled based on variance comparison with the empirical covariance function. The only difference between this simplified approach and full least-squares adjustment, as represented by equation (5.23), is the determination of only one scaling coefficient. Still, the simplified approach is expected to closely resemble the optimal covariance function as given by Knudsen (1987); Nguyen et al. (2020).

To document the impact and improvement of a more complex covariance modelling, figure 5.3 shows the plotting of each term in equation (5.23) for the covariance function of residual geoid height $C^{\Delta N \Delta N}$ in the validation area. The covariance functions for the validation area, shown in figure 5.3, are estimated using already implemented MATLAB routines with degree variances as indicated by the legend of each curve. Comparison of the resulting global covariance functions
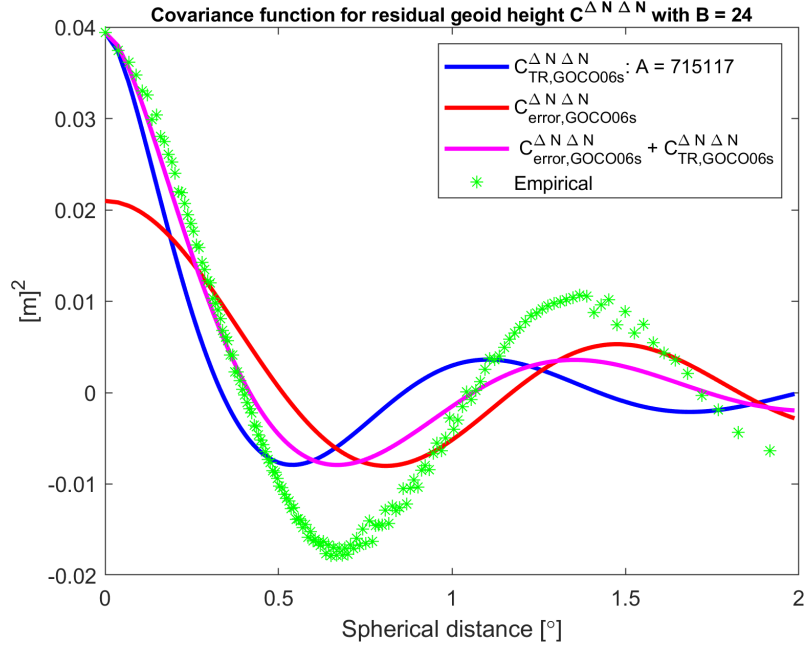
Figure 5.3: Investigation of the effects on the global covariance function for GOCO06s in the validation area by including different components for the degree variances computation. The three cases are calculated as follows; Red line: error degree variances of GOCO06s for $N \in [2, N_{cut}]$. Blue line: degree variances from Tscherning-Rapp for $N \in [N_{cut} + 1, 10000]$. Magenta line: Combination of degree variances used for the red and blue line. Green dots: Empirical covariance function.
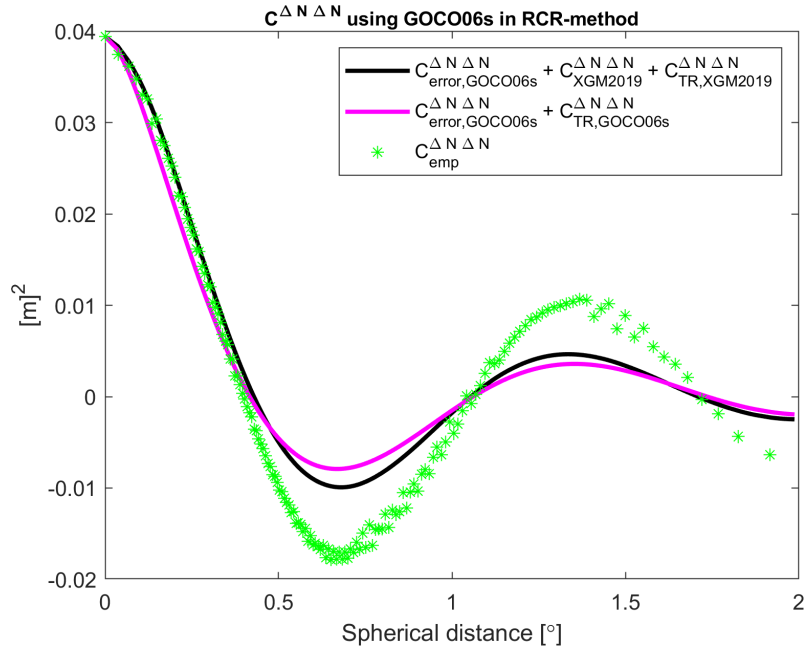

Figure 5.4: Covariance modelling for GOCO06s in the validation area using the most complex degree variances modelling. Black line: degree variances calculated according to equation (5.24). Magenta line: error degree variances of GOCO06s for $N \in [2, N_{cut}]$ and degree variances from Tscherning-Rapp for $N \in [N_{cut} + 1, 10000]$. Magenta line corresponds to the magenta line shown in figure 5.3. Green dots: Empirical covariance function.

44

with the empirical covariance function shows that inclusion of more terms and following a more sophisticated covariance modelling leads to a better approximation of the empirical covariance function. From figure 5.3 it is especially visible that the magenta line, where a degree variance vector formed by a combination of commission error and omission error is used, shifts the global covariance function such that its oscillation fits better with the empirical covariance function. This effect is expected as the empirical covariance function is considered to cover the complete spectrum, while red and blue curves are based on degree variances representing only part of the spectrum, i.e., the long wavelength and the medium to short wavelength. By combining these two degree variance vectors, the magenta curve again represents the full spectrum. From those investigations it is evident that inclusion of both commission and omission error gives a better covariance modelling. A more detailed modelling of the omission error can be further introduced by including degree-variances from a high-resolution GGM for the spectral band $N \in [N_{cut} + 1, N_{max}]$, and then only apply a Tscherning-Rapp model for the remaining spectral band $N \in [N_{max} + 1, 10000]$. Figure 5.4 shows the results by using this extended covariance modelling, and it can clearly be seen that it increases the covariance function's amplitude for large distances. The results for GOCO06s, documented in figure 5.3 and figure 5.4, verify the proposed covariance modelling approach. A natural next step is also to create global covariance functions when the high-resolution GGMs, EGM2008 and XGM2019e2159, are used for the *remove-restore* step. Using the same covariance modelling for EGM2008 and XGM2019e2159 results in odd-shaped analytical covariance functions as presented in figure 5.5a and figure 5.5b. A closer look needs to be taken in order to clarify and explain the very different covariance functions resulting from EGM2008 and XGM2019e2159 compared to GOCO06s. At first sight, it is surprising that the same method results in different analytical global covariance functions. From equation (5.23) it is evident that the Tscherning-Rapp component remains the same for all three models, so the difference must be caused by either of the two first terms relating to the degree variances c_{GGM} and error-degree variances σc_n given by equation (2.32) and equation (2.33), respectively. An investigation of the complete degree variance vector used for the most complex covariance modelling will be taken in the following. The complete degree variance vectors for EGM2008, XGM2019e2159 and GOCO06s are shown in figure 5.6a, 5.7a and 5.8a, respectively.
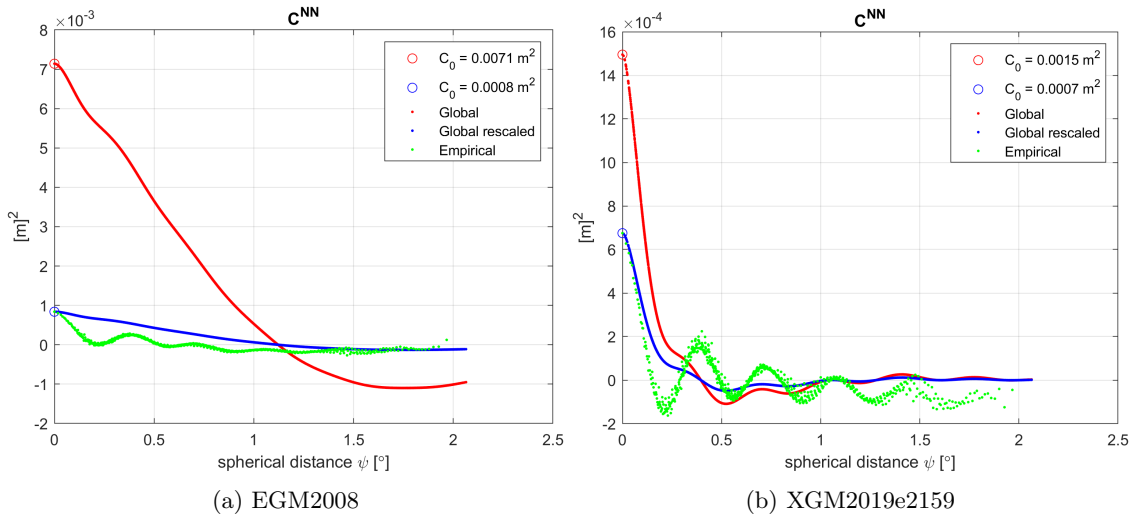

(a) EGM2008   (b) XGM2019e2159

Figure 5.5: Odd-shaped covariance functions for EGM2008 (left) and XGM2019e2159 (right) calculated from degree variances given by equation (5.24).

The covariance modelling using GOCO06s, shown by figure 5.3 and 5.4, showed that all components of the degree variances vector contributes to the final covariance function. GOCO06s also proved that the proposed approach, which was to create one common degree variances vector and introduce only one scaling coefficient, is a valid method for covariance modelling. As the general idea for the covariance modelling proves to be sufficient, then no further modification of the modelling approach for the covariance function is wanted.

Figure 5.6a and figure 5.7a shows the full degree variances vector ranging from spherical harmonic

degree 2 up to 10000 for EGM2008 and XGM2019e2159, respectively. It can clearly be seen that the degree variances vector contains jumps in the transition between its different components consisting of error-degree variances, degree variances and Tscherning-Rapp. For the RCR-method with EGM2008 and XGM2019e2159 there are jumps in the transition between all degree variances components, but for GOCO06s, shown in figure 5.8a, a jump in value only occurs in the connection between the high-resolution GGM and Tscherning-Rapp for degrees above the GGM's resolution. The degree variance vector's behaviour can in the case of GOCO06s be explained for the transition between error degree variances for GOCO06s and degree variances from XGM2019e2159. In Zingerle et al. (2020), a detailed explanation of the computation and observations of XGM2019e2159 can be found. The lower spherical harmonic degrees of XGM2019e2159 is mainly determined by the satellite-only model GOCO06s (Kvas et al., 2021), where the information from GOCO06s is introduced by its unconstrained normal equations. Then the potential coefficients of XGM2019e2159 and its standard deviations will be equal with the corresponding values of GOCO06s at the maximum spherical harmonic degree of the satellite-only model, this is also verified by Zingerle et al. (2020). Thereby, for the maximum degree of GOCO06s, i.e., where the error degree exceeds the degree variances, the error degree and degree variances will have the same value and accordingly no jump in degree variances will occur. A nice representation of relevant error-degrees and degree variances can be found in figure 4 of Zingerle et al. (2020). Another feature of figure 5.6a and 5.7a is that the degree variances decreases rapidly in the spectral band between $n = [2160, 2190]$. For all models there are a clear drop in the spectral band between $N \in [2160, 2190]$. This can be explained by the reduced signal strength for the potential coefficients of XGM2019e2159 in this range caused by the transformation from spheroidal harmonic to spherical harmonic domain. In the following, degree variances calculated from the potential coefficients of a high-resolution GGM will only be performed up to a spherical harmonic degree of 2159, and for the remaining spherical harmonic degrees up to 10000 by using the Tscherning-Rapp model. Still, figure 5.6a and figure 5.7a contain large jumps in the transition between degree variances calculated from the GGM's potential coefficients and the Tscherning-Rapp model for spherical harmonic degrees above the GGM's resolution. Degree variances for the anomalous potential T using Tscherning-Rapp is calculated according to

$$c_n(T,T) = \sigma_n^2(T,T) = \frac{A}{(n-2)(n+b)}, \tag{5.25}$$

and further transformed to dimensionless degree variances by use of the spectral eigenvalues and dimensioning factor of the anomalous potential T, see section 2.2, which finally results in the relationship

$$\sigma_n^2 = \frac{\sigma^2(T,T)}{\left[\frac{GM}{R}\right]^2} = \frac{1}{\left[\frac{GM}{R}\right]^2} \frac{A}{(n-2)(n+b)} \tag{5.26}$$

The scaling coefficient A is selected such that it best fits to the data. As a preprocessing step, the value of B is fixed to a value of $B = 24$. This has to be done, since the values of A and B are expected to be highly correlated. Different values for B exists in the literature, see Nguyen et al. (2020); Knudsen (1987); Heydarizadeh Shali et al. (2020). Initial tests, not shown here, confirmed that fixing B at an different value would be counter affected by a corresponding scaling of the A parameter. In the early stage of the thesis, when degree variances were exclusively modelled by using a Tscherning-Rapp model above the model's truncation degree N_{cut} up to a spherical harmonic degree of 10000, then this resulted in an estimated scaling coefficient of $A = 715116$, which is a similar value as was estimated by Knudsen (2007). Those initial computations did not account for the commission and omission error of the GGM, and in particular the Tscherning-Rapp model was already applied at the truncation degree N_{cut}, and not from the model's maximum degree N_{max}. Thereby, it is expected that the scaling coefficients will be considerable lower when using the extended covariance modelling. The scaling coefficient A can either be determined from visual inspection, or by introducing an additional scaling parameter β defined as

$$\beta_{TR} = \frac{c_{GGM}(N_{max})}{c_{TR}(N_{max})}, \tag{5.27}$$

and following the Tscherning-Rapp model will be scaled such that it fits with degree variances from the GGM's potential coefficients. To assure theoretical consistency the comparison of signal strength is performed at the spherical harmonic degree N_{max}. However, the Tschering-Rapp model can be evaluated for arbitrary degrees and will first be applied from $N_{max}+1$. From the Tscherning-Rapp model it can be shown that unmodelled signal components results in less than 1 cm for the geoid when spherical harmonic degrees larger than 5000 are neglected (Gerlach, 2019). In the following computations, all the effects discovered from figure 5.6a and figure 5.7a will be accounted for. Taking all those effects into consideration, then the final degree variances vectors to be taken as input for the covariance function routine in MATLAB are shown in figure 5.6b, 5.7b and figure 5.8b. Two jumps remain in the degree variances vector for XGM2019e2159 occurring at spherical harmonic degree of 720 and 1000, respectively. The jump at $N = 720$ is caused by change in dataset to forward-modelled gravity anomalies using a global topography model. The jump in value at $N = N_{cut} = 1000$ is natural as the degree variances component, see equation (5.24), is calculated from error degree variances for $2 \leq N \leq 1000$ and degree variances for $1000 < N \leq 10000$. No words have yet been said about degree variances for EGM2008, but they shows similar features as for XGM2019e2159. The degree variances vector does not contain a jump for spherical harmonic degree 720 as the computation of EGM2008 is performed using one consistent dataset. However, it still contains the same jump in value for $N = 1000$ due to the transition from error-degree variances to degree variances. The original and final degree variances for EGM2008 is shown in figure 5.6. From this analysis, all theoretical and numerical aspects, which first were encountered in the validation area, relating to degree variances has now been justified. The final implementation of degree variances and covariance functions will be performed according to

$$c_n = \begin{cases} \sigma c_n^{GGM} & 2 \leq n \leq N_{cut} \\ c_n^{HR-GGM} & N_{cut} < n \leq 2159 \\ \beta_{TR} c_n^{TR} & 2159 < n \leq 10000 \end{cases}, \tag{5.28}$$

where a new notation for high-resolution GGM (HR-GGM) is introduced such that equation (5.28) is valid for all GGMs, since the three models have a different truncation degree. A final flowchart of the implementation and calculation in MATLAB can be found in figure 6.1. The original and final degree variances vectors, calculated according to equation (5.28), are showed in figure 5.6, 5.7 and 5.8 for the different GGMs applied in the *remove-restore* step.

(a) Using original degree variances
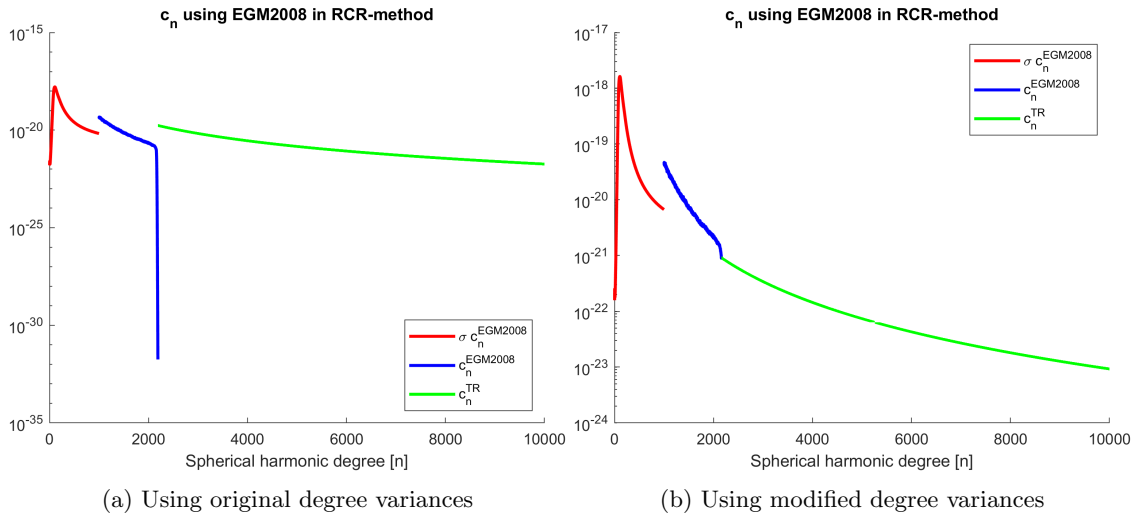
(b) Using modified degree variances

Figure 5.6: Comparison of degree variances calculated for RCR method with EGM2008. Figure 5.6a: original degree variances given by equation (5.24). Figure 5.6b: modified degree variances given by equation (5.28).
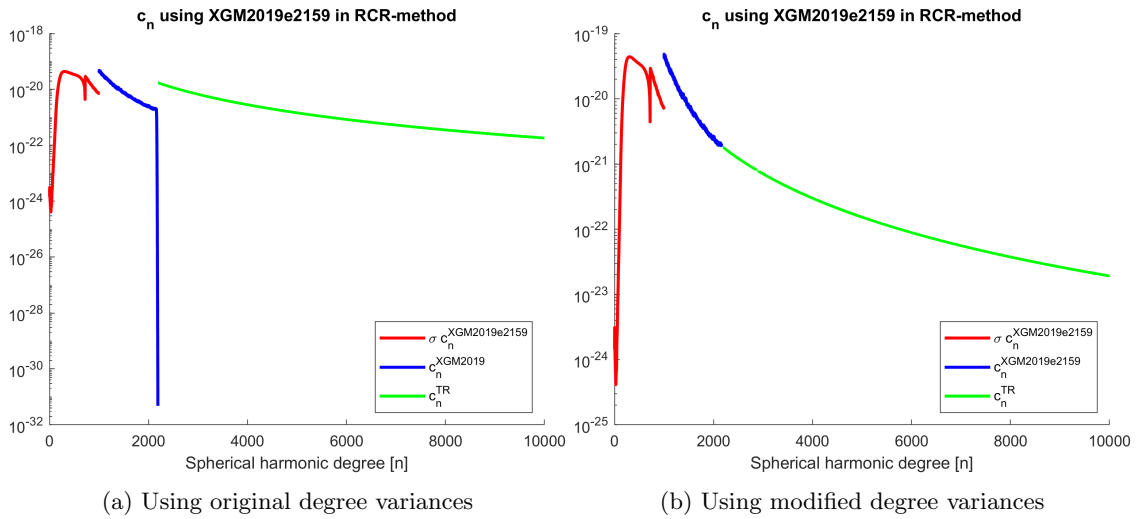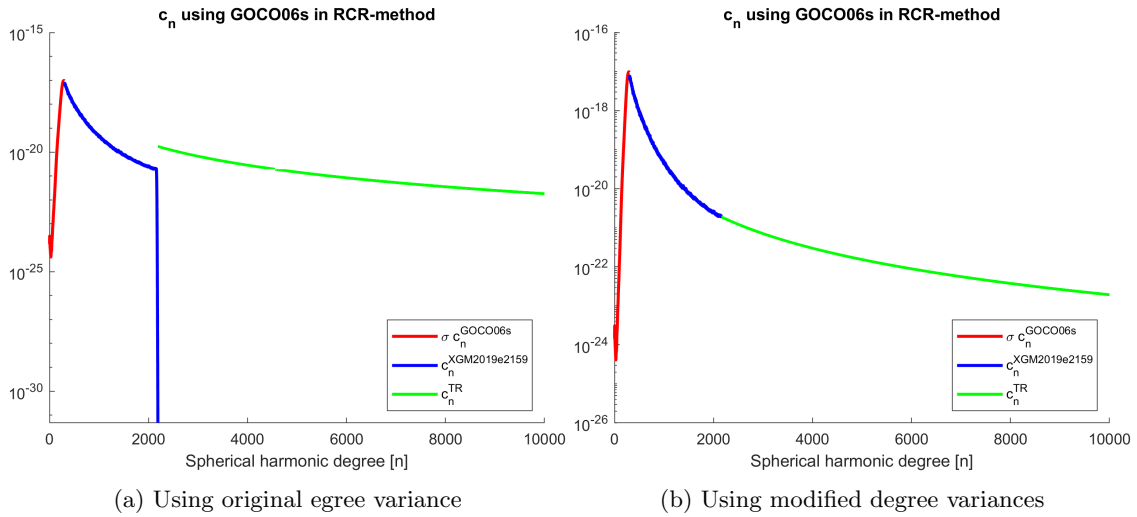

(a) Using original degree variances

(b) Using modified degree variances

Figure 5.7: Comparison of the degree variances calculated for RCR method with XGM2019e2159. Figure 5.7a: original degree variances given by equation (5.24). Figure 5.7b: modified degree variances given by equation (5.28).

(a) Using original egree variance   (b) Using modified degree variances

Figure 5.8: Comparison of the degree variances calculated for RCR method with GOCO06s. Figure 5.8a: original degree variances given by equation (5.24). Figure 5.8b: modified degree variances given by equation (5.28).

As a final check of the modified degree variances modelling, a comparison of the resulting global covariance functions with the empirical covariance is performed. Empirical covariance functions will be generated, by the method outlined in section 4.3, and used for scaling and comparison of the global covariance functions. The *remove*-step by applying the different GGMs results should result in a residual geoid height signal ΔN fulfilling the stochastic properties given in section 3, and accordingly also result in local empirical covariance functions with similar shape as the global covariance functions derived from potential coefficients. However, since the empirical covariance functions should reflect local effects and will be used for scaling the global covariance functions by variance comparison, the two functions are not expected to fit perfectly. The empirical covariance function should not contain any clear trends, then the residual signal contains some deterministic component and it violates with the stochastic requirement of LSC.

Figure 5.9a and 5.9b shows the corresponding global and empirical covariance functions of residual geoid height $C^{\Delta N \Delta N}$ for EGM2008 and XGM2019e2159, respectively. It was expected that a modified treatment of degree variances modelling would result in similar global covariance functions for all the GGMs, but figure 5.9 shows that still some problems exists for EGM2008 and XGM2019e2159.
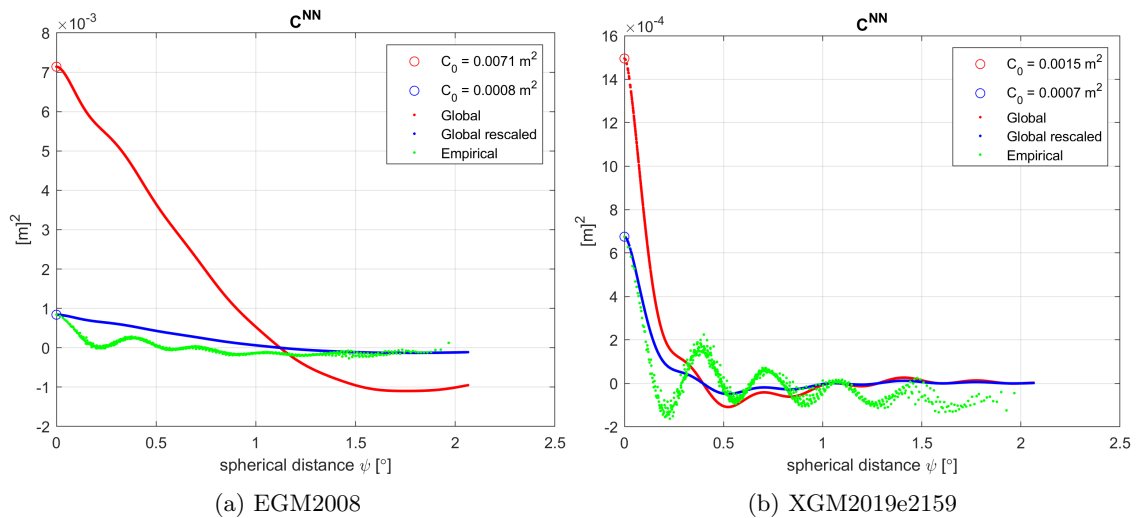

(a) EGM2008   (b) XGM2019e2159

Figure 5.9: Empirical and global covariance functions using the extended degree variances modelling given by equation (5.28). Figure 5.9a: EGM2008. FIgure 5.9b: XGM2019e2159.

As the cross-covariance functions between residual geoid heights ΔN and gravity anomalies Δg does not have any empirical results available to be used for scaling, then they are scaled with the same coefficient as the auto-covariance function for residual geoid height. This method is also in accordance with methods found in different literature (Knudsen, 1987; Nguyen et al., 2020). From the plots of analytical and empirical covariance functions it is visible that both EGM2008 and XGM2019e2159 results in odd-shaped covariance functions compared to GOCO06s, but more importantly they does not produce any good approximations of the real signal represented by the empirical covariance function. The small scaling coefficients of $\alpha_{EGM2008} = 0.1127$ and $\alpha_{XGM2019e2159} = 0.4667$ shows that the high-resolution GGMs have a poor fit to local effects. This can also be caused by wrongly selecting a too large initial scaling coefficient for the Tscherning-Rapp component, but, as seen from equation (5.27) for the simplified degree variances modelling, this problem has already been included and corrected for. One other possibility could be that the residual geoid height when using a high-resolution GGM for the *remove-restore* step up to a spherical harmonic degree of 1000 resulted in a residual signal with very low signal-to-noise ratio, and then no signal content is possible to model with LSC. This could have been observed by the empirical covariance function, and with a low signal amplitude, then also the contribution of LSC to the total gravity signal, according to equation (6.3), will become smaller. Due to the very low value of $\alpha_{EGM2008}$ and $\alpha_{XGM2019e2159}$, then small details for the empirical and global covariance function are hard to observe from figure 5.9a and 5.9b. In the case of XGM2019e2159, some of the same effects can be seen, but the global covariance function fits marginally better to the empirical values than for EGM2008. The only GGM resulting in a satisfying global covariance function is GOCO06s, as represented by figure 5.4. A separate plotting, not shown here, of the rescaled global and empirical covariance functions were made of EGM2008 and XGM2019e2159, but it only conformed the global covariance functions as poor approximation of the local signal, which is clearly visible from figure 5.9 as well.

As LSC is an estimation technique based on statistical relationship between the observables and target quantity, then empirical and formal errors based on prediction results using global covariance functions not resembling the empirical covariance function cannot be relied on. In order to give a final answer on the odd-shaped covariance functions, then the empirical errors and global covariance functions from an earlier LSC based on a different set of degree variances will be presented in the following.

Initially the residual geoid height signal was considered to be truly bandlimited restrictive to the spectral band $N \in [N_{cut} + 1, N_{max}]$. Accordingly, degree variances within this spectra was formed by the potential coefficients from a high-resolution GGM, i.e.,

$$\vec{c}_n = \begin{cases} c_n^{HR-GGM} & N_{cut} < N \leq 2159. \end{cases} \tag{5.29}$$

As a way to scale the Tscherning-Rapp component above the GGM's maximum degree was obtained by equation (5.27), the initial degree variances modelling in equation (5.29) can be extended with a Tscherning-Rapp term resulting in

$$\vec{c}_n = \begin{cases} c_n^{HR-GGM} & N_{cut} \ < N \leq 2159. \\ \beta c_n^{TR} & \begin{cases} 2159 \ < N \leq 10000 \text{ for XGM2019e2159} \\ 2140 \ < N \leq 10000 \text{ for EGM2008} \end{cases} \end{cases} \tag{5.30}$$

degree variances, calculated by equation (5.30), and corresponding global covariance functions for EGM2008 and XGM2019e2159 are shown in figure 5.10 and 5.11, respectively. Figure 5.6b shows for EGM2008 a rapid decrease in value for the spectral interval $N \in [2140, 2160]$, so to contour-act this effect for EGM2008 a Tscherning-Rapp model is already applied from $N = 2141$. Both figures shows a clear improvements by the covariance functions, which now resembles the empirical covariance in a similar manner as for GOCO06s. Comparison with figure 5.9a and 5.9b verifies that realistic global covariance functions can *only* be formed based on degree variances

free of large jumps in values. Accordingly, evaluation of EGM2008 and XGM2019e2159 will be based on empirical and formal errors derived from global covariance functions using equation (5.30) for degree variances modelling, and thereby it will not include the GGM's error-degree component. Since Knudsen (1987); Nguyen et al. (2020) uses the GGM up to its maximum degree, i.e., $N_{cut} = N_{max}$, they can avoid jumps induced by switching from error-degree variances to degree variances, and directly use least-squares adjustment to determine the model parameters shown in equation (5.23).

(a) Modified degree variances

(b) Modified global covariance functions
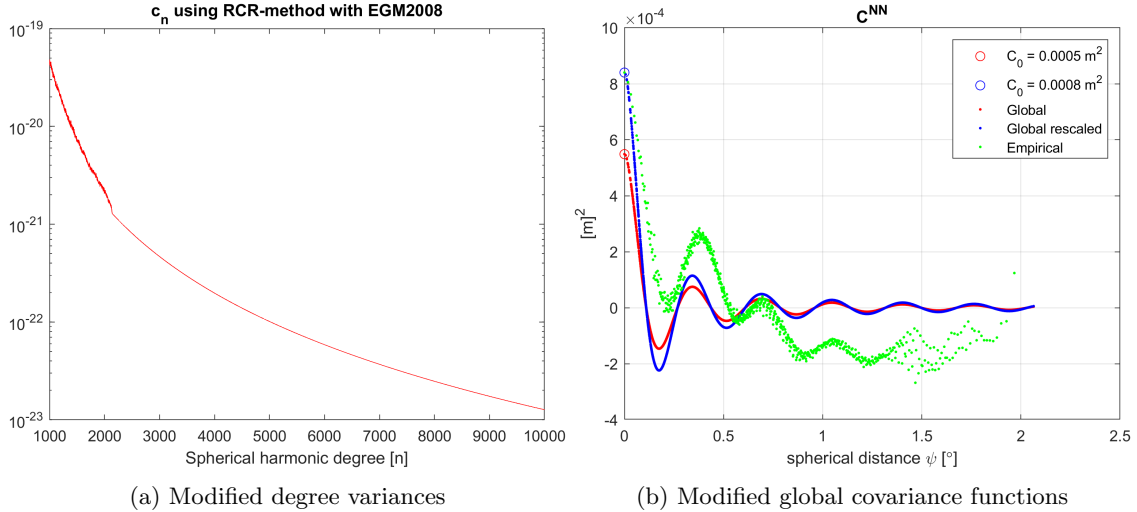
Figure 5.10: Modified approach for calculating degree variances according to equation (5.30) alongside with the resulting global covariance function for EGM200 using DTU13MSS as the MSS model.
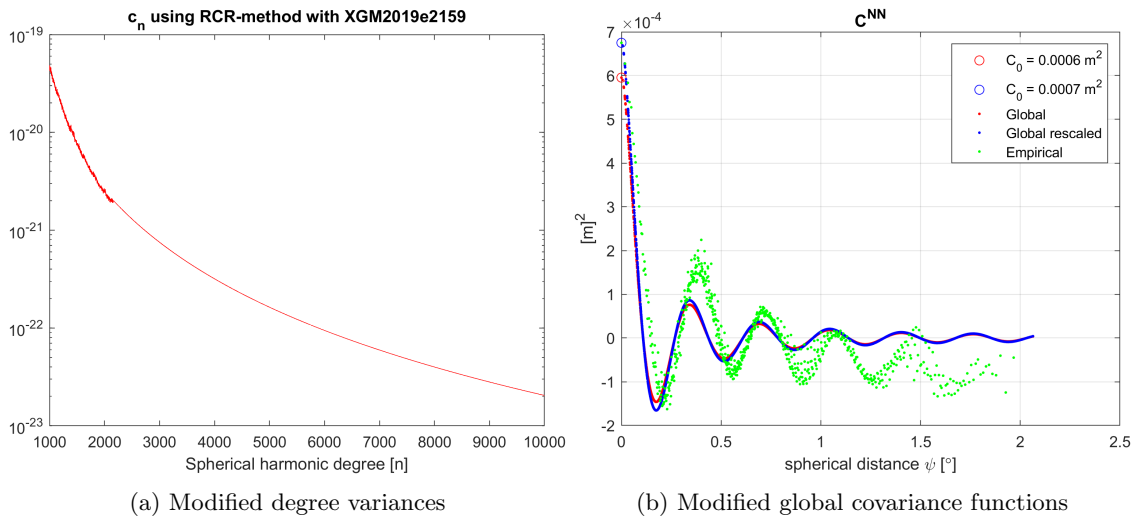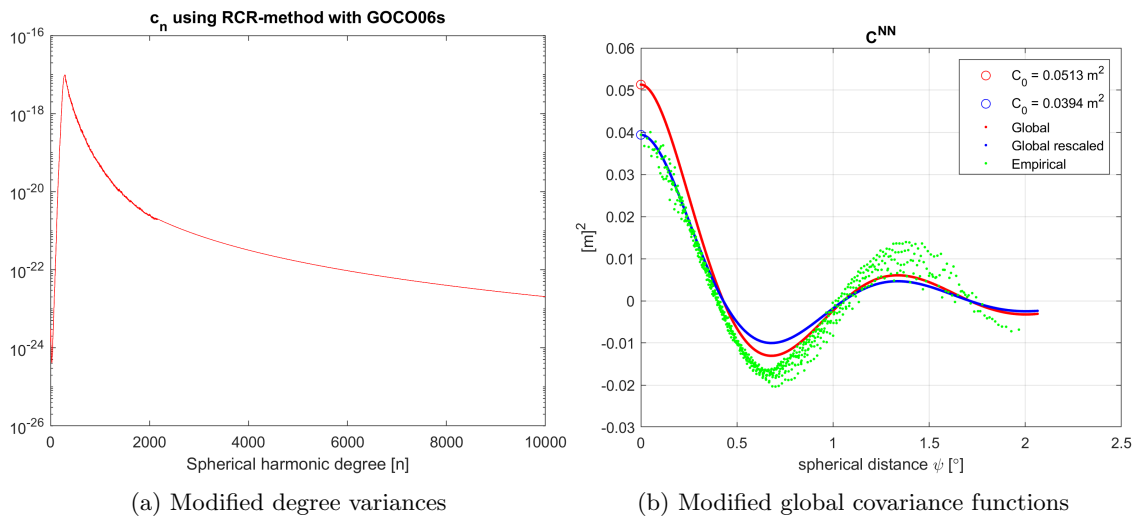

(a) Modified degree variances

(b) Modified global covariance functions

Figure 5.11: Modified approach for calculating degree variances according to equation (5.30) alongside with the resulting global covariance function for XGM2019e2159 using DTU13MSS as the MSS model.

(a) Modified degree variances

(b) Modified global covariance functions

Figure 5.12: Modified approach for calculating degree variances according to equation (5.30) alongside with the resulting global covariance function for GOCO06s using DTU13MSS as the MSS model.

Chapter 6

Numerical investigations

The datasets used in this thesis are Mean Sea Surface (MSS) - DTU18MSS (Andersen et al., 2018), DTU13MSS (Andersen et al., 2016), DTU13MDT (Andersen et al., 2016) and DTU13GRA (Andersen et al., 2014). Further description of the datasets, preprocessing and methods can be found in their corresponding references. An overview of the different datasets and their reference ellipsoids, tide systems, spatial resolution are shown in table 6.1.

Table 6.1: An overview of the different datasets and their specifications used in the LSC for the validation area.

	DTU13GRA	DTU13MDT	DTU13MSS	DTU18MSS
Spatial coverage	Global	Global	Global	Global
Spatial resolution[°]	1×1	$\frac{1}{60} \times \frac{1}{60}$	$\frac{1}{60} \times \frac{1}{60}$	$\frac{1}{60} \times \frac{1}{60}$
Reference period		1993-2013	1993-2013	1993.1-2013.0
Reference ellipsoid		TOPEX	TOPEX	WGS84
Tide system	Mean tide	Mean tide	Mean tide	Mean tide

In this thesis, the subject of study is gravity field modelling in marine areas, specifically along the Norwegian coast. Without presence of topography it is not necessary to apply a topographic gravity field model to remove topographic effects. Zingerle et al. (2020) state that even though the ocean geoid can be considered as a smooth surface compared with the land geoid, significant signal is still left above the maximum degree and order 2159. How to model the statistical behaviour of the remaining signal through covariance functions was explained in section 4. By truncating the high-resolution models to a maximum degree of $N_{cut} = 1000$ allowed the global covariance functions to be modelled with the potential coefficients above the truncation degree with already implemented routines in MATLAB. The degree variances above $N_{max} = 2190$ were further modelled using a Tscherning/Rapp covariance model.

In all computations the data area is sub-divided into a one smaller central target zone named "target area" and the whole area called "data area". This is done to overcome known boundary effects in regional gravity field modelling, and in order to compare results, then a smaller are free for boundary effects, i.e., the target area, is considered for comparison of empirical and formal errors. The calculation is done for the entire data area, so the target area is just a sub-area used for validation purposes. Throughout this thesis a significant amount of time has been devoted to the limitation of memory storage. All numerical calculations has been done in MATLAB on a basic computer, Lenovo ThinkPad E460 with Core i5-6200U processor (Lenovo, 2020). The storage limitation is due to the computer's RAM availability, no problems are related to MATLAB itself. Due to limited computational capacity the maximum number of observations that can be handled in the LSC calculations are 14400. The resulting covariance matrix with a dimension of $[14400, 14400]$ uses close to 8GB storage which is the computer's RAM size. The whole scripts with
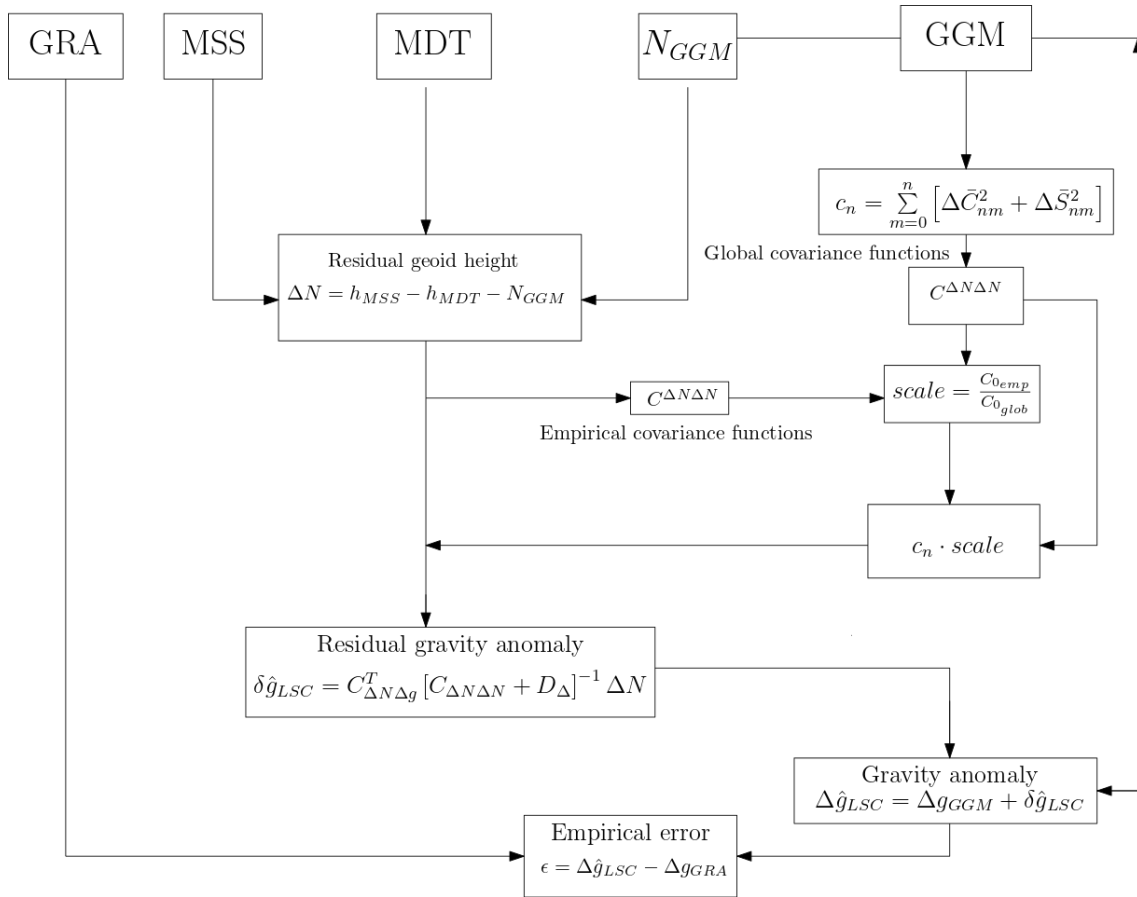
GRA   MSS   MDT N_{GGM} GGM

$$c_n = \sum_{m=0}^{n} \left[\Delta \bar{C}_{nm}^2 + \Delta \bar{S}_{nm}^2 \right]$$

Residual geoid height
$$\Delta N = h_{MSS} - h_{MDT} - N_{GGM}$$

Global covariance functions

$C^{\Delta N \Delta N}$

$C^{\Delta N \Delta N}$

Empirical covariance functions

$$scale = \frac{C_{0_{emp}}}{C_{0_{glob}}}$$

$c_n \cdot scale$

Residual gravity anomaly
$$\delta \hat{g}_{LSC} = C_{\Delta N \Delta g}^{T} \left[C_{\Delta N \Delta N} + D_{\Delta} \right]^{-1} \Delta N$$

Gravity anomaly
$$\Delta \hat{g}_{LSC} = \Delta g_{GGM} + \delta \hat{g}_{LSC}$$

Empirical error
$$\epsilon = \Delta \hat{g}_{LSC} - \Delta g_{GRA}$$

Figure 6.1: The implementation and processing strategy in MATLAB used for LSC of gravity anomalies from residual geoid heights.
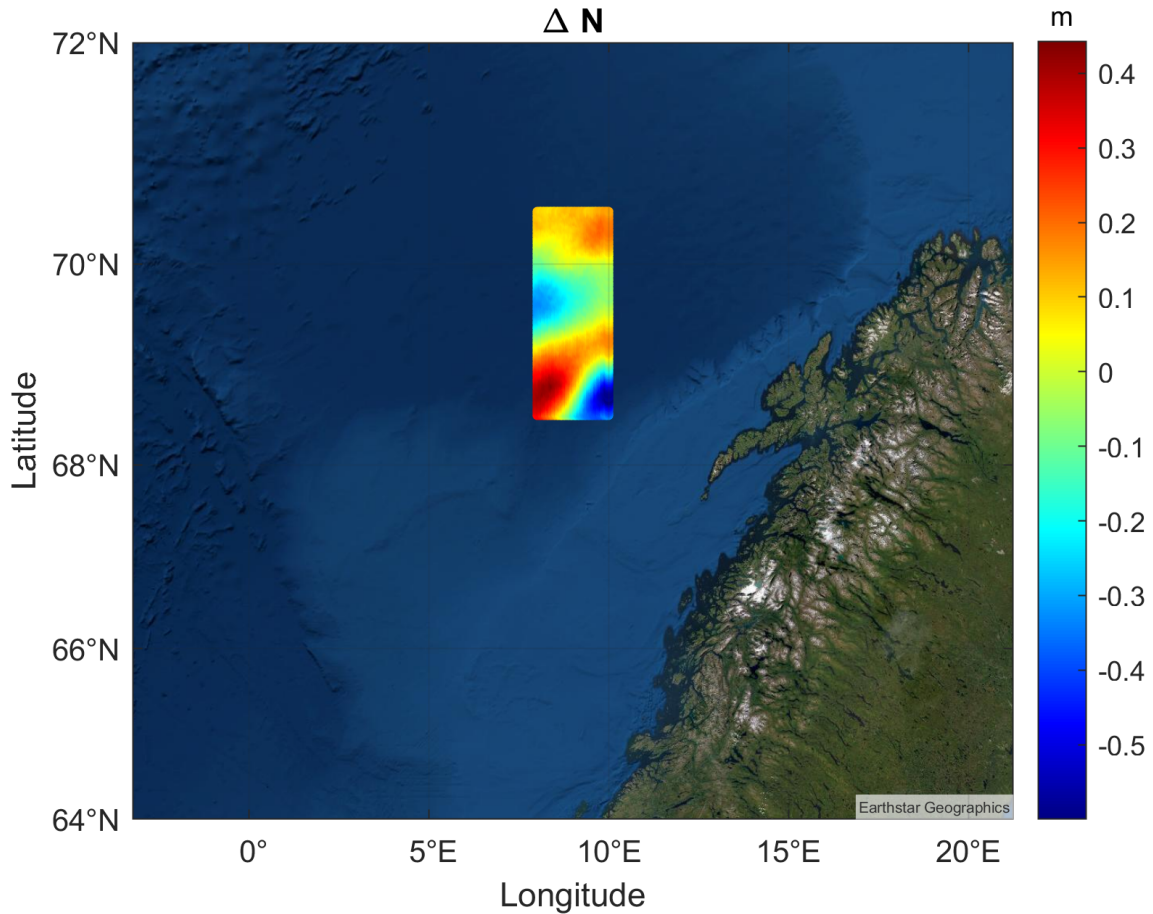
Figure 6.2: Area used for validating LSC implementation in MATLAB. The data covers a region of $\phi = [68.5, 70.5]$ and $\lambda = [8, 10]$. Here the residual geoid height ΔN is calculated according to equation (5.17) with GOCO06s and DTU18MSS.

creating residual geoid heights, covariance and cross-covariance functions, LSC and calculation of empirical and formal errors spends around 20 minutes, where a substantial part is used on creation and saving of figures. A final upgrade to 16 GB RAM size reduced the run time to 10 minutes, and test simulations at a rather late stage shows that LSC predictions can be carried out with a total number of observations between $15000 - 16000$. The large computational power of LSC is one of its drawbacks, but still on a regular computer it is possible to predict gravity anomalies Δg from residual geoid heights ΔN for an area of sufficient size according to this thesis' objective.

6.1 Validation of least-squares collocation

As an initial test to verify the implementation of LSC in MATLAB, a small area outside of the Norwegian coast was chosen. The validation area is shown in figure 6.2 and extends over $\phi = [68.5, 70.5]$ and $\lambda = [8, 10]$, which is approximately 150 km from the Norwegian coast such that any coastal effects on the altimetry data can be neglected. The validation is both performed using a satellite-only gravity field model, GOCO06s (Kvas et al., 2021), with a maximum degree of $N_{cut} = 300$, and two high-resolution gravity field models, EGM2008 and XGM2019e2159, with its maximum degree truncated to $N_{cut} = 1000$. Further details about the selection criteria for the GGMs is explained in section 2.2.

In this area, gravity anomalies Δg from DTU13GRA is used as validation data for the LSC predictions. DTU13GRA is based on a large amount of the same observations, but the processing strategies differ so the validation does not strictly follow a *closed-loop* simulation. The global model

DTU13GRA is calculated by applying a Tscherning-Rapp model for interpolating residual geoid heights at a regular grid, and secondly using the fast fourier techniques (FFT) for the transformation between residual geoid height and gravity anomalies (Andersen et al., 2015). However, small deviations between the total gravity signal based on LSC and DTU13GRA can be used to validate the implementation of LSC in MATLAB. Nguyen et al. (2020), in their research on marine gravity modelling from Cryosat-2 and Saral/AltiKa satellite altimetry data, reports empirical errors of their LSC satellite altimetry derived gravity anomalies compared to DTU13GRA as

$$\epsilon_{Nguyen} = 2.94 \pm 5.73 \text{ mGal} \tag{6.1}$$

with errors ranging from $[-44.13 \text{ mGal}, 40.16 \text{ mGal}]$. Empirical and formal errors for LSC smaller than 2 mGal, or of similar size as found in Nguyen et al. (2020), are used as validation criteria in the validation area. The validation area consist of 14400 observations, which results in covariance matrices with dimensions of 14000×14000 and a total of 196000000 elements. The implementation and processing of LSC is shown in figure 6.1, which is greatly inspired by the scheme found in Nguyen et al. (2020).

Two different MSS models, DTU13MSS (Andersen et al., 2015) and DTU18MSS, are available, so the numerical investigations will be divided into two parts, where the only difference between the two is the selection of the MSS model. The reason for using two different MSS models is to see if any systematic effects caused by dependencies between any of the components in equation (5.17) shows up in the empirical or formal errors. All computations are performed following the implemented scheme as represented by figure 6.1, so for further details about each processing step I will refer to that figure whenever it is relevant.

For comparison in order to evaluate the different GGMs, plots of residual gravity anomaly will be made according to

$$\Delta g_{res} = \Delta g_{SHS} - \Delta g_{DTU13GRA}, \tag{6.2}$$

where Δg_{SHS} is gravity anomaly resulting from SHS, given by equation (2.28), using spherical harmonic coefficients up to spherical harmonic degree N_{cut} from the GGM under consideration, while $\Delta g_{DTU13RA}$ is gravity anomalies from the global model DTU13GRA (Andersen et al., 2014). LSC works on a residual geoid height signal ΔN consisting of short wavelength characteristics, and accordingly the LSC can contribute with determination of the gravity field signal's short wavelength components. The total gravity anomaly signal, after the *restore*-step, is given by

$$\Delta \hat{g}_{tot} = \Delta g_{SHS} + \Delta g_{LSC}, \tag{6.3}$$

and accordingly another set of residual gravity anomalies can be calculated by comparison with DTU13GRA

$$\epsilon\left(\Delta g_{LSC}\right) = \Delta \hat{g}_{tot} - \Delta g_{DTU13GRA}. \tag{6.4}$$

The contribution by LSC is evaluated based on its effect on mean value, standard deviation and extremal values of the empirical error, obtained by equation (6.4), compared to the same descriptive statistics for the residual gravity anomaly signal formed by equation (6.2). The two sets of residual gravity anomaly fields only differs by the LSC of gravity anomaly, then the contribution by LSC can be evaluated based on its influence on the empirical errors' statistical parameters compared to the residual gravity anomaly signal. In case their values are similar, then a very limited contribution by LSC can be offered, and vice versa. Residual gravity anomalies for EGM2008, XGM2019e2159 and GOCO06s are shown in figure 6.7b, 6.8b and 6.9b, respectively.

6.1.1   LSC estimates using DTU13MSS as mean surface model

The residual geoid height for the different GGMs are shown in figure 6.3, 6.4 and figure 6.5. Here the residual geoid height is shown before it has been reduced by its own mean value, which is performed in order to compare the prediction results based on different GGMs and also to optimally fulfill the stochastic requirements as was explained in section 5.1. From plots of residual geoid height, as is shown by the respective figures, no conclusion can be drawn about the stochastic properties for the residual field. One feature that should be noticed is the much larger signal variance of ΔN when using GOCO06s for the *remove*-step. An increased signal variance for GOCO06s is to be expected, as the gravity field's long wavelength components are only removed up to a spherical harmonic degree of 300, compared with 1000 for EGM2008 and XGM2019e2159. The covariance functions for EGM2008, XGM2019e2159 and GOCO06s were shown in figure 5.10, 5.11 and figure 5.12, respectively.
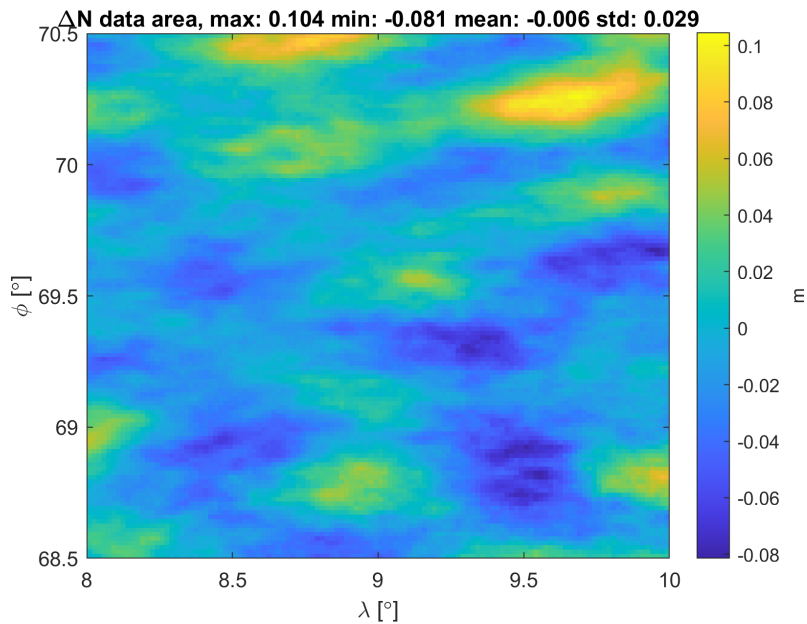
Figure 6.3: Residual geoid height, calculated according to equation (5.17), using EGM2008 for removement of the gravity field's long wavelength components.
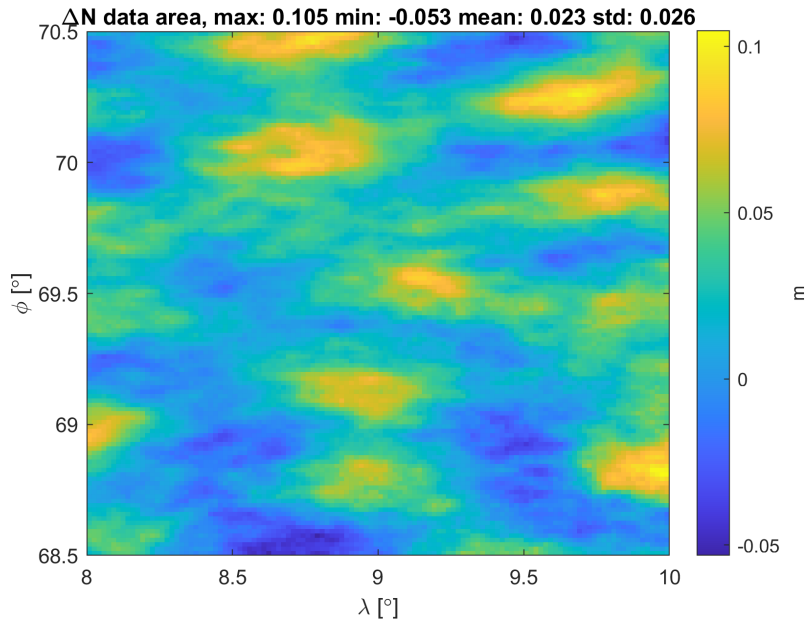
Figure 6.4: Residual geoid height, calculated according to equation (5.17), using XGM2019e2159 for removal of the gravity field's long wavelength components.
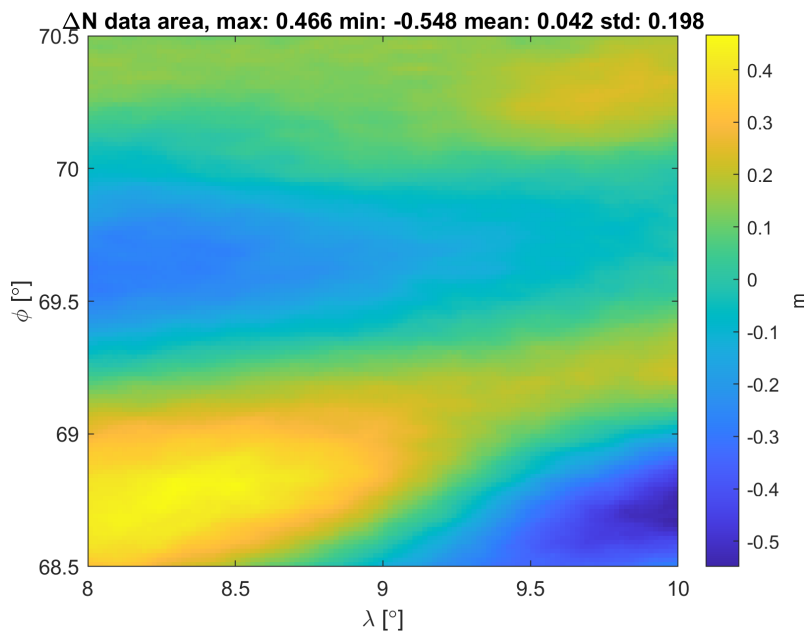

Figure 6.5: Residual geoid height, calculated according to equation (5.17), using GOCO06s for removal of the gravity field's long wavelength components.

One last important quantity of LSC, as given by equation (5.18), is the MSS' accuracy. The error covariance matrix D_Δ is a diagonal matrix consisting of squared values from the MSS error field at the observation points. Figure 6.6 shows the error field for DTU13MSS with values ranging from $1.5 - 1.9$ mGal. Adding values along the diagonal of the covariance matrix gives a numerical more stable system, but one side-effect is that it has a smoothing effect on the signal.

Table 6.2: Descriptive statistics for empirical errors, according to equation (6.4), when using DTU13MSS as the MSS model and the respective GGMs alongside with residual gravity anomaly given by equation (6.2). All quantities have unit mGal.

Difference of total gravity signal from LSC and DTU13GRA	DTU13MSS				$\Delta g_{SHS} - \Delta g_{DTU13GRA}$			
	min	max	mean	std	min	max	mean	std
EGM2008	-7.283	5.850	0.044	1.877	-10.204	9.826	-0.106	3.629
XGM2019e2159	-8.360	5.811	-0.465	1.920	-9.930	9.145	-0.578	3.589
GOCO06s	-6.738	4.810	-0.688	1.680	-23.332	14.023	-2.233	8.186
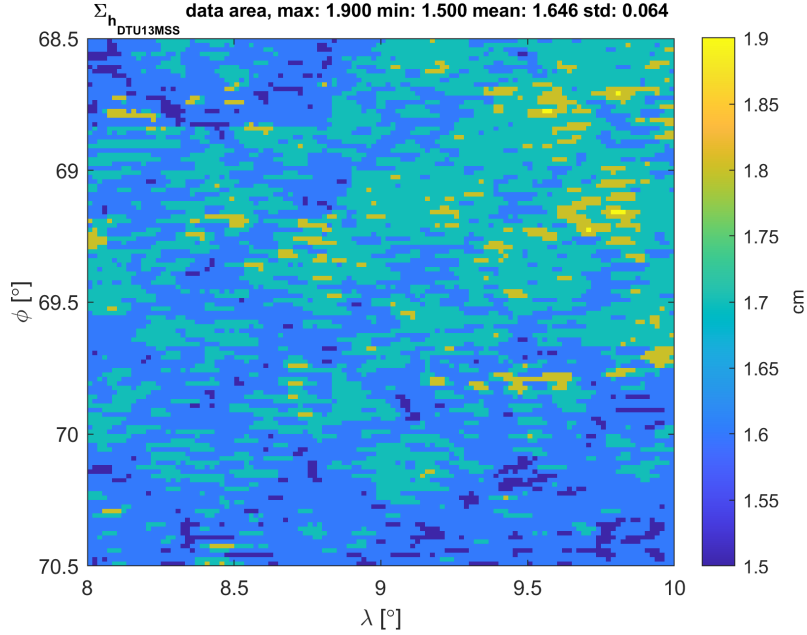
Figure 6.6: Corresponding error-field of DTU13MSS. Notice that the error-field is shown with unit of cm.

The residual gravity anomaly signal formed by equation (6.2) are shown in figure 6.7b, 6.8b and 6.9b, while the empirical errors derived by equation (6.4) are shown in figure 6.7a, 6.8a and 6.9a. All figures are in the order of EGM2008, XGM2019e2159 and GOCO06s, respectively. A summary of the descriptive statistical parameters are shown in table 6.2. It can clearly be seen a contribution by LSC from all the GGMs. However, the reduction is largest in the case of GOCO06s. This can in particular be explained by its well approximating global covariance function, and also its higher SNR for the residual geoid height signal. EGM2008 obtains a smaller value for both the mean value and standard deviation compared to XGM2019e2159. Especially, its mean value is by a factor 10 smaller than for both XGM2019e2159 and GOCO06s. This might be explained by a better consistency between DTU13MDT and EGM2008. DTU13MDT is calculated as a difference between DTU13MSS (Andersen et al., 2016) and EIGEN-6C3 (Foerste et al., 2011), where EIGEN-6C3 in turn uses EGM2008 as surface data for their computation.

GOCO06s shows very promising results, where the mean value and standard deviation for the empirical errors in figure 6.9a are reduced by 79 % and 63%, respectively, compared to the residual gravity signal shown in figure 6.9b. Also for EGM2008 and XGM2019e2159 LSC contributes to a large reduction. These results are in accordance with the principal of model independence for the RCR-method. GOCO06s achieves the lowest standard deviation which shows that a satellite-only model can be used as GGM for the *remove-restore* step, in addition it again validates the extended covariance modelling represented in section 6 when degree variances are free of jumps in value.
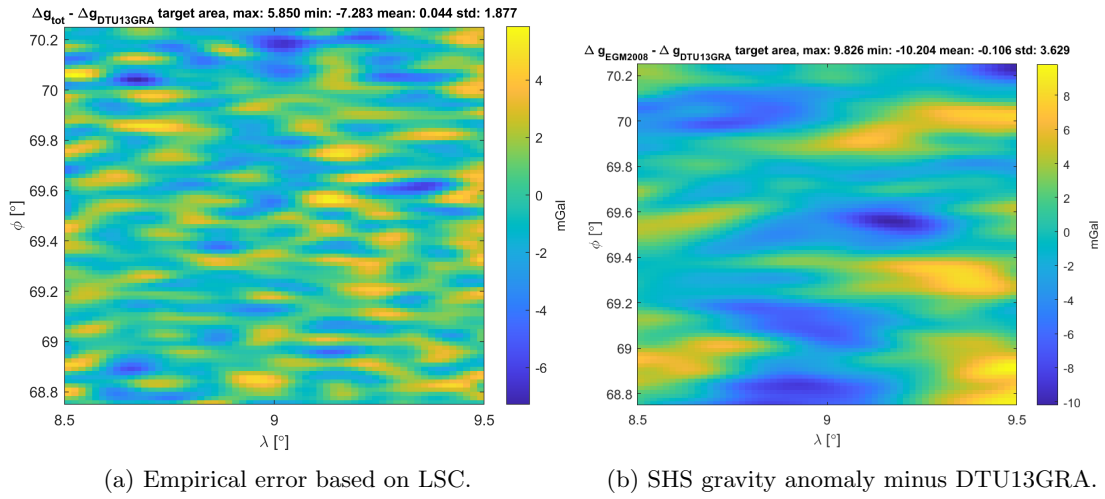
(a) Empirical error based on LSC.

(b) SHS gravity anomaly minus DTU13GRA.

Figure 6.7: Evaluation of the contribution by the LSC of gravity anomalies from residual geoid height using EGM2008 for the remove-restore step.
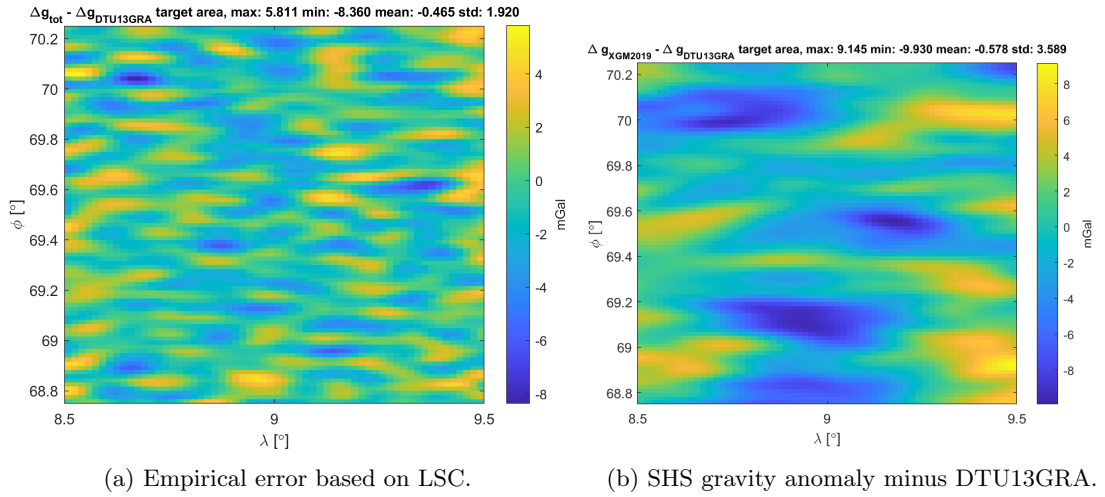

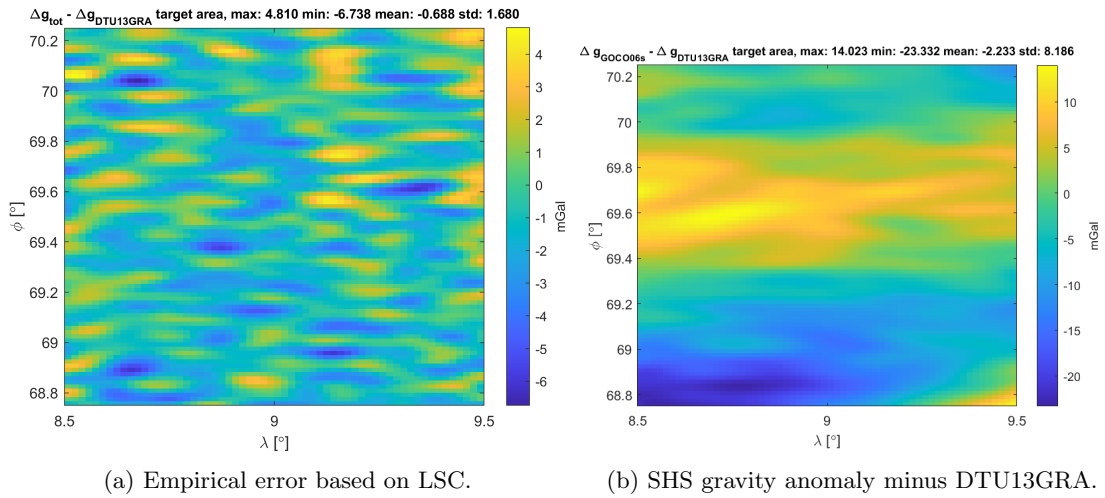(a) Empirical error based on LSC.

(b) SHS gravity anomaly minus DTU13GRA.

Figure 6.8: Evaluation of the contribution by the LSC of gravity anomalies from residual geoid height using XGM2019e2159 for the remove-restore step.

(a) Empirical error based on LSC.

(b) SHS gravity anomaly minus DTU13GRA.

Figure 6.9: Evaluation of the contribution by the LSC of gravity anomalies from residual geoid height using GOCO06s for the remove-restore step.

As a final step the formal error are predicted according to equation (5.19) and shown in figure 6.10, 6.11 and 6.12 for EGM2008, XGM2019e2159 and GOCO06s, respectively. Again I will emphasize that formal errors calculated by equation (5.19) are independent of observations, and they are exclusively determined using error-propagation of the target guantity' mathematical relationship to the observations described by the auto-covariance function and cross-covariance function. All models produce a homogeneous error field, where again GOCO06s posses the smallest values. The three models only marginal differs from each other showing a consistent covariance modelling. All plots of formal errors shows increasing errors in-between the satellite tracks. A more sparse sampling is existing in these regions compared to along the satellite tracks, and the LSC of gravity anomaly will then rely more on observations further away compared to points along the satellite track. Compared with the empirical errors it can be seen that the formal errors represents an upper bound estimate. Practically, this is a lot safer than producing a too optimistic error estimate, because altimetry derived gravity anomalies can be included in other estimations where corresponding weights safely can be assigned according to the formal errors. The main thesis objective was to investigate the possibility of predicting gravity anomalies from residual geoid height, and accordingly the results from all GGMs proves this to be possible. In the following section, the same LSC using DTU18MSS as mean sea surface model will be carried out.
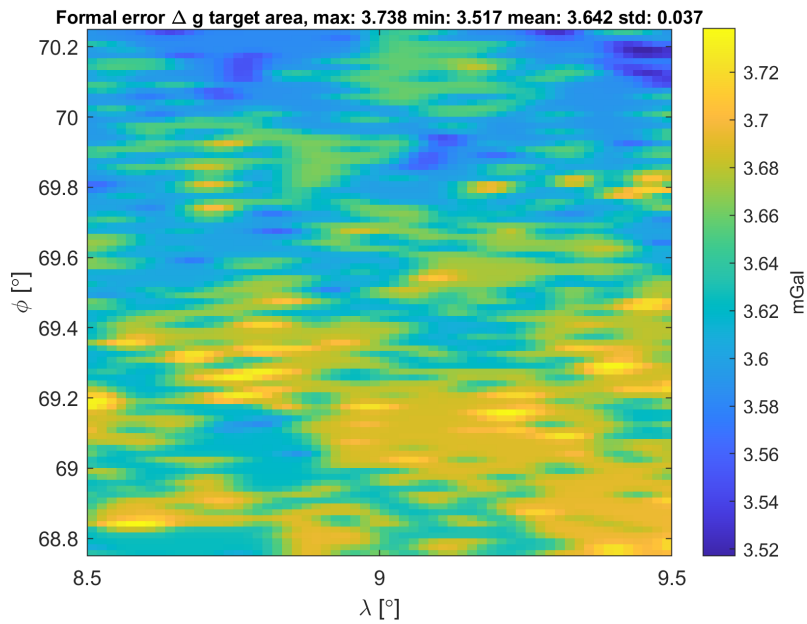

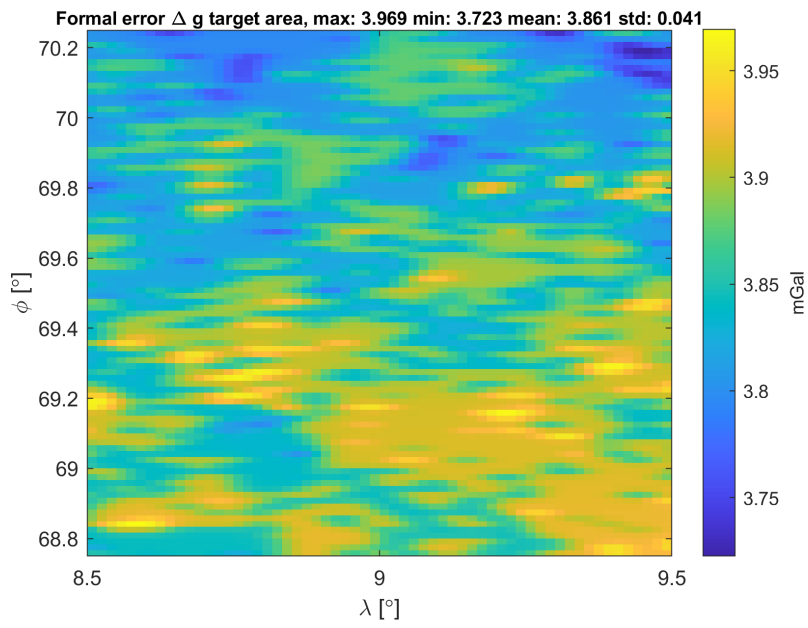Figure 6.10: Formal errors using covariance functions with EGM2008.

Formal error △ g target area, max: 3.969 min: 3.723 mean: 3.861 std: 0.041

Figure 6.11: Formal errors using covariance function with XGM2019.

Formal error △ g target area, max: 3.476 min: 3.285 mean: 3.391 std: 0.032
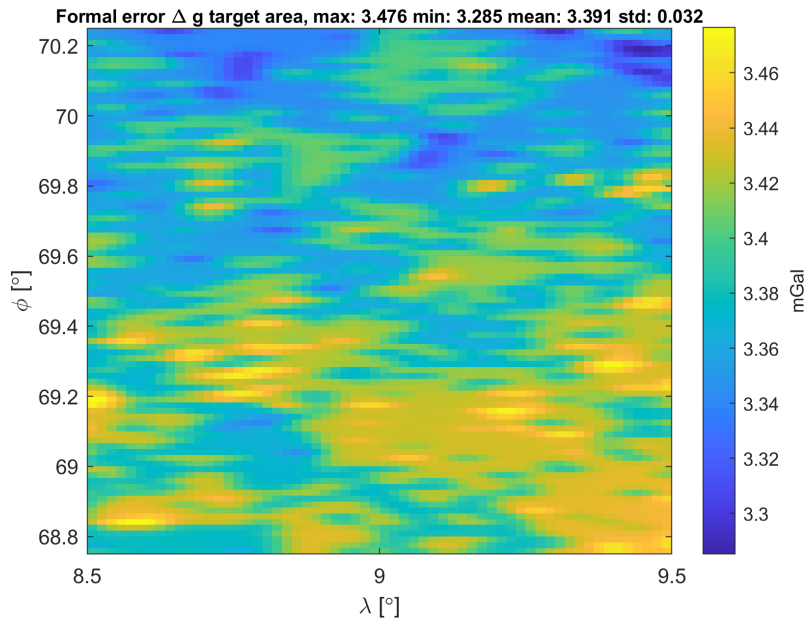

Figure 6.12: Formal errors using covariance function with GOCO06s.

6.1.2 LSC estimates using DTU18MSS as mean sea surface model

As degree variances modelling is independent of mean sea surface model, except from scaling by variance comparison with the empirical covariance function, then the same degree variances modelling for EGM2008 and XGM2019e2159 will be applied in these numerical estimations using DTU18MSS as mean sea surface model. Again, first the residual geoid height ΔN is calculated using the different GGMs for the *remove*-step. Isolated by the residual plots shown in figure 6.13, 6.14 and 6.15 no clear conclusions can be drawn. A plot of residual geoid height works as a visual check to verify that the computations by equation (5.17) has resulted in a stochastic signal. From a comparison between figure 6.5 and 6.15 it can be seen that the mean value is reduced by 3.4 cm for GOCO06s. The standard deviation, and thereby also the signal variance, is unchanged which means that the mean value calculated for the residual geoid height of GOCO06s in the case of DTU13MSS, as represented in figure 6.5, reflects a pure offset between the two datasets.
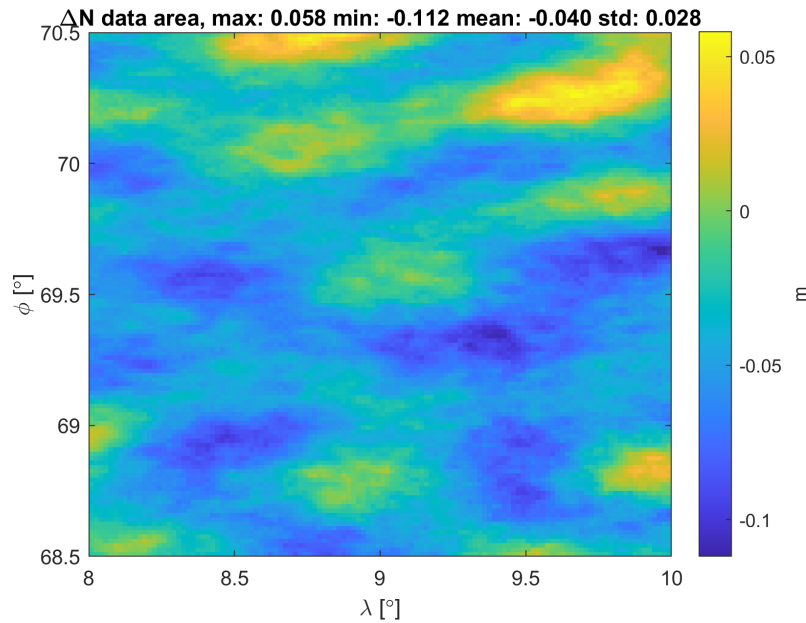

Figure 6.13: Residual geoid height when using EGM2008 and DTU18MSS.
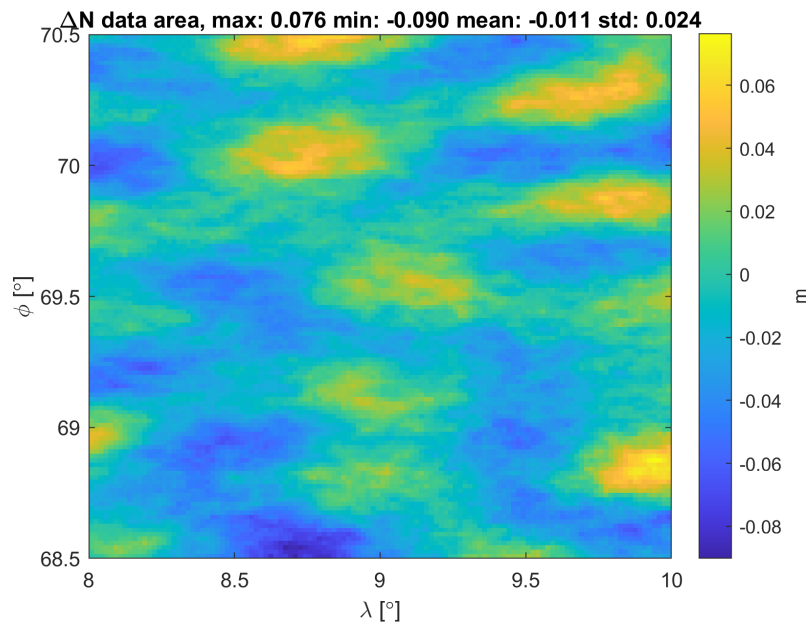

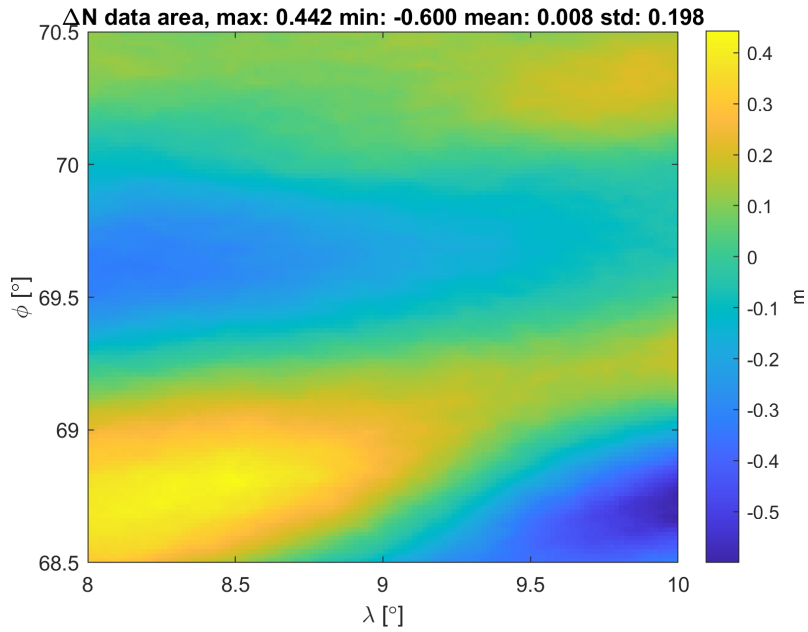Figure 6.14: Residual geoid height when using XGM2019e2159 and DTU18MSS.

Figure 6.15: Residual geoid height when using GOCO06s and DTU18MSS.

The error-field of DTU18MSS is shown in figure 6.16. By comparison with figure 6.16 it can be verified that DTU13MSS and DTU18MSS have error-fields of similar size. DTU18MSS has a slightly larger mean value and standard deviation by 0.1 cm, and it shows a more defined pattern for the satellite tracks. However, these slight differences are expected to not have any great influence on the empirical and formal errors of LSC.
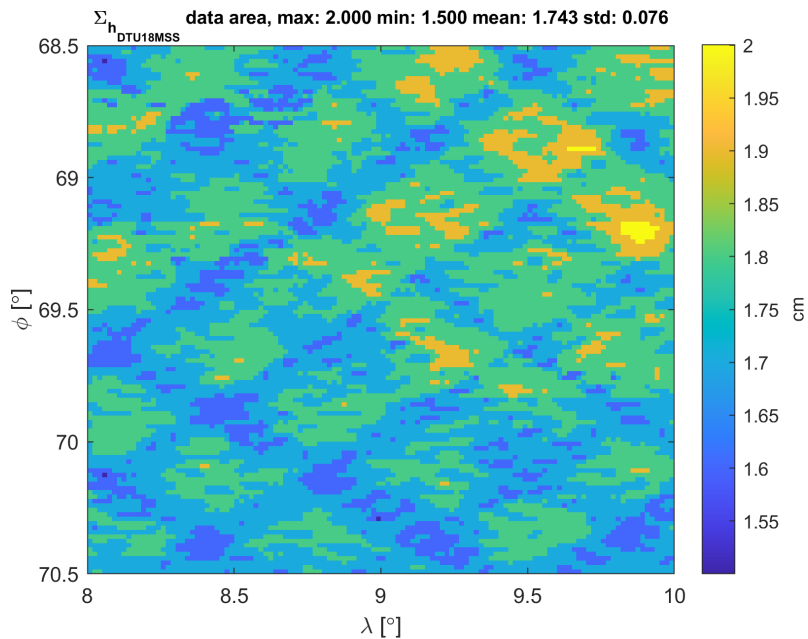

Figure 6.16: Corresponding error-field of DTU18MSS. Notice that the error-field is shown with unit of cm.

The corresponding global and empirical covariance functions using the three GGMs are shown in figure 6.17b, 6.18b and 6.19b. Since the same degree variances are used for the computations as was shown in section 6.1.1, then the left parts of the respective figures shows the cross-covariance function between residual geoid height and gravity anomaly $C^{\Delta N \Delta g}$. No remarks on the empirical covariance functions were given in the numerical calculations with DTU13MSS, but now as

similar functions have been derived using DTU18MSS, then a closer inspection of the empirical covariance functions behaviour will be made. Comparison of the empirical covariance functions using DTU13MSS and DTU18MSS shows only minor differences depending on the different MSS models. However, the empirical covariance functions of residual geoid height $C^{\Delta N \Delta N}$ generated by using different GGMs as part of the *remove*-step shows some differences. XGM2019e2159, figure 5.11b and 6.18b, shows signs of a small negative trend with larger distances. This negative trend is very marginal, so performing a reduction by a linear model can be neglected. The empirical covariance functions derived by GOCO06s, figure 5.12b and 6.19b, shows truly a stochastic signal with no deterministic components for the spatial distances depicted in the corresponding figures. Here again, the signal variance using GOCO06s is by an order of 2 larger compared to EGM2008 and XGM2019e2159. On the other hand, the empirical covariance functions for EGM2008, figure 5.10b and 6.17b, shows relatively large difference compared to what can be seen for XGM2019e2159 and GOCO06s. Especially figure 6.17b looks to contain a deterministic signal consisting of two components with a period of approximately $1°$ and one of larger wavelength, respectively. In order to apply any correction formula for the residual geoid height a much more detailed knowledge of the deterministic signal components must first be obtained. Therefore, no correction is applied to the residual geoid height for EGM2008. This is a topic that can, and should, be investigated further in future research.
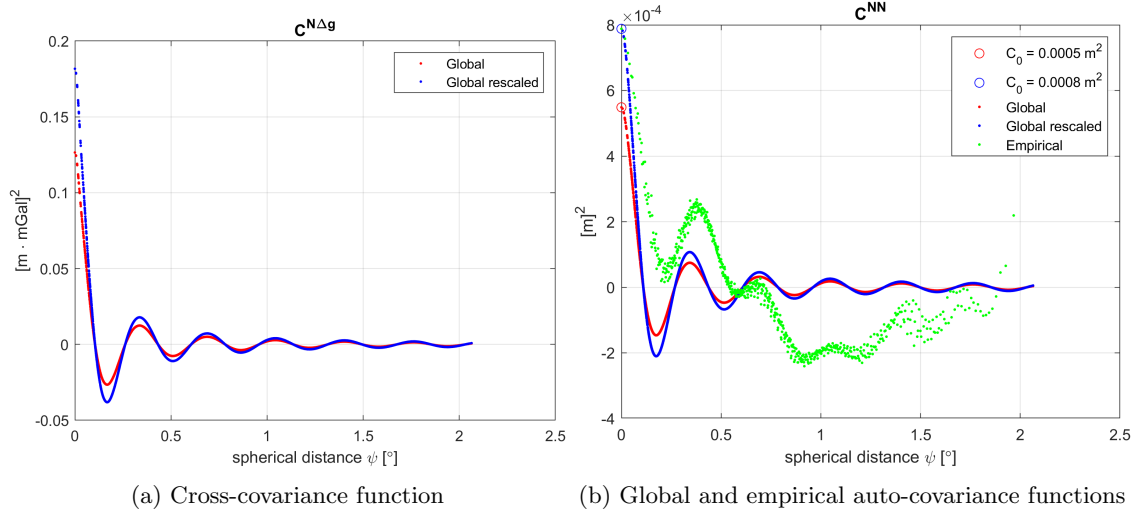

(a) Cross-covariance function
(b) Global and empirical auto-covariance functions

Figure 6.17: Figure 6.17a: Cross-covariance functions between residual geoid height and gravity anomaly $C^{\Delta N \Delta g}$. Figure 6.17b, red line: global covariance and green dots: empirical covariance functionsfor residual geoid height. EGM2008 is applied for the remove-step.

(a) Cross-covariance function

(b) Global and empirical auto-covariance functions

Figure 6.18: Figure 6.17a: Cross-covariance functions between residual geoid height and gravity anomaly $C^{\Delta N \Delta g}$. Figure 6.17b, red line: global covariance and green dots: empirical covariance functionsfor residual geoid height. XGM2019e2159 is applied for the remove-step.

(a) Cross-covariance function

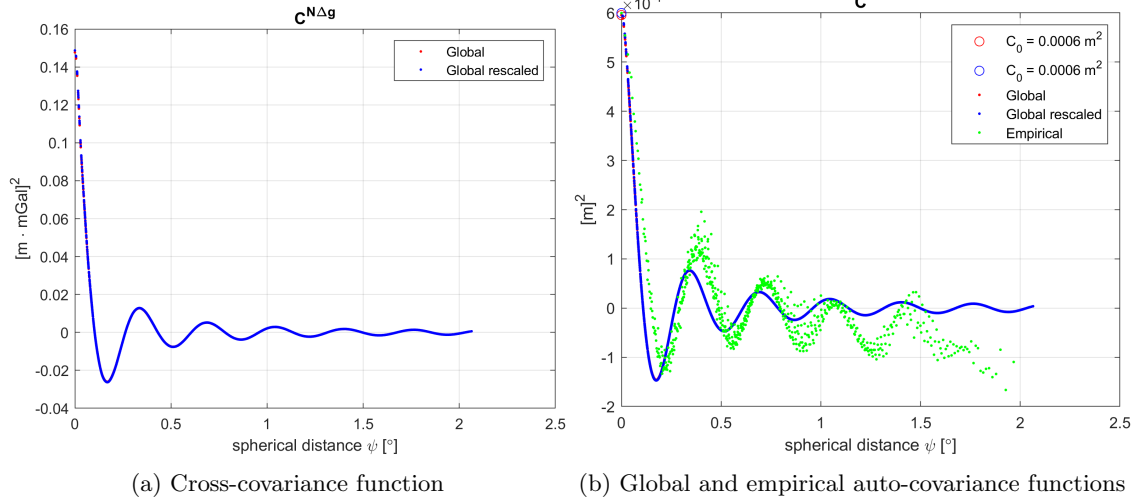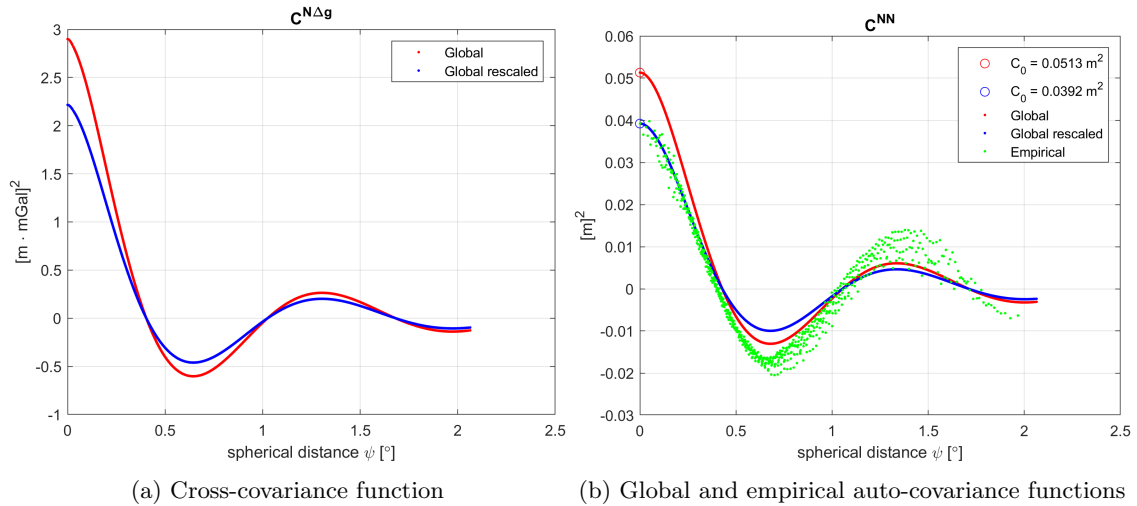(b) Global and empirical auto-covariance functions

Figure 6.19: Figure 6.17a: Cross-covariance functions between residual geoid height and gravity anomaly $C^{\Delta N \Delta g}$. Figure 6.17b, red line: global covariance and green dots: empirical covariance functionsfor residual geoid height. GOCO06s is applied for the remove-step.

In figure 6.20a, 6.20a and figure 6.20a the empirical errors are once again shown alongside with the difference between SHS derived gravity anomalies and DTU13GRA in figure 6.20b, 6.21b and 6.22b. Also when using DTU18MSS all three GGMs contribute by LSC to a reduced mean value and standard deviation. A comparison of the empirical and formal errors from LSC using DTU13MSS and DTU18MSS will be given in the following section. Table 6.3 shows descriptive statistics using for the empirical error using LSC with DTU18MSS as the MSS model. The same results as obtained in the case of DTU13MSS can again be concluded from table 6.3. GOCO06s achieves the greatest reduction of 69 % and 72 % for the mean value and standard deviation, respectively.

Table 6.3: Comparison of empirical errors resulting from LSC applied to residual geoid height signal using DTU18MSS as MSS model with residual gravity anomaly formed by the difference in gravity anomaly from SHS using the different GGMs and gravity anomalies derived from DTU13GRA. All quantities have unit mGal.

| Empirical errors | DTU18MSS | | | | $\Delta g_{shs} - \Delta g_{DTU13GRA}$ | | | |
	min	max	mean	std	min	max	mean	std
EGM2008	-7.596	7.727	0.069	2.350	-10.204	9.826	-0.106	3.629
XGM2019e2159	-9.124	8.445	-0.444	2.346	-9.930	9.145	-0.578	3.589
GOCO06s	-9.255	6.163	-0.682	2.234	-23.332	14.023	-2.233	8.186

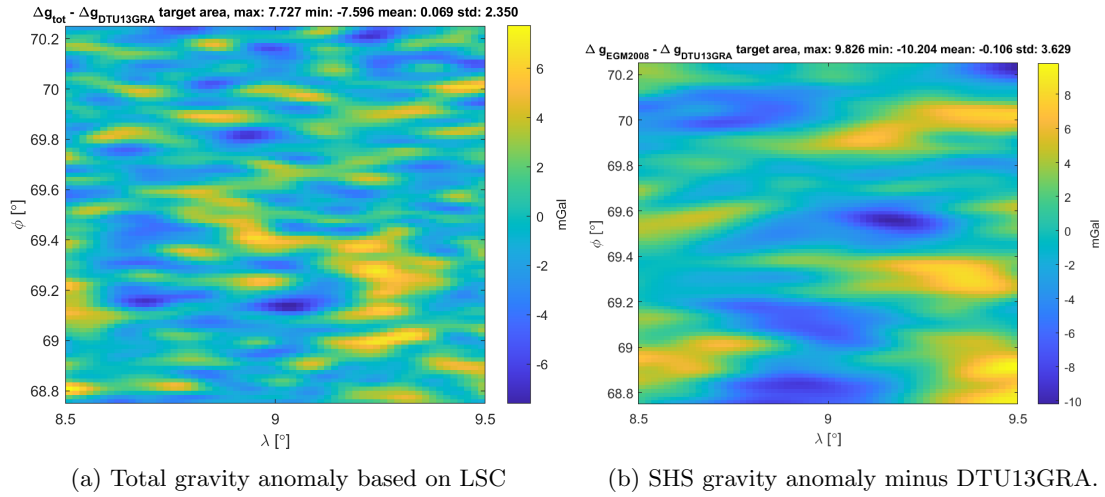(a) Total gravity anomaly based on LSC

(b) SHS gravity anomaly minus DTU13GRA.

Figure 6.20: Evaluation of the contribution by LSC of gravity anomalies from residual geoid height using EGM2008 for the remove-restore step.

(a) Total gravity anomaly based on LSC
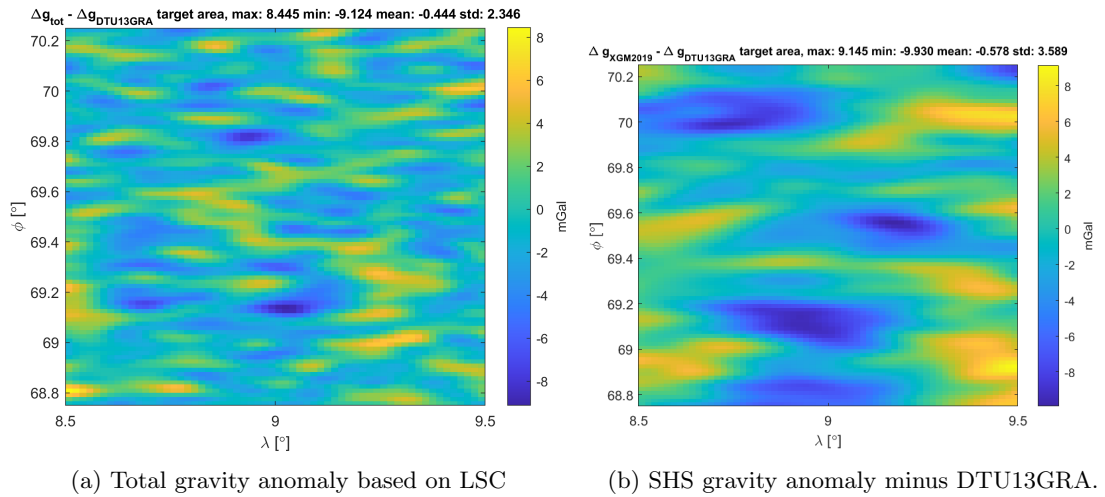
(b) SHS gravity anomaly minus DTU13GRA.

Figure 6.21: Evaluation of the contribution by LSC of gravity anomalies from residual geoid height using XGM2019e2159 for the remove-restore step.

(a) Total gravity anomaly based on LSC

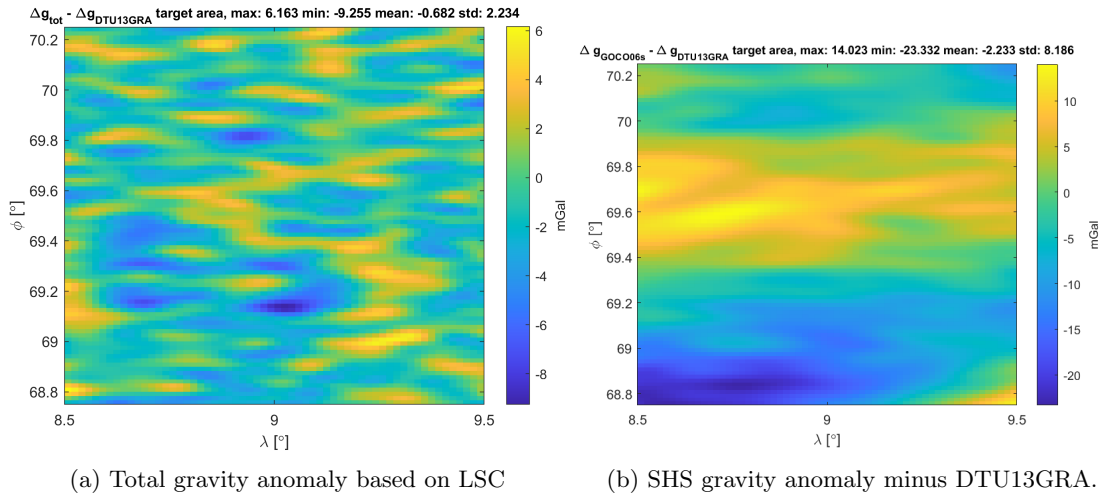(b) SHS gravity anomaly minus DTU13GRA.

Figure 6.22: Evaluation of the contribution by LSC of gravity anomalies from residual geoid height using GOCO06s for the remove-restore step.

The formal errors, calculated according to equation (5.19), are shown in figure 6.23, 6.24 and 6.25. All GGMs results in a homogeneous field, and compared to the results for DTU13MSS only minor differences can be seen.
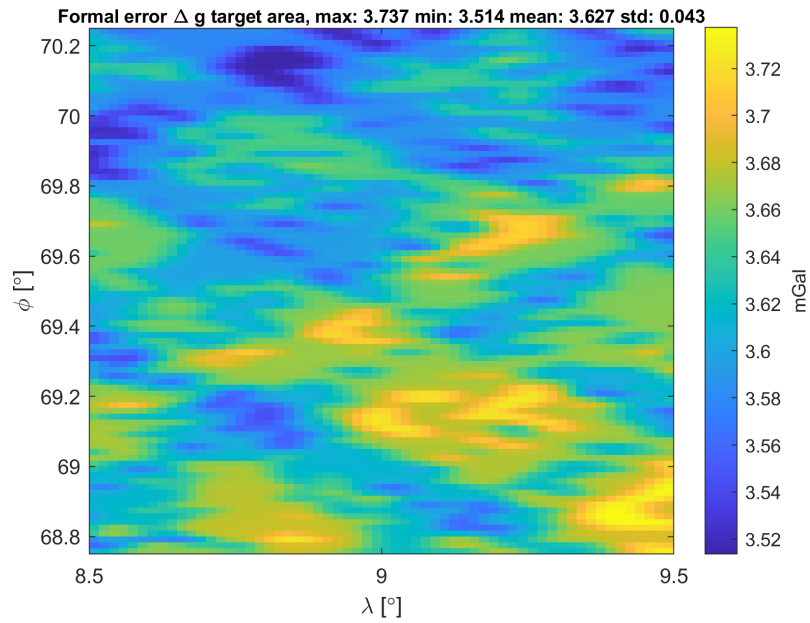
Figure 6.23: Formal errors using covariance functions with EGM2008.

Formal error △ g target area, max: 3.900 min: 3.659 mean: 3.781 std: 0.046
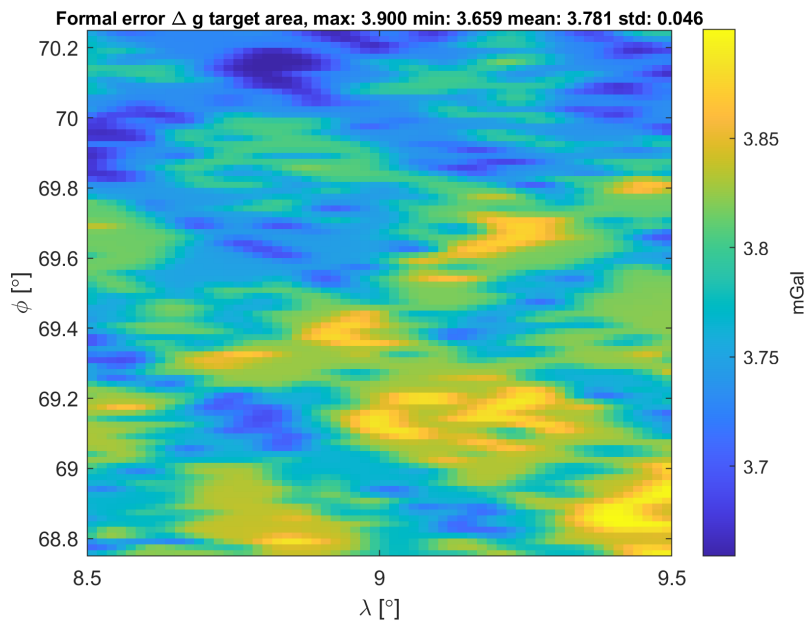
Figure 6.24: Formal errors using covariance function with XGM2019.

Formal error △ g target area, max: 3.545 min: 3.338 mean: 3.443 std: 0.039
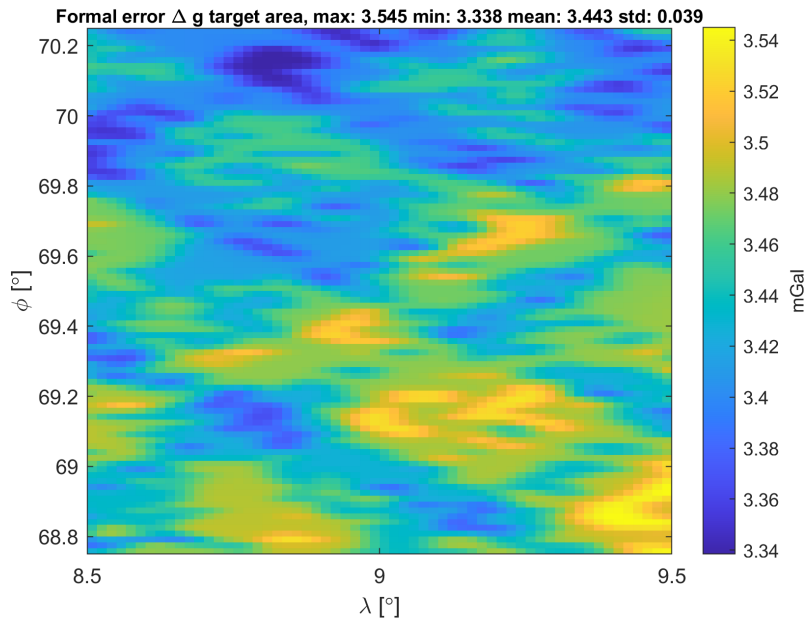
Figure 6.25: Formal errors using covariance function with GOCO06s.

6.1.3 Summary of LSC in the validation area

To summarize the prediction of gravity anomalies from residual geoid heights by LSC, table 6.4 shows the empirical and formal errors for the two different MSS models. In addition to using three different GGMs, the calculations were also carried out using two different MSS models. The comparison of global covariance functions, as was made in the previous sections, showed hardly any differences. The observations, residual geoid heights ΔN, together with the global covariance functions solely determines LSC. As no difference in the global covariance functions could be seen either using DTU13MSS or DTU18MSS as the MSS model, then the slight difference in results using LSC must be caused by the input ΔN dataset or the MSS' error field. Figure 6.26 shows the difference between DTU13MSS and DTU18MSS which reaches a maximum of -6.5 cm. With this observation alongside with similar error-fields, it is expected that LSC applied to the residual geoid height signal ΔN will result in similar empirical and formal errors using the two different MSS models. From table 6.4 a slight increase in standard deviation for the empirical error when using DTU18MSS can be seen. From the similar formal errors when using DTU13MSS and DTU18MSS, then the slight increase in empirical error must be caused by the small difference between the MSS models as shown in figure 6.26.

Table 6.4: Comparison of empirical and formal errors from LSC applied to residual geoid heights formed by using different MSS models, where left and right parts are the results using DTU13MSS and DTU18MSS as MSS models, respectively. All quantities have unit mGal.

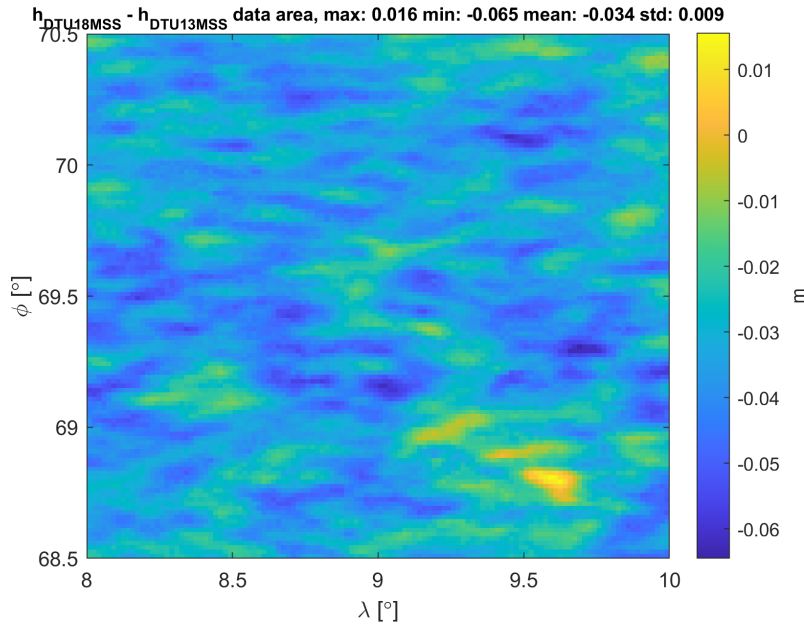|	DTU13MSS				DTU18MSS			
Empirical errors	min	max	mean	std	min	max	mean	std
EGM2008	-7.283	5.850	0.044	1.877	-7.596	7.727	0.069	2.350
XGM2019e2159	-8.360	5.811	-0.465	1.920	-9.124	8.445	-0.444	2.346
GOCO06s	-6.738	4.810	-0.688	1.680	-9.255	6.163	-0.682	2.234
Formal errors	min	max	mean	std	min	max	mean	std
EGM2008	3.517	3.738	3.642	0.037	3.514	3.737	3.627	0.043
XGM2019e2159	3.723	3.969	3.861	0.041	3.659	3.900	3.781	0.046
GOCO06s	3.285	3.476	3.391	0.032	3.338	3.545	3.443	0.039

Figure 6.26: Difference in MSS between DTU18MSS and DTU13MSS.

Evaluation of empirical errors, independent of MSS model used, shows that satellite altimetry derived gravity anomalies using the RCR-method with LSC results in empirical errors between $1.68 - 2.35$ mGal when compared to DTU13GRA. In addition, corresponding formal errors are estimated in the range between $3.39 - 3.78$ mGal. For all calculations the formal errors represent an upper-bound error estimate. Accordingly, gravity anomalies obtained by LSC can safely be included in other estimations with weights determined from their formal errors. GOCO06s is the GGM which results in the smallest empirical and formal errors, both in the case of DTU13MSS and DTU18MSS. This is probably relating to the observations used in the processing of GOCO0s which is solely collected by satellites (Kvas et al., 2021), and accordingly the GGM will not reflect on-land topographic effects observed with terrestrial techniques. The results obtained by empirical and formal errors using all GGMs are in agreement with accuracy of marine gravity field as found in literature, e.g., Andersen (2013); Nguyen et al. (2020).

6.2 Testbed of Sunnmøre

The near *closed-loop* simulation for the validation area showed that realistic estimates of satellite altimetry derived gravity anomalies can be obtained from residual geoid heights by applying LSC. The numerical investigations by LSC have been applied in open waters where the quality of global MSS and gravity field models are not degraded by coastal effects. For validation purposes DTU13GRA was considered ideal to be used as empirical validation for the near *closed-loop* simulation. In coastal areas, the quality of DTU13MSS degrades due to sparse sampling and extrapolation effects. The accuracy of DTU13GRA also degrades as DTU13MSS is used in its estimation.

The Norwegian Mapping Authority (NMA) has initiated a research project to study the possibility of creating a common physical vertical datum on land and at sea. To serve this project, a testbed, located at $\phi = [61.9°, 62.5°]$ and $\lambda = [4.5°, 6.5°]$, covering approximately $250\,\text{km} \times 250\,\text{km}$ has been established. Within this testbed, gravity observations with a density of $\sim 2\,\text{km}$ have been collected in the recent years (Kartverket, 2020).

The numerical investigations in section 6.1 showed that only GOCO06s, when the covariance function was modelled as outlined in section 6.1, resulted in analytical covariance function with similar shape as commonly reported in literature, .e.g., Knudsen (1987); Nguyen et al. (2020); Heydarizadeh Shali et al. (2020). GOCO06s was also the GGM that resulted in smallest empirical and formal errors using both MSS models in the validation area. Based on these findings and time limitations, only GOCO06s is used for LSC predictions at the Sunnmøre testbed.

For the Sunnmøre testbed, LSC of gravity anomalies is carried out based on residual geoid heights calculated from a dataset of SSH measurements gathered with Saral/ALTIKA, Saral/ALTIKA-GM, Sentinel-3A and Cryosat-2 (Ophaug et al., 2019). In contrast to the validation area, where data originated from models provided homogeneously on a grid, the SSH measurements forms a heterogeneous dataset. The SSH measurements, collected over a time period between 2013 and 2017, have undergone a preprocessing to ensure high quality of the dataset. This preprocessing involves calculating offsets between the satellite missions from crossover analysis, and reducing the ocean tide (OT) contribution on the measurement by applying a local OT model from the NMA. In addition, seasonal effects are eliminated by subtracting a linear model including annual and semi-annual harmonics. For further details about processing and estimations of the SSH observations I refer to Ophaug et al. (2019) where a detailed description can be found. The SSH measurements use WGS84 as their reference ellipsoid, and following no inconsistency exists in reference ellipsoid between the SSH measurements, GGM and MDT. The residual geoid height ΔN calculated at the heterogeneous observation points is shown in figure 6.27. To obtain MDT values at the observation points, in order to apply equation (5.17), a 2D cubic interpolation method has been applied. This interpolation technique is also applied to DTU13GRA in order to obtain independent gravity anomalies used for validation.

Figure 6.28b shows the empirical and analytical covariance function calculated by the same approach as in section 6.1. The empirical and analytical covariance function for the Sunnmøre testbed shows to a large extent the same behaviour as for the validation area, see figure 6.19b or 5.12b. The validation area was selected far from the Norwegian coast to avoid coastal effects, and from this reasoning it was expected to see a different behaviour of the empirical covariance function in the Sunnmøre testbed. As the estimation of sea state biases and dynamical effects are reported to be more complex in coastal areas, then the empirical covariance function would be expected to contain more deterministic signals due to the uncertainty and incompleteness of the MDT modelling and from a larger noise on the observations itself. By comparison of 6.28b with 6.19b or 5.12b it can be seen that the Sunnmøre testbed consist of a signal with a period of around 1° while in the validation area the signal has a considerable longer wavelength characteristic and a period of approximately 2°. Coastal effects were expected to show up as short wavelength components in the empirical covariance function, but no such effect can be seen in figure 6.28b. The empirical covariance function has the same shape as the empirical covariance function found in other literature. The only difference, except from the periodicity of the signal, between the two cases is the signal amplitude described by the two functions variance, i.e., $C(\psi) = C_0$. The residual geoid signal ΔN at Sunnmøre has a larger amplitude compared to the validation area of a factor 1.25,
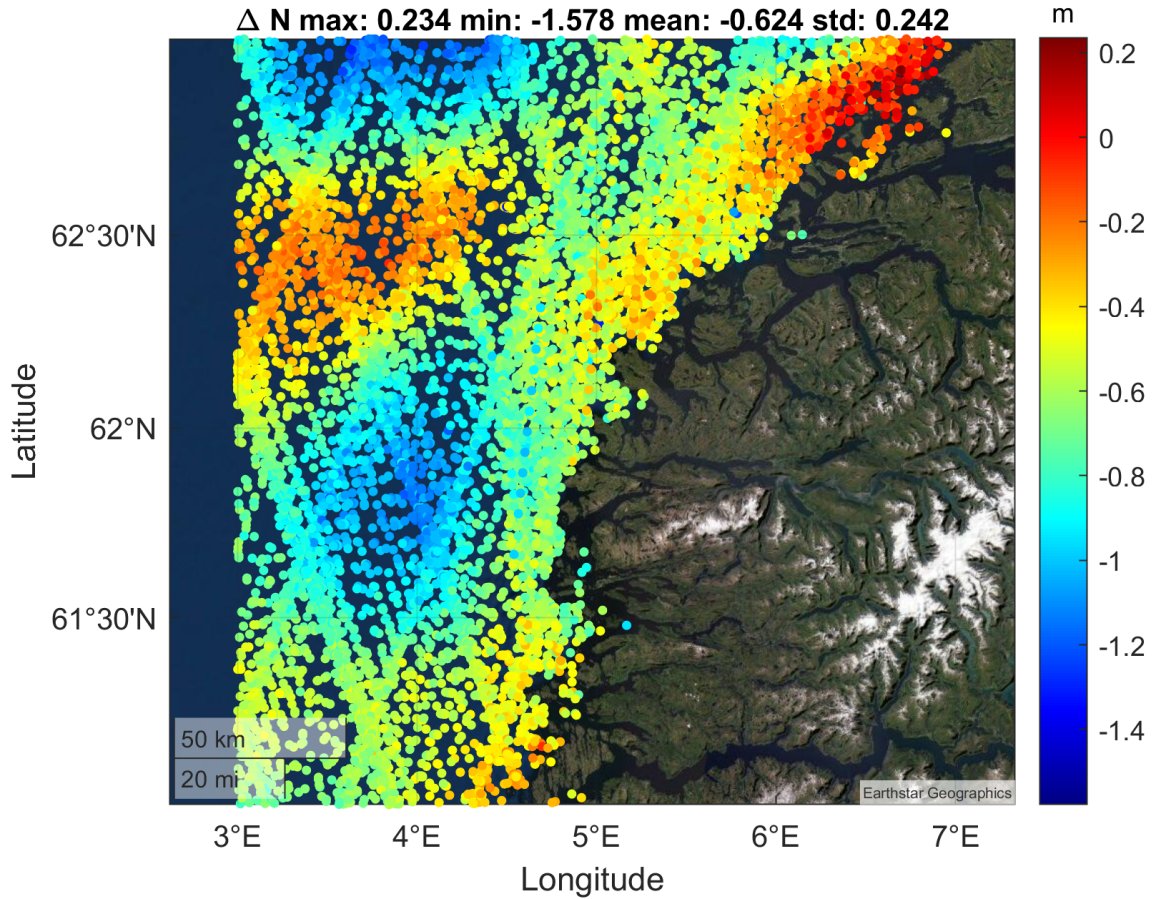
Figure 6.27: The Sunnmøre testbed covers a region of $\phi = [61.9°, 62.5°]$ and $\lambda = [4.5°, 6.5°]$. Here the residual geoid height ΔN is calculated according to equation (5.17) with SSH dataset, GOCO006s and DTU13MDT.

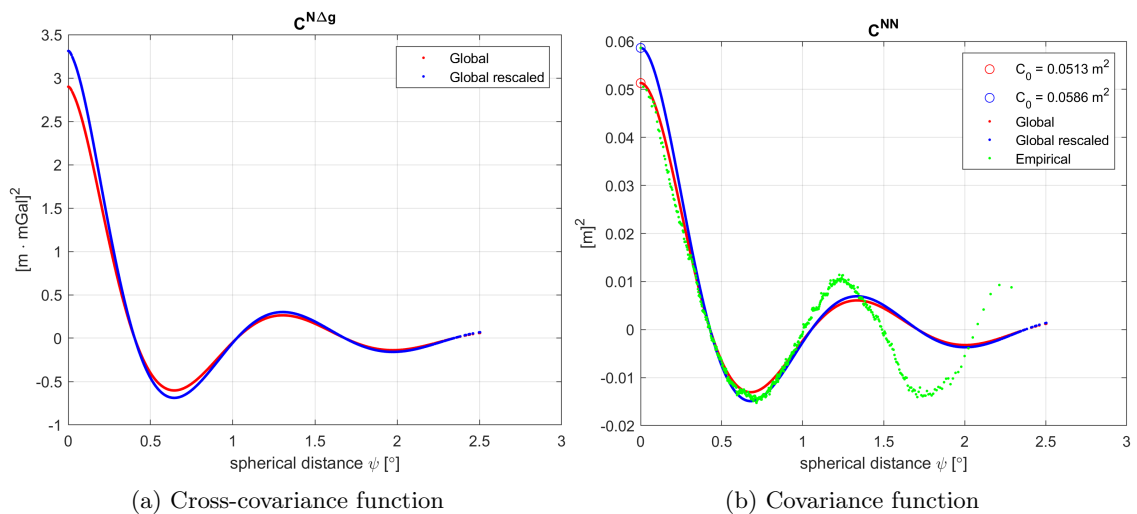(a) Cross-covariance function

(b) Covariance function

Figure 6.28: Figure 6.28a: Cross-covariance. Figure 6.28b: auto-covariance function for the Sunnmøre testbed. Residual geoid height is generated according to equation (5.17).

Table 6.5: Empirical errors formed as differences between the total gravity signal based on LSC and gravity anomalies from DTU13GRA. The formal errors are calculated according to equation (5.19). All quantities have unit mGal.

| | $\Delta g_{tot} - \Delta g_{DTU13GRA}$ | | | | Formal errors | | | |
	min	max	mean	std	min	max	mean	std
GOCO06s	-15.205	19.020	-1.787	4.084	4.704	7.811	5.551	0.387

which is not by any means a great increase. These first investigations at the Sunnmøre testbed shows a good consistency between the different datasets, and no clear deterministic signal component can be observed from the residual geoid height and its empirical covariance function. The large maximum negative value for the residual geoid height in the Sunnmøre testbed, shown in figure 6.27, is probably caused by an gross error, especially since the maximum positive value only differ from the mean value with $0.858\,\text{m}$ compared to $1.540\,\text{m}$ for the negative value. As a rule of thumb, a gross error is recognized if it deviates from the mean value with more than 3 times the standard deviation. Accordingly the maximum positive value can also be a gross error, but a closer inspection of the residual geoid height shows no clear jump in value for the 10 or 20 maximum values. For the negative case things are quite different, where the two most negative values differ from the rest by $0.5\,\text{m}$. This is more than the variation of the following 300 SSH observations. The two gross errors found using this simple method are located at the border of the dataset with a position of $\phi = [62.4214°, 62.4628°]$ and $\lambda = [3.0157°, 3.0071°]$. These two observations are removed from the dataset before the calculations of empirical covariance functions and LSC predictions are performed, but no updated plot of residual geoid height will be given here.

Figure 6.28b shows both the original global covariance function derived from potential coefficients of the GGM and the scaled global covariance function with its scaling coefficient derived from variance comparison using equation (4.10). Earlier it has been stated that the scaled covariance function will be used in order to adapt the global covariance function to local effects. From figure 6.28b it is seen that the global covariance function's fit with the empirical covariance function degrades for the scaled version, so a visual inspection of the original and scaled global covariance function should always be done. From this observation the LSC in the Sunnmøre testbed will use the unscaled global covariance function. The primarily purpose for using LSC on a residual signal is to perform a detailed analysis of the signal's short wavelength components. Figure 6.29 shows a comparison of the difference in empirical errors between gravity anomalies derived by SHS using GOCO06s and LSC predictions applying the RCR method. The gravity anomalies obtained by LSC predictions reduces the empirical errors standard deviation by a factor of 4, and hence shows that LSC and the RCR method can offer large benefits compared to only applying a standalone comparison with a global model. Large empirical errors for the standalone comparison using GOCO06s is expected as it is a *satellite-only* model expanded up to a spherical harmonic degree of 300. The empirical error increases closer to the coast where islands and fjords creates a very complex environment for the satellite altimetry and its quality is expected to degrade (Abdalla et al., 2021). Ophaug et al. (2019) with their model DTU18MSS, using the same dataset, reports an empirical error of $\approx 8\,\text{cm}$ by comparison with tide gauges. Accordingly, measurement noise of $D_\Delta = 0.08\,\text{m}^2$ is added to the auto-covariance matrix creating a stable system without producing any clear signs of large smoothing effects. SSH measurements fulfilling the conditions $\phi \in [3°, 7°]$ and $\lambda \in [61°, 63°]$ were selected as observations for the LSC. This resulted in a total number of 12586 data points. At the Sunnmøre testbed no clear boundary effects for the LSC predicted gravity anomalies is visible, meaning that no creation of a 'target area' used for comparison is necessary. As DTU13MDT and DTU13GRA are interpolated onto the SSH observation points, then no further modification of the implementation in MATLAB is required. The empirical errors, see figure 6.29b, obtained in this thesis, where computations are performed along the challenging Norwegian coast, achieves similar results as found in Nguyen et al. (2020). The empirical errors obtained by (Nguyen et al., 2020) are calculated from LSC predictions using an extended collocation formulation allowing for the combination of both observations from satellite altimetry derived gravity anomalies and ship-measured gravity anomalies. A summary of the comparison between satellite altimetry derived gravity anomalies and DTU13GRA together with its formal errors can be found in table 6.5.
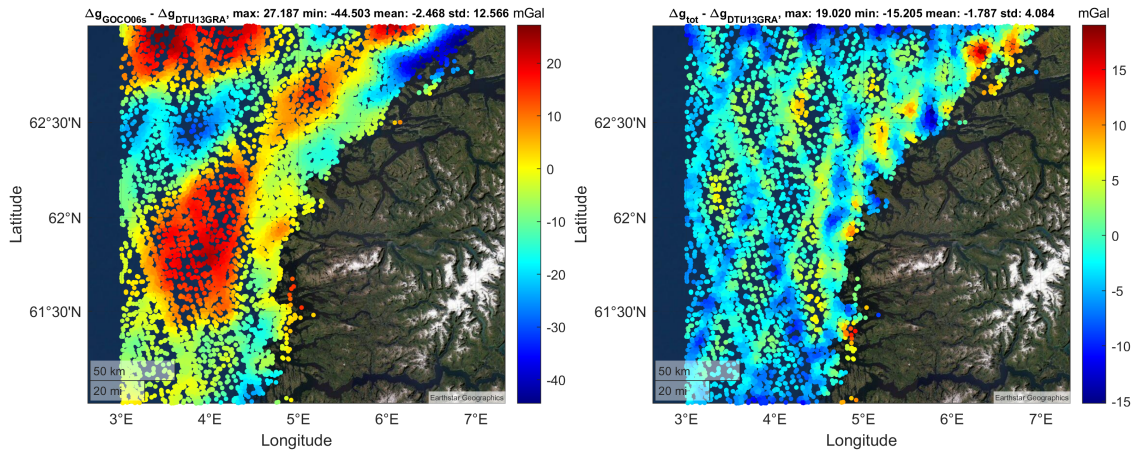
(a) Empirical error of gravity anomalies derived by SHS using GOCO06s and DTU13GRA.

(b) Empirical errors of LSC predicted gravity anomalies and DTU13GRA.

Figure 6.29: Comparison of empirical errors. Figure 6.29a: Difference in gravity anomalies derived by SHS from GOCO06s and DTU13GRA. Figure 6.29b: Difference between the total gravity anomaly signal constructed by LSC predictions and applying GOCO06s for the *remove-restore* step and DTU13GRA.

The formal errors, shown in figure 6.30 computed using equation (5.19), still serves as an upper-error estimate for the empirical error's standard deviation as shown in figure 6.29b. In the same way as for the validation area, a too conservative error estimates by the formal errors is preferable, than vice versa. If the resulting gravity anomalies are used in further computations, then a potential weighting of the observations based on their corresponding formal errors will assign a lower weight to the satellite altimetry derived gravity anomalies, instead of a high weight if the formal errors would have been to optimistic. Figure 6.28b reveals that larger frequency oscillation for point-pairs separated by a spherical distance of larger than $\psi \sim 1.5°$ cannot be approximated by the global covariance function. From the comparison of signal amplitude between the two areas, only an increase of a factor 1.25 in variance could be observed for the Sunnmøre testbed, and accordingly a small increase in formal error would be expected. A formal error of 5.723 mGal can be explained by the small increase in signal variance and taking into consideration the increased measurement noise of 8 cm compared to less than 2 cm in the validation for DTU13MSS and DTU18MSS. Compared with the empirical and analytical covariance functions found in Nguyen et al. (2020), the corresponding functions for the Sunnmøre testbed closely resembles this shape. The formal errors are predicted entirely on the observations mathematical relationship described through its auto-covariance and cross-covariance functions. Again I would like to emphasize that the formal errors are independent of the observations, except for the assumed measurement noise forming the measurement noise matrix D_Δ. Any unmodelled signal components should result in poor prediction results and thereby large empirical errors. From figure 6.30 it can also be seen that the formal errors increases in-between the satellite tracks. A more sparse sampling is existing in these regions compared to along the satellite tracks, and the LSC of gravity anomaly will then rely more on observations further away compared to points along the satellite track. The analytical and empirical covariance function starts deviating for point-pairs separated by more than 1.25°, even here the differences are considered to be small, which also is supported by the small variations in formal error. Still, the geometry of the observations is reflected in the formal errors. For now the formal errors are considered to represent an upper-bound error field, which can safely be used for weight assignment in the computations where the satellite derived gravity anomalies are taken as input.
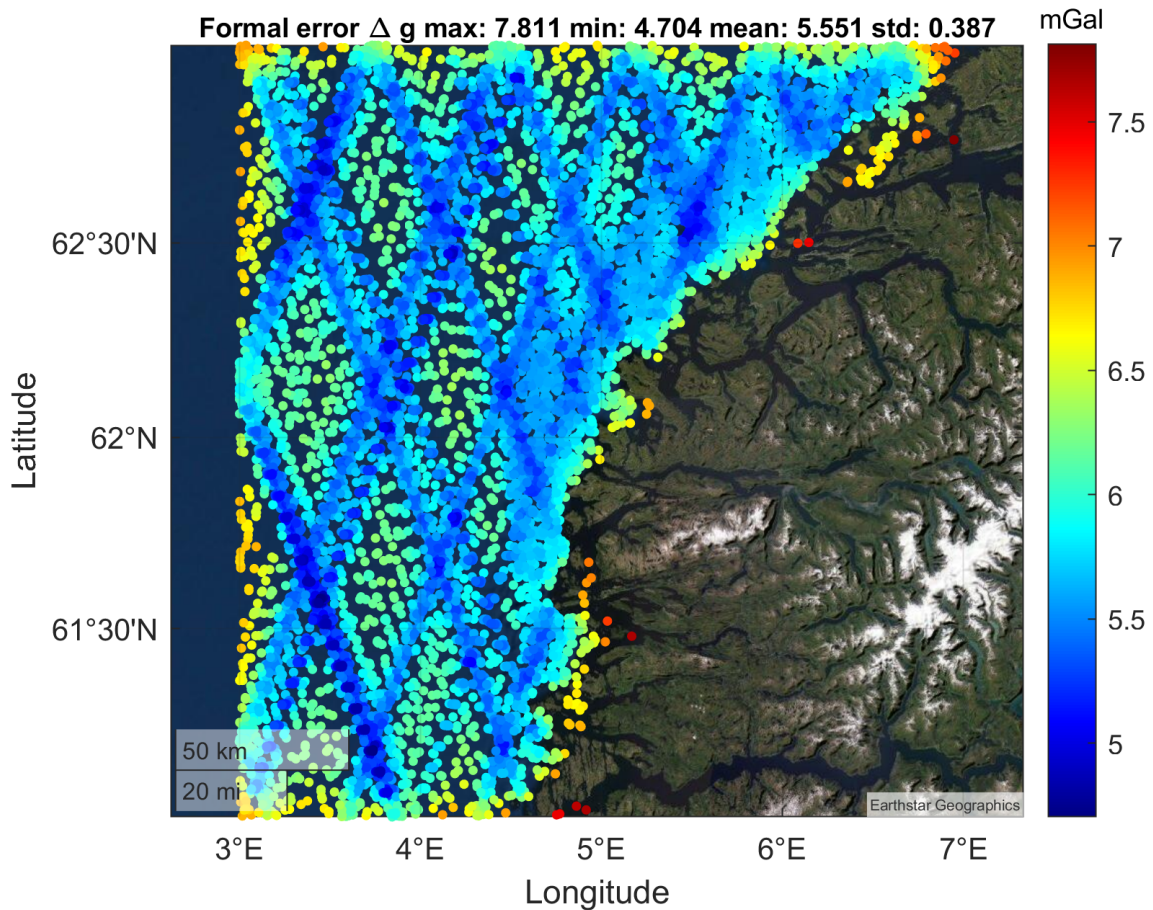
Figure 6.30: Figure showing the formal errors of the LSC predicted gravity anomalies using equation (5.19).

The empirical validation with DTU13GRA is more questionable for the Sunnmøre testbed as its accuracy degrades in coastal areas. An independent set of gravity measurement collected by the NMA should have been used as an external validation of the gravity anomalies derived from residual geoid height by LSC. For comparison with the NMA gravity measurements a new computation procedure was set up in MATLAB. This procedure involved to predict gravity anomalies at an evenly spaced grid with the same resolution as DTU13GRA, and then the LSC predicted gravity anomalies were interpolated to the observation points of the NMA. The NMA gravity observations would have been an independent validation of the LSC, and in contrast to DTU13GRA which is a global model of gravity anomalies, the NMA dataset consist of single point observations that have not undergone any common estimation procedure resulting in a gravity anomaly surface or anything like that. Due to time limitations the final implementation was not achieved. A future validation with the NMA will be of great importance as it provides a solid measure on the possibility, and application, of satellite altimetry derived gravity anomalies in addition to gravity anomalies obtained by dedicated satellite gravity missions and national measurement campaigns. Another important aspect is that it will give a more reliable measure of the error estimates.

Chapter 7

Conclusion and outlook

Within this thesis, satellite altimetry derived gravity anomalies were predicted from residual geoid heights using LSC. First a theoretical study of GGMs, LSC and covariance functions was carried out. Based on these findings, implementation of LSC and numerical investigations were performed using MATLAB. The numerical investigations took place at two different study areas. One area was selected in open-water, not influenced by coastal effects, to be used for validation purposes, while the other area was selected at a gravimetric testbed in coastal areas outside of Sunnmøre created by the NMA. For the validation area, DTU13GRA was used to derive empirical errors in a near *closed-loop* simulation. The residual geoid heights were formed by using two different MSS models, DTU13MSS and DTU18MSS. In addition, separate computations were performed using different GGMs for the RCR-method, namely EGM2008, XGM2019e2159 and GOCO06s. The comparison of empirical and formal errors using the different GGMs showed similar results, where GOCO06s obtained the smallest empirical and formal errors for both DTU13MSS and DTU18MSS. For the Sunnmøre testbed only GOCO06s was used as GGM, and here the total gravity signal based on LSC was compared with DTU13GRA. The quality of DTU13GRA is known to degrade in coastal areas, so the empirical errors for the Sunnmøre testbed must be used with caution. Due to time limitations, an external validation with shipborne gravimetric observations provided by the NMA was not possible.

From the results documented in section 6, some conclusion and areas for further research can be drawn. Even though considerable work has been paid to the field of covariance modelling, there is still room for optimisation and theoretically studies to ensure a proper handling of covariance modelling in accordance to methods found in literature (Knudsen, 1987; Nguyen et al., 2020; Heydarizadeh Shali et al., 2020). A detailed understanding to the topic of covariance modelling and LSC can be achieved by the research of Zingerle et al. (2020); Willberg et al. (2020), where the latter is part of the International Association of Geodesy (IAG) joint working group (JWG) 2.2.2, called the '1 cm geoid experiment'. A topic that has been neglected in this thesis, is the truncation method for calculating height anomalies ΔN and gravity anomalies Δg from the truncated GGM. The simple 'rigorous' cutting of the GGM's potential coefficients at a spherical harmonic degree N_{cut}, which is the method used in this thesis, creates well-known side lobes in the spatial structures of the truncated field (Barthelmes, 2008). A natural starting point for future work would be an investigation of the difference between using a rigorous or gentle truncation of the GGM's spherical harmonic coefficients. The computation service provided by ICGEM already offers the possibility to select preferred truncation method. Pail et al. (2017); Zingerle et al. (2020), in their computation of XGM2016 and XGM2019e, treats topics of data combination and model truncation. They are using a tapering function to assign relative weights of the observations in land-ocean transition areas, and also weights for the potential coefficients in order to compare GGMs with different spherical harmonic degrees. Those articles can form the foundation and guidelines for looking into the topic of truncation methods and tapering functions.

The simplified covariance modelling used in this thesis showed that computation of one common degree variance vector, and then estimate one common scaling coefficient, will result in odd-shaped covariance functions if there exists jumps in the degree variance vector. The implementation of a

least-squares adjustment method for estimating the model parameters α, R_b and A proved itself to be a difficult task, and at last the proposal of a slightly modified way of covariance modelling forced its way. Here a new problem relating to the calculation of one common degree variance vector, given by equation (5.24), emerged. The idea, which was finally validated with the use of GOCO06s, was to account for both commission and omission error of the GGM used in the *remove-restore* step, but also include higher degree effects by a Tscherning-Rapp covariance model. Optimization in covariance modelling by least-squares determination of the model parameters will further reduce the formal errors, as they are more sensible to changes in the covariance modelling than the estimate of gravity anomalies from LSC itself. In comparison with residual gravity anomalies Δg_{res}, formed by the difference between SHS-derived gravity anomalies and DTU13GRA, all GGMs used within this thesis resulted in significantly reduced empirical errors by prediction of gravity anomalies using LSC. When it comes to the selection of GGM one can even argue that using a satellite-only GGM, here represented by GOCO06s, suffice for the remove-restore method. The calculations with different MSS models showed similar results, where the slight variations are assigned to the difference between DTU13MSS and DTU18MSS for the validation area. GOCO06s results in the smallest empirical and formal errors both for DTU13MSS and DTU18MSS. The RCR-method should in principle be model independent *if* the GGM is of high quality and fits well with the local effects, and similar empirical and formal errors obtained using different GGMs confirms this assumption about model independency.

Initial investigations, not shown within this thesis, of forming residual geoid height ΔN by using the high-resolution GGMs EGM2008 and XGM2019e2159 up to its maximum spherical harmonic degree 2190 resulted in empirical covariance functions with clear signs of trend and deterministic signal. Accordingly, the continuing calculations were performed with the high-resolution GGMs maximum spherical harmonic degrees truncated to 1000. The empirical covariance function is generated by a set of local observations representing the signal's spatial variations. Strictly speaking it is no necessity for the empirical covariance functions to follow a smooth shape as is resulting from the use of GOCO06s and XGM2019e2159, but those functions are known to fulfill the stochastic requirements in order to apply LSC. Even though the global covariance functions are derived from the potential coefficients of a GGM, and hence reflects the signal characteristics on a global scale, the empirical covariance functions should not contain any clear signs of trends or accelerations. Plots of residual geoid heights, as shown within this thesis, can only provide information about any clear deterministic signal components with respect to the dataset's geometry or any inconsistency in definitions and reference systems between the MSS, MDT and GGM. The empirical covariance function is a great tool for detecting deterministic components of the residual geoid height signal. EGM2008 is the only GGM resulting in empirical covariance functions for DTU13MSS and DTU18MSS with a different shape, see figure 5.10b and 6.17b, than commonly reported in literature. This is a result that should be investigated further. A final evaluation of the different GGM's accuracy in the Norwegian coastal zone would be an interesting study, even though I strongly argue that the best-guidelines should be to use the best possible GGM in the *remove-restore* step.

Nguyen et al. (2020) in their study uses EIGEN-6C4 up to its maximum spherical harmonic degree 2190 and obtains empirical covariance functions of similar shapes as the global covariance functions. In this thesis, using the same approach resulted in empirical covariance functions of different shapes than commonly reported in literature, and accordingly the maximum spherical harmonic degree of the GGMs were truncated. This result is in contrast to what is obtained by Nguyen et al. (2020). Further research should be paid to this issue. Especially, investigations of the impact from different signal-to-noise ratios by evaluation of empirical and formal errors resulting from the RCR-method using the same GGM with different truncation degree N_{cut}. After spending some time with covariance modelling, I am convinced that an empirical covariance function should not contain any clear trends or deterministic components and closely resemble the same shape of the global covariance function. The empirical covariance function is by these means a good measure of the completness in modelling the different terms of equation (5.17) for residual geoid height.

Computations following the RCR-method works on a residual signal, and its long wavelength components are removed and restored in beforehand and afterwards. Other research and evaluation of EGM2008, e.g., Gruber and Willberg (2019), indicates that increase in observations and developments of modelling and processing strategies have increased the quality of GGMs. For both DTU13MSS and DTU18MSS, EGM2008 actually obtains the smallest mean value for the empiri-

cal error. This result is assumed to be caused by a better consistency between DTU13MDT and EGM2008, but again here is a possibility for more research.

With lack of experience relating to covariance modelling, and neither a very precise knowledge of the expected accuracy in the prediction of gravity anomalies by the RCR-method, then no focus were drawn in direction of the degree variance vector. At all stages with identical implementation scheme for all GGMs, GOCO06s has resulted in promising results. Thereby, no obvious reason existed for being sceptical towards the computation of degree variances. In hindsight, a simple plotting routine during the computation of degree variances would have revealed this effect at an early stage. With knowledge from the computation approach used in XGM2019e2159, then these problems relating to the combination of degree variances could, and maybe also should, have been recognised and dealt with at an earlier stage. Using a simplified approach for EGM2008 and XGM2019e2159, where only the omission error represented by degree varinces from the GGM's potential coefficients for $N \in [N_{cut}, 2140, 2159]$ and high degree terms using a Tscherning-Rapp model, gave satisfying results. All three GGMs resulted for the validation in empirical errors even better than what was reported by Nguyen et al. (2020) for the Gulf of Tonkin.

Another encouraging result is that hardly any difference between the empirical covariance function for the two different study areas can be observed. This finding is of great importance as the requirement for applying least-squares collocation is that the residual signal can be treated as stochastic. These results shows that all components in equation (5.17) are modelled consistently, even in the coastal region where coastal effects takes a more high frequency components and impose a higher complexity of the signal. In both areas and for all the GGMs, the formal errors represents an upper-bound error estimate, which means that inclusion of altimetry derived gravity anomaly can safely be included in other calculations with weights assigned according to its formal errors.

The comparison with DTU13GRA for the two study areas validate the implementation and processing strategy of LSC as outlined in this thesis. Empirical errors derived by comparison with DTU13GRA shows that LSC prediction of gravity anomalies from sea surface height measurement observed by satellite altimetry is a method with great potential. Even in the challenging environment along the Norwegian coastline the predictions show small deviations compared to the global model DTU13GRA. The accuracy of DTU13GRA is known to degrade in coastal areas, so evaluation with independent gravity observations collected by the NMA will provide an external validation. For this future research, the implementation and processing strategies as proposed within this thesis can be used as guidelines. With an even better covariance modelling the empirical and formal errors are expected to be further reduced. Continuously improvements in altimetry observation technique, signal processing and orbit determination indicates a bright future for gravity anomalies derived from satellite altimetry. The first investigation of Sentinel-6, with its improved POD results by combination of GPS and Galileo, will provide very interesting data and especially its improvement in the coastal zone. The same conclusions as is drawn by (Nguyen et al., 2020) can also be said about the validation area and Sunnmøre testbed.

Bibliography

Abdalla, S., Abdolnabi, A., Adusumilli, S., Aich Bhowmick, S., Alou-Font, E., and Amarouche, Laiba, ... Zlotnicki, V. (2021). Altimetry for the future: Building on 25 years of progress. *Advances in Space Research.*

Andersen, O. (2013). *Marine Gravity and Geoid from Satellite Altimetry*, pages 401–451. Lecture Notes in Earth Sciences. Springer.

Andersen, O., Knudsen, P., Kenyon, S., and Holmes, S. (2014). Global and Arctic Marine Gravity Field From Recent satellite altimetry (DTU13).

Andersen, O., Knudsen, P., and Stenseng, L. (2015). *The DTU13 MSS (Mean Sea Surface) and MDT (Mean Dynamic Topography) from 20 Years of Satellite Altimetry.*

Andersen, O., Knudsen, P., and Stenseng, L. (2016). The DTU13 MSS (Mean Sea Surface) and MDT (Mean Dynamic Topography) from 20 Years of Satellite Altimetry. In Jin, S. and Barzaghi, R., editors, *IGFS 2014*, pages 111–121, Cham. Springer International Publishing.

Andersen, O., Knudsen, P., and Stenseng, L. (2018). A New DTU18 MSS Mean Sea Surface – Improvement from SAR Altimetry. page 172. 25 years of progress in radar altimetry symposium ; Conference date: 24-09-2018 Through 29-09-2018.

Barthelmes, F. (2008). Low Pass Filtering of Gravity Field Models by Gently Cutting the Spherical Harmonic Coefficients of Higher Degrees. *http://icgem.gfz-potsdam.de/gentlecut_engl.pdf last access: 29 May 2021.*

Barthelmes, F. (2009). Definition of functionals of the geopotential and their calculation from spherical harmonic models: theory and formulas used by the calculation service of the International Centre for Global Earth Models (ICGEM), http://icgem. gfz-potsdam. de.

Benveniste, J., Birol, F., Calafat, F., Cazenave, A., Dieng, H., Gouzenes, Y., Legeais, J., Leger, F., Niño, F., Passaro, M., Schwatke, C., and Shaw, A. (2020). Coastal sea level anomalies and associated trends from Jason satellite altimetry over 2002–2018. *Scientific Data*, 7.

Breili, K. (2018). GMLM211 marin geodesi - Satellittaltimetri. Lecture notes in GMLM211 at NMBU.

Dale, B. (2021). Special topic in least squares collocation. Unpublished report, individual course work.

ESA (2020a). Coastal observations boosted by new reference satellite.

ESA (2020b). Copernicus Sentinel-1 maps Norway in motion.

ESA (2020c). Europe's Copernicus programme.

ESA (2020d). Galileo enhancing Sentinel-6's sea level monitoring mission.

ESA (2020e). Sea-level monitoring satellite first results surpass expectations.

ESA (2021). Sentinel-6 passes in-orbit test with flying colours.

Fecher, T., Pail, R., and Gruber, T. (2015). Global gravity field modeling based on GOCE and complementary gravity data. *International Journal of Applied Earth Observation and Geoinformation*, 35:120–127.

Fecher, T., Pail, R., and Gruber, T. (2017). GOCO05c: A New Combined Gravity Field Model Based on Full Normal Equations and Regionally Varying Weighting. *Surveys in Geophysics*, 38.

Foerste, C., Shako, R., Flechtner, F., Dahle, C., Abrikosov, O., Neumayer, H., Barthelmes, F., Bruinsma, S., Marty, J., Balmino, G., and Biancale, R. (2011). EIGEN-6 - A new combined global gravity field model including GOCE data from the collaboration of GFZ Potsdam and GRGS Toulouse. *AGU Fall Meeting Abstracts*, 1.

Gerlach, C. (2019). Satellite Gravimetry and Global Gravity Models Gravity Reductions and Anomalies - Lecture Notes and Exercises on Physical Geodesy prepared for GMGD300.

Gerlach, C. and Ophaug, V. (2021). Lecture notes: Spesialpensum - Fysisk Geodesi, januarblokk 2021.

Gruber, T. and Willberg, M. (2019). Signal and error assessment of GOCE-based high resolution gravity field models. *Journal of Geodetic Science*, 9:71–86.

Heydarizadeh Shali, H., Ramouz, S., Safari, A., and Barzaghi, R. (2020). Assessment of Tscherning-Rapp covariance in Earth gravity modeling using gravity gradient and GPS/leveling observations. In *EGU General Assembly Conference Abstracts*, page 1059.

Hofmann-Wellenhof, B. and Moritz, H. (2006). *Physical geodesy*. Springer Science & Business Media.

ICGEM (2019). ICGEM Service Frequently Asked Questions (FAQs).

Ince, E. S., Barthelmes, F., Reißland, S., Elger, K., Foerste, C., Flechtner, F., and Schuh, H. (2019). ICGEM -15 years of successful collection and distribution of global gravitational models, associated services, and future plans. *Earth System Science Data*, 11:647–674.

Jekeli, C. (2015). *Potential Theory and the Static Gravity Field of the Earth*, pages 9–35.

Kartverket (2020). Felles referanseramme for sjø og land.

Kaula, W. (1966). *Theory of Satellite Geodesy*. Blaisdell.

Knudsen, P. (1987). Estimation and modelling of the local empirical covariance function using gravity and satellite altimeter data. *Bulletin géodésique*, 61:145–160.

Knudsen, P. (2007). Simultaneous Estimation of the Gravity Field and Sea Surface Topography From Satellite Altimeter Data By Least-Squares Collocation. *Geophysical Journal International*, 104:307 – 317.

Krarup, T. (1969). A contribution to the mathematical foundation of physical geodesy. *MeGIC*, 44.

Kvas, A., Brockmann, J., Krauss, S., Schubert, T., Gruber, T., Meyer, U., Mayer-Gürr, T., Schuh, W.-D., Jäggi, A., and Pail, R. (2021). GOCO06s - a satellite-only global gravity field model. *Earth System Science Data*, 13:99–118.

Lenovo (2020). Thinkpad e460 laptop.

Moritz, H. (1980). *Advanced Physical Geodesy*. Sammlung Wichmann : Neue Folge : Buchreihe. Wichmann.

Nguyen, V. S., Van-Tuyen, P., Nguyen, L. V., Andersen, O. B., Forsberg, R., and Bui, D. T. (2020). Marine Gravity Anomaly Mapping for the Gulf of Tonkin area (Vietnam) using Cryosat-2 and Saral/AltiKa satellite altimetry data. *Advances in Space Research*.

NOOA (2021). Altimetric Bathymetry.

Ophaug, V. (2018). Notat om permanent tidesystem. Unpublished report.

Ophaug, V., Breili, K., and Andersen, O. (2019). A coastal mean sea surface with associated errors in Norway based on new-generation altimetry. *Advances in Space Research*.

Pail, R., Fecher, T., Barnes, D., Factor, J., Holmes, S., Gruber, T., and Zingerle, P. (2017). Short note: the experimental geopotential model XGM2016. *Journal of Geodesy*, 92.

Pavlis, N., Holmes, S., Kenyon, S., and Factor, J. (2012). The Development and Evaluation of the Earth Gravitational Model 2008 (EGM2008) (vol 117, B04406, 2012). *Journal of Geophysical Research*, 118.

Stammer, D. and Cazenave, A. (2017). *Satellite Altimetry over Oceans and Land Surfaces*. CRC Press.

Tscherning, C. (1972). *An Algol-program for prediction of height anomalies, gravity anomalies and deflections of the vertical*. Geodaetisk Institut.

Tscherning, C. C. (2001). Computation of Spherical Harmonic Coefficients and Their Error Estimates Using Least-Squares Collocation. *Journal of Geodesy*, 75:12–18.

Tscherning, C. C. and Rapp, R. (1974). Closed covariance expressions for gravity anomalies, geoid undulations, and deflections of the vertical implied by anomaly degree variance models. *Scientific Interim Report Ohio State Univ., Columbus. Dept. of Geodetic Science.*, -1.

Willberg, M., Zingerle, P., and Pail, R. (2019). Residual least-squares collocation: use of covariance matrices from high-resolution global geopotential models. *Journal of Geodesy*, 93.

Willberg, M., Zingerle, P., and Pail, R. (2020). Integration of airborne gravimetry data filtering into residual least-squares collocation: example from the 1 cm geoid experiment. *Journal of Geodesy*, 94.

Wu, Y., Abulaitijiang, A., He, X., Luo, Z., Wang, H., and Zhou, B. (2020). An assessment of recently released high-degree global geopotential models based on heterogeneous geodetic and ocean data.

Zingerle, P., Pail, R., Gruber, T., and Oikonomidou, X. (2020). The combined global gravity field model XGM2019e. *Journal of Geodesy*, 94.